Design, Simulation, and Wind Tunnel Verification of a Morphing Airfoil

Eric A. Gustafson

Thesis submitted to the Faculty of the
Virginia Polytechnic Institute and State University
in partial fulfillment of the requirements for the degree of

Master of Science
in
Mechanical Engineering

Kevin B. Kochersberger, Chair
Daniel J. Inman
Robert A. Canfield

May 25, 2011
Blacksburg, Virginia

Keywords: Morphing, Macro Fiber Composite, Thin Cambered Airfoil, GenMAV

Design, Simulation, and Wind Tunnel Verification of a Morphing Airfoil

Eric A. Gustafson

ABSTRACT

The application of smart materials to control the flight dynamics of a Micro Air Vehicle (MAV) has numerous benefits over traditional servomechanisms. Under study is wing morphing achieved through the use of piezoelectric Macro Fiber Composites (MFCs). These devices exhibit low power draw but excellent bandwidth characteristics. This thesis provides a background in the 2D analytical and computer modeling tools and methods needed to design and characterize an MFC-actuated airfoil.

A composite airfoil is designed with embedded MFCs in a bimorph configuration. The deflection capabilities under actuation are predicted with the commercial finite element package NX Nastran. Placement of the piezoelectric actuator is studied for optimal effectiveness. A thermal analogy is used to represent piezoelectric strain. Lift and drag coefficients in low Reynolds number flow are explored with XFOIL. Predictions are made on static aeroelastic effects. The thin, cambered Generic Micro Aerial Vehicle (GenMAV) airfoil is fabricated with a bimorph actuator. Experimental data are taken with and without aerodynamic loading to validate the computer model. This is accomplished with in-house 2D wind tunnel testing.

To my parents David and Beverly Gustafson

Acknowledgments

I would like to acknowledge and thank the crews of old and new at the VT Unmanned Systems Lab, especially (in no order) Mike Rose, Jimmy May, Kevin Stefanik, Kenny Kroeger, Jerry Towler, Brian McCabe, and Shajan Thomas. I would be remiss to not thank Dr. Kevin Kochersberger for offering me this opportunity, and for being the reason this project was able to take foot. I'd like to extend my gratitude to Dr. Canfield for his valuable input on my thesis and research. A special thanks goes out to my parents, David and Beverly Gustafson, and my siblings, Stephen and Darla, for their support at every point of my progress.

I appreciate the efforts of AVID LLC, and especially John Ohanian, for their guidance during the project. As with all research, this work represents an extension on the academic pursuits of others, and for that I thank Dr. Onur Bilgen. Additionally, I'd like to acknowledge the VT CIMSS lab for granting me use of their wind tunnel which enabled the latter half of this research.

This work was produced in collaboration with AVID LLC as part of a Phase I and II SBIR from the US Air Force Research Laboratory (AFRL), Eglin, FL.

Contents

List of Figures

List of Tables

Chapter 1

Introduction

1.1 Background

This thesis presents a look into morphing airfoil development using a smart material technology. The term smart material is typically used to describe a subset of materials that take advantage of coupling between two forms of energy. The Macro Fiber Composite (MFC) is a recent innovation in the category of smart materials. Invented by NASA in the late 1990's [1], the uniquely efficient actuation ability of the MFC has been researched for use in structurally oriented fields including civil, mechanical, and aerospace engineering. Morphing wings have been studied with greater interest in recent times due the advent of new, small scale actuators. Such actuators are based on smart material innovations in the field of piezoelectrics, shape memory alloys (SMAs), and shape memory polymers (SMPs). In contrast with slower SMAs and weaker SMPs, piezoceramics material are better suited for fast shape control of thin wing MAVs [2], though early testing with SMAs for camber control were still explored.

MFCs are assembled from numerous layers of polyimide film (Kapton), copper, and piezoceramic fibers bonded together with epoxy. Lead-zirconate-titanate (PZT) fibers run orthogonal to interdigitated electrodes along the longitudinal axis of the actuator. Substantial electric fields up to 3 kV/mm between electrodes induce the piezoelectric effect in the fibers causing strain. The multitude of constituent materials ultimately bonded together to form the final product give rise to the "piezocomposite" descriptor. Depending on the type and structural application, MFCs may be configured for various modes of actuation. Given an

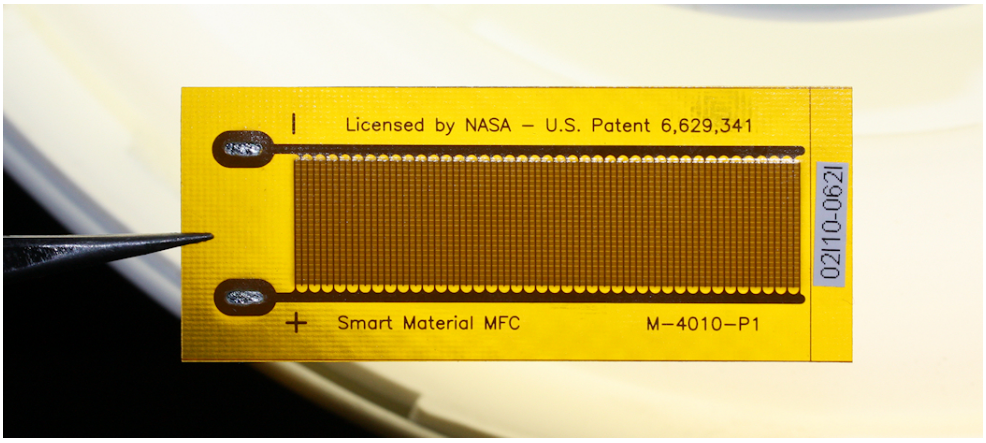

Figure 1.1: The M4010-P1 MFC actuator. The horizontal length of the active region in this photo is 40 cm.

electrical input, MFCs can provide in-plane extension and contraction, or out-of-plane bending and twisting motions. MFCs are designed to change the shape of the structure to which they are bonded after the application of an externally applied voltage. This effect is accomplished via the contraction and expansion of embedded piezoelectric fibers. The actuation scheme is able to take advantage of the efficient d_{33} mode [3]. In this mode, the induced strain is aligned perpendicular to the electrodes, also called the poling direction.

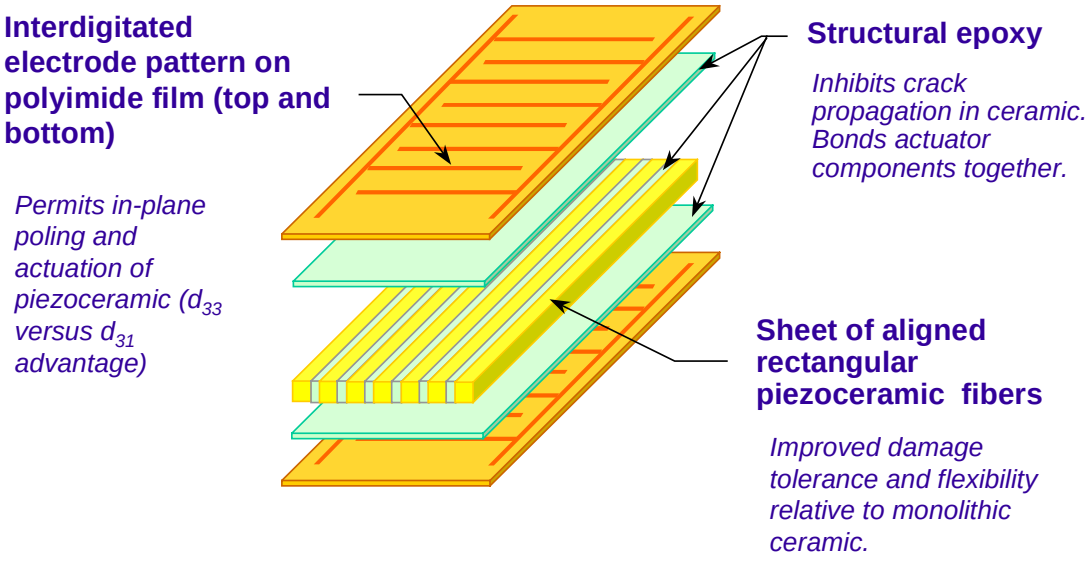

Figure 1.2: Exploded view of all layers comprising a generic MFC actuator [3].

Under the direct piezoelectric effect, piezoelectrics make an excellent case for use as energy

harvesters and sensors, since even slight deformations in the material tend to produce relatively high voltages. This level of sensitivity from physical phenomena is highly desirable for sensing applications. When utilizing the converse effect, piezoelectrics also demonstrate the ability to deform in the presence of an electric field. Under actuation, the piezoelectric effect causes a change in the geometry. Total stroke is limited since the effect is based on a small-scale crystalline deformation [2], but strains on the order of 0.1% are not unusual. Macro Fiber Composites do not escape the issues that inherently plague piezoelectrics, such as poor repeatability and strains that are difficult to control.

MFCs come from a lineage of piezocomposites that have evolved over time to allow for favorable operating characteristics, such as reduced brittleness and greater conformability. Generally, MFCs are an advancement over active fiber composites (AFCs), which themselves represent an improvement over first generation piezoelectric fiber composites (PFCs) [4]. This particular technology was selected for its fast response and high bandwidth nature, which are critical in active structures.

In conventional aircraft, roll authority is achieved through movement of rigid aileron flaps near the wing tips. Electromechanical (servo) or hydraulic motors articulate the flaps to impart an effective change in camber [5], and alter the lift at this position of the wing. In turn, an aircraft experiences a moment about its roll axis (a coupled yaw moment also results if not trimmed). A thin wing found on an MAV provides no easy integration of aileron-flap motors. On the other hand, MFCs are only around 0.3 mm thick; a beneficial trait for use on thin wing aircraft. Mechanical linkages exterior to the wing can be costly in terms of drag, weight, and power. The discontinuous joint created by the wing-flap interface adds more drag. Embedded MFCs employ a bending motion to change wing camber, increasing the lift coefficient and system performance over servomechanisms. The resulting airfoil shape is continuous and more aerodynamically efficient. Maneuverability is improved if the underlying structure is optimized for high frequency outputs.

1.2 Motivation

This thesis seeks to apply the foundation of available theories, software tools, and proper experimentation to a morphing airfoil so that an optimal active structure is designed. Actively cambered airfoils have the possibility to offer performance enhancements, but traditional design methods are not unanimously applicable. It is the purpose of this work to validate and augment the processes pertaining to thin morphing airfoil analysis. To this end, a systems level approach is used that will consider all aspects of integrated MFC development. Elements of aerospace, mechanical, and electrical design constitute the three primary facets of development. This thesis will make use of a unique method to attain predictions on piezoelectric based camber changes. Aero-structural effects will be studied with a newly defined process and implemented with a common finite element package and aerodynamic predictive software. New hardware to drive MFC actuators will be presented to fulfill power supply requirements. Wind tunnel experimental results will enable comparisons with predictions to ascertain model accuracy. To the authors knowledge, no previous work has been attempted to encompass each of these aspects from the conceptual to testing stages using this method.

Chapter 2

Literature Review

Morphing wings concepts can be manifested variety of ways. All deviate from the notion that the wing needs to be a rigid structure with fixed geometries. Wing area, sweep, dihedral, and camber are just some of the parameters with the potential to be changed by infrequent or continuously variable mechanisms. Much focus has been placed on actuating control surfaces, which offer the greatest capacity for performance improvements. This is a form of maneuvering morphing, wherein the wing is changed to enhance flight control and performance. In other morphing concepts, entire wing sections may fold unto themselves or may reconfigure at a more infrequent basis. This expands the flight envelope to include many distinctive missions achievable with a single platform. These are forms of configuration morphing, which effect large changes in vehicle inertia, stability, and again performance. Select examples are provided from the previous work of other researchers.

All morphing concepts open the door to a number of challenges involving structural and aerodynamic design. Sophisticated analytical techniques have been used [6] [7] for modeling piezoelectric stuctures, but they are difficult to use quickly for simple designs. This has generated interest in modeling morphing effects with traditional finite element tools. A few methods used in this work are presented here.

2.1 Active Wing Structures

2.1.1 Maneuverability Morphing

Use of piezoelectrics to effect wing shape control is not new. Vos, Brueker *et al* [8] demonstrated morphing wing flight control via precompressed actuators on a unique semi-rigid skinned airfoil. This thick airfoil combined a stiff NACA 0012 D-spar with a compliant skin/bender mechanism on the aft portion of the 5.7 in chord. The dynamic motion of the bender and skin was modeled using a the Rayleigh-Ritz method, Euler-Bernoulli beam theory, and classical laminate theory (CLT). A net trailing edge (TE) deflection of 3.1° delivering a C_{L_α} of 1.72/rad was attained in wind tunnel tests. The system was subsequently flown on a subscale UAV which exhibited a large gain in control authority.

Bilgen [9] developed a lightweight MAV with unimorph actuators. His initial investigation used a Rayleigh-Ritz model to approximate structural deflections from MFCs. These results were used to design the airfoil on a 0.76 m wingspan MAV, which demonstrated the validity of thin cambered wings for use with MFCs. In flight testing, the durability of the flight control devices came to light when numerous crash incidents were experienced. The structural integrity of the MAV proved resilient and maintained sufficient roll control authority.

More recently, Bilgen [6] characterized a multitude of piezocomposite airfoils. These had various implementations of MFC actuators, including unimorph and bimorph configurations used for camber change and flow control. Compared to other piezoelectrics, he found MFCs to be the most versatile, with other monolithic piezoelectric devices suffering from excessively brittleness. Thin and thick airfoils were investigated for 2D lift and drag coefficients in low Reynolds number flow. He demonstrated a maximum L/D of 17.8 for a flat plate airfoil with two M8557-P1 bimorphs. This thin airfoil had a minimal 1 mil thick stainless steel substrate and was able to maintain deflections under speeds around 45 m/s. The efficacy of a compliant box-spar mechanism on a thicker airfoil was substantiated. Camber control was not the sole focus of his work. Bilgen also studied the use of MFCs for flow control. By exciting small MFCs near the leading edge (LE) of his airfoil at 125 Hz, a $C_{l,max}$ gain of 27.5% was obtained. Additionally, various forms of high voltage drive circuitry are explored, some of which are used in this thesis.

Using a Selig S1210 thick airfoil, Ohanian *et al* [10] introduced a novel design of trailing edge camber control with MFCs. He cited the need for a solution to the separation inducing

flaps of traditional micro air vehicles at lower Reynolds numbers, pointing out the most prominent benefits of MFCs, such as reduced drag, minimal added volume, and increased relability due to less moving parts. The unique design includes numerous features meant to prevent aerodynamic pressures from inhibiting the deflections from embedded bimorphs. Aileron deflection tests demonstrated both the potential for large displacement amplitudes and hysteresis effects of the actuator. Suggestions for open and closed loop control are made in dealing with the hysteresis nonlinearities. Aerodynamic predictions based on experimental bimorph deflections showed a possible ΔC_l of 2.25 due to MFC input, exceeding that of a servo-actuated flapped airfoil.

In designing for camber morphing, Gandhi and Anusonti-Inthra [11] looked into the implications of control surface stiffness on actuation. They noted it is advantageous to have "low in-plane axial stiffness but a high out-of-plane flexural stiffness," the purpose of which is to afford a reduction in the demands of camber change inducing technology (MFCs, SMAs, etc.). They discovered a lower limit on these values that should be observed for reducing undesirable deformation. The relevance of the paper deals with the tradeoff between rigid structures that are capable of high aerodynamic loads and more flexible structures that allow for high bandwidth technology to actuate them.

Kudva documents the DARPA Smart Wing [12] program as it has evolved since its inception in 1995. This project was initiated to work on the application of smart materials to improve the performance of military aircraft. Performance metrics were based on aerodynamic and aeroelastic improvements. The article covers the two phases of the project that have since been completed. Phases I and II both saw experimentation with Shape Memory Alloys (SMAs) to actuate control surfaces. Early efforts brought out the bandwidth issues of SMAs. During the second phase, a 30% scaled design with LE/TE active material appointments was tested over a range of Mach 0.3 to 0.8, and resulted in significant performance improvements (lift, roll rate). At such high dynamic pressures, the ability to retain control through use of LE actuation at reduced aileron effectiveness was noted. The second phase of the Smart Wing Project saw a UAV prototype that delivered a roll rate of 80°/s. Another highlight is the durability of the smart material designs. Kudva notably mentions that the "[Smart Wing's] control surfaces showed no degradation in performance during the three weeks of wind tunnel testing."

One of the largest projects undertaken in active wing development involved the Active Aeroelastic Wing (AAW) program [13] by NASA, the Air Force Research Laboratory (AFRL), and

Boeing. The wings of an F/A-18 aircraft were re-engineered with a combination of thin aluminum and composite panels. The key parameter of effective wing torsional stiffness, which enables active aeroelastic control, was experimentally determined. Overall stiffness decreased 17% from a standard F/A-18 wing. Leading and trailing edge control surfaces were driven by hydraulics at lower dynamic pressures. Control at higher speeds was achieved with twist enabling "tabs", to design around the common, albeit expected, aileron reversal issue at higher Mach numbers. A new flight controller was developed by Boeing and NASA for the AAW aircraft. An FEM delivered flutter predictions. Ground vibration testing matched modal frequencies from the FEM with good accuracy. Roll data from in-flight testing at Mach numbers between 0.8 and 1.2 demonstrated roll rates comparable to and sometime exceeding that of traditional control surfaces. As one of the first forays into active wing structures on a full scale air vehicle, the program has provided valuable insight in the multidisciplinary requirements in active aeroelastic design.

2.1.2 Configuration Morphing

The utility of piezoelectric actuators is not limited to morphing for improved maneuverability. Schultz [7] investigated their potential for snap-through shape changes, in which a laminate substrate could be forced (snapped) into one of its multiple stable shapes. This would only require a momentary input on behalf of an MFC. His focus is on unsymmetric laminates. Due to their inherent property of being easily transformed into a new shape, they lend themselves well to configuration morphing. To make predictions on the resulting shapes, he applies classical laminate theory in combination with the Rayleigh-Ritz technique. He was able to accurately predict snap-through behavior (resulting displacement fields) after continually refining his model to include sensitive parameters such as final ply thicknesses and orthotropic material properties. After fixing these issues, he emphasizes concerns with piezoelectric and material nonlinearities.

Bowman *et al* [14] list the developments eminating from the Morphing Aircraft Structures program from DARPA/AFRL/NextGen (NMAS). Thus far, the work has addressed potential benefits, important design features resulting from the program, wind tunnel tests, and operational considerations. The flight envelope of a UAV usually falls under one or more of the following modes: survive, attack, and loiter/reconnaissance. The authors attempt to determine the optimal form of shape changes to most effectively operate in all three modes;

this is based on mathematical criterion examining the factors of loiter, dash times, and fuel weight penalties. The NextGen morphing wing concept is then reviewed. A "batwing"-resembling concept was ultimately chosen for the large range of attainable geometries. Skin flexure was found to be the most critical design aspect. The tradeoff between adequate flexibility and retaining flutter/ divergence margins was mentioned, but not detailed. What emerged from this phase was a wing capable of an adjustable wing sweep between 15-45° and half-span of 7-10 ft. Uniquely, sweep and planform could be varied independently by hydraulic actuators. Wind tunnel testing was completed at the NASA Transonic Dynamic Tunnel, and met objectives such as operation under 2.5 G loading and transonic dynamic pressures.

A 9.3 ft wingspan UAV designated Morphing Flight-vehicle Experimental 1(MFX-1) [15] was developed by NextGen Aeronautics from the ground up to assess the practicality of in-flight configuration morphing. An electric motor was employed to adjust wing sweep between 15-35°. Coupled movements from actuation simultaneously altered planform area by up to 40%. This platform was successfully tested in speeds up to 120 knots. The impetus for this project was derived from the NMAS program, which identified the need to characterize individual morphing technologies before incorporating a suite of components onto a platform.

2.2 Finite Element Modeling of Piezoelectrics

In 1993, Hwang and Park [16] offered some of the first finite element code relating to piezoelectric materials. The initial purpose of their research was modeling the piezoelectric effect in two dimensional structures; as opposed to inefficient solid elements or analytical models used by others at the time. A quadrilateral plate element with a single electrical degree of freedom was presented. This element was to represent the electromechanical responses for both sensors or actuators since the application involved feedback-based vibration supression. For actuators, element equations of motion were derived from Hamilton's Principle, the converse effect piezoelectric equation (stress as a function of strain and electric field - from constitutive relationships), and classical lamination theory. These were next discretized with the Kirchhoff technique. Solving the resulting equations with the example case of a PVDF bimorph cantilevered beam produced good agreement with static deflection predictions.

Côté *et al* [17] worked to develop static and dynamic models for piezocomposites in MSC/-

NASTRAN. They cited the need for a common method to be used in designing piezoelectric actuators bonded to composite structures, such as those used in the aerospace industry. They foresee the use of a computational tool to describe the active regions incorporating piezoelectric actuators and sensors. In this regard, a three dimensional model was used to gauge the accuracy of using thermal strains in FEA to represent the converse piezoelectric effect. Three dimensional elements were used in static and dynamic analyses. In their cantilevered beam example, they found excellent correlation between the finite element model results and numerical estimations. Experimental testing on dynamic behavior was less conclusive, and Côté postulated on the effects of insulating layers used in fabrication.

Reaves discusses the need to be able to quickly implement piezoelectric actuators using FEA [18]. In this regard, three approaches from previous research are outlined. The first involves use of the thermal analogy to represent actuator induced strain. A second approach from some researchers progressed to employing native elements incorporating the piezoelectric effect within MSC/NASTRAN. Lastly, the prospect of coupled field elements offered by ANSYS are of interest. Reaves indicates the need to validate these new methods with experimental validation. He take advantage of these modelling techniques to fully characterize piezoelectric systems with a focus on dynamic response. Overall, "global behavior" such as steady state displacement and reasonant frequencies were well correlated between the models and experiment. As with Côté [17], the bonding between actuator and substrate was exposed as critical issue contributing to reduced model accuracy. Apart from a few minor differences, the three approaches largely provided similar results.

Chapter 3

Mechanical Simulation with FEA

The following section will present the design and simulation methods for modeling MFC-actuated airfoils. Each aspect of the final model from geometry and material generation is discussed in detail. An electro-thermal analogy is derived to recreate the piezoelectric effect in simulation. This culminates in an NX Nastran-produced [19] solution, which is compared to experimental results in later chapters. NX Nastran is a commerically available software tool built upon the NASTRAN code database developed by NASA [20]. Finite element modeling is a practical method of delivering fast predictions for complex geometries, allowing a broader scope of design areas to be investigated.

3.1 Airfoil Selection

The airfoil of interest is from the GenMAV, an aircraft design eminating from the AFRL but evolved from a University of Florida design [21]. Its purpose is to test concepts related to MAV design. The thin, cambered airfoil belonging to the GenMAV has a chord length of 5 in and was optimized for a low Reynolds number flight regime ($8 \cdot 10^4 - 2.4 \cdot 10^5$). The MAV design specifies a 24 in span and incorporates various 3D features such as a dihedral angle and an elliptical planform, the effects of which are not the immediate focus of this work. In later analyses, the airfoil coordinates are imported into NX using a 7th-order spline.

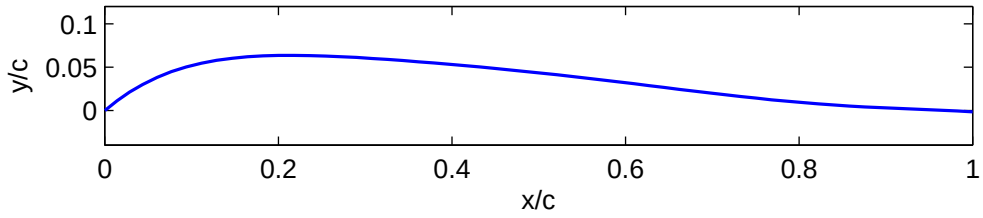

Figure 3.1: The GenMAV airfoil shape.

3.2 Macro Fiber Composites Properties

A rectangular coordinate system is most suitable to represent MFC dimensions. Verification of proper alignment is critical for non-isotropic materials. The X-axis and Y-axis are aligned with the longitudinal (PZT fiber) and transverse (electrode) directions, respectively. Figure 3.2 correlates to the material property directions given in Table 3.1.

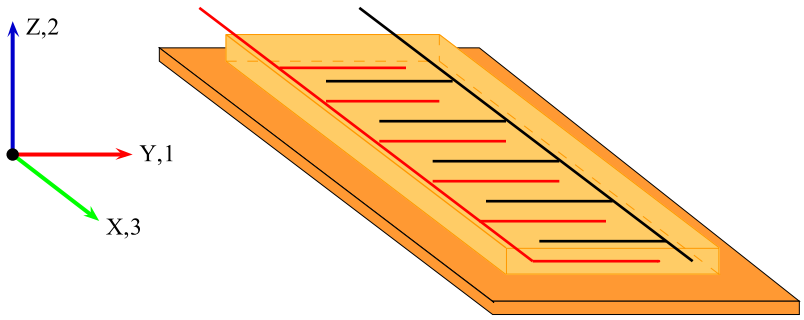

Figure 3.2: Reference directions for thermal analogy with respect to the alignment of electrodes.

The piezocomposite MFC material is not isotropic in nature. It is instead known to be orthotropic, in which the material properties are defined by the three orthogonal directions. Relevant orthotropic properties of MFCs have previously obtained by derivation and experiment and are well established [4] [9]. These are listed alongside values provided by the manufacturer in Table 3.1.

Macro Fiber Composites and their composite substrates are assumed to act in the linear elastic regions of their respective materials. No loading from the actuators or aerodynamic forces will be designed to take the material beyond the elastic region.

Table 3.1: Orthotropic properties of the MFC actuator by various sources.

Property	**MFC Datasheet [3]**	**Williams [4]**	**Bilgen [9]**
E_x (GPa)	30.34	29.4	30.7
E_y (GPa)	15.86	15.2	14.4
G_{xy} (GPa)	5.52	6.06	4.10
ν_{xy}	0.31	0.312	0.267

Macro Fiber Composites are electrically equivalent to capacitors. Input voltages range from -500 V_{DC} to 1500 V_{DC}. Although voltage requirements are relatively high, current draw is quite low. Actual current draw is dependent on the form of drive circuitry (see Chapter 4). Table 3.2 displays the electrical properties of the three different actuators used in this thesis. Each product is offered by Smart-Material Corporation [3], Sarasota, FL.

Table 3.2: Electromechanical properties of the MFC actuator.

Model	**Length(mm)**	**Width(mm)**	**Cap.(nF)**	$\mathbf{V}_{RANGE}$**(V)**
M4010-P1	40	10	1.00	-500→1500
M8514-P1	85	14	3.00	-500→1500
M8528-P1	85	28	5.70	-500→1500
M8557-P1	85	57	9.30	-500→1500

3.3 Composite Substrates

The core morphing wing design involves embedding MFCs into a wing to effect a change in shape and gain favorable dynamic characteristics such as high roll control. As this calls for an embedded actuator, special attention must be made to the material stiffness. The actuator should function within design limits without experiencing excessive restriction in the actuation direction. This compliance must also not be so great that the wing flutters under normal operating conditions. Composites are the obvious substrate choice because they can be tailored to the unique design requirements. Another benefit is the high strength-to-weight ratios.

Due to the significant effect of substrate properties on actuation characteristics, an extended derivation into the stiffness properties of composites laminate can be found in Appendix A. A MATLAB program was written to quickly determine the sensitivity of material properties to various ply schedules. The ply schedule specifies the construction of the stack of layers within a laminate, including (but not limited to) stacking sequence, ply orientation, ply thickness. Figure 3.3 gives the reference directions and angles used with discussion of laminate properties.

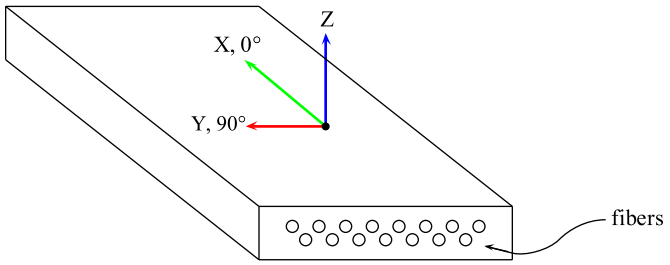

Figure 3.3: Illustration of laminate coordinate system with respect to fiber directions.

When designing the ply schedule of the substrate, a few considerations are made. In a symmetric laminate, the ply schedule is mirrored about the middle surface. For these laminates, the bending-extension coupling matrix (B_{ij} matrix of Appendix A Equation A.12) is zero. This prevents bending from MFC actuation from inducing any coupling effects. Since the wing structure is active by design, large deflections in an antisymmetric substrate could produce undesirable geometry changes. An induced curvature is the only effect related to camber control, so symmetric laminates are chosen for this suitable behavior.

Candidate materials for the composite substrates include E-Glass, S-Glass, and standard modulus carbon fiber. E-Glass, or electrical-glass, is used in structural applications demanding low to moderate stiffness. Conveniently, the high resistivity and low dielectric [22] of the fibers lends itself well to insulating embedded MFCs. S-Glass is both stiffer and stronger than E-Glass. An intermediate/ standard modulus carbon fiber is significantly stiffer and stronger than either of the glass products. Isotropic properties of theses materials are outlined in Table 3.3.

Two dimensional elements are appropriate for modeling the behavior of laminates in FEA. Since ply thicknesses are generally thin, a three dimensional model would require an inordinate amount of elements to prevent poor aspect ratios. Only one material could constitute

Table 3.3: Relevant engineering properties of the constituent laminate materials.

Material:	**Tensile Modulus (GPa)**	**Tensile Strength (GPa)**	**Poisson's Ratio**	**Density (kg/m^3)**
E-Glass (Fiber) [23]	72.4	3.45	0.22	2540
S-Glass (Fiber) [23]	85.0	4.80	0.22	2480
Std. Carbon (Fiber) [23]	230	3.53	0.20	1750
Epoxy Resin [24]	2.81	0.054	0.236	–

each element. These restrictions would normally demand an elaborate model that accounted for each separate ply in single-element thick sublaminates. Instead, the built-in NX laminate modeler[1] creates a physical property which can be applied to a 2D mesh. Within the modeler, ply materials, scheduling, and thicknesses are specified. The entire analysis only covers macroscopic effects such as displacement characteristics. Directly modeling the fiber-matrix interface would be time consuming and is unnecessary. Instead, an homogeneous layer is used to represent each ply.

Figures 3.4 - 3.5 feature the variation of orthotropic properties as a woven layer is rotated between $0° \leq \theta \leq 45°$ only. Beyond this angular range, the variation is symmetric for $45° \leq \theta \leq 90°$ and then repeated for $90° \leq \theta \leq 360°$. The variation of in-plane elastic moduli E_x^b and E_y^b show not much difference between E-Glass and S-Glass, but a large jump in stiffness with carbon fiber. The largest disparity occurs for a ply orientation of $0°$.

The difference between shear moduli and Poisson's ratio is largest at the $45°$ ply angle, although very little shear deformation is expected for the thin laminates used as substrates. These plots used ply stiffness properties from Table 3.4 using the process detailed in Appendix B.

[1]The NX Laminates module optionally generates elastic moduli from constituent materials, but this functionality is not used in this work.

Table 3.4: Orthotropic properties of various singles layer laminate plies.

Ply Description:	$\mathbf{E_x}$**(GPa)**	$\mathbf{E_y}$**(GPa)**	$\mathbf{G_{xy}}$**(GPa)**	$\nu_{\mathbf{xy}}$
1 ply E-Glass 0/90° plain weave	23.71	23.71	3.10	0.09
1 ply S-Glass 0/90° plain weave	27.29	27.29	3.41	0.08
1 ply Std. CF 0/90° plain weave	63.72	63.72	3.31	0.04
1 ply Uni. Std. CF 0°	116.41	10.66	3.31	0.22

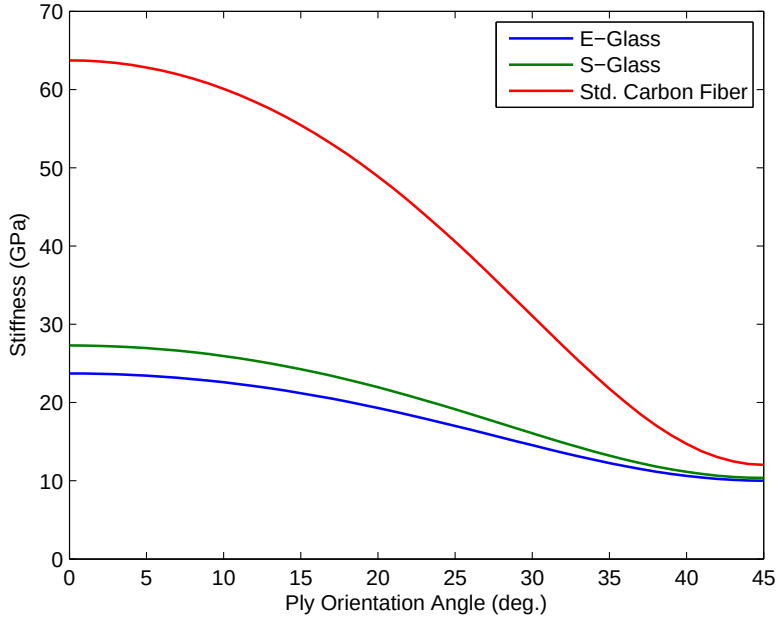

Figure 3.4: Variation of in-plane elastic moduli E_x^b & E_y^b for a woven ply of various materials.

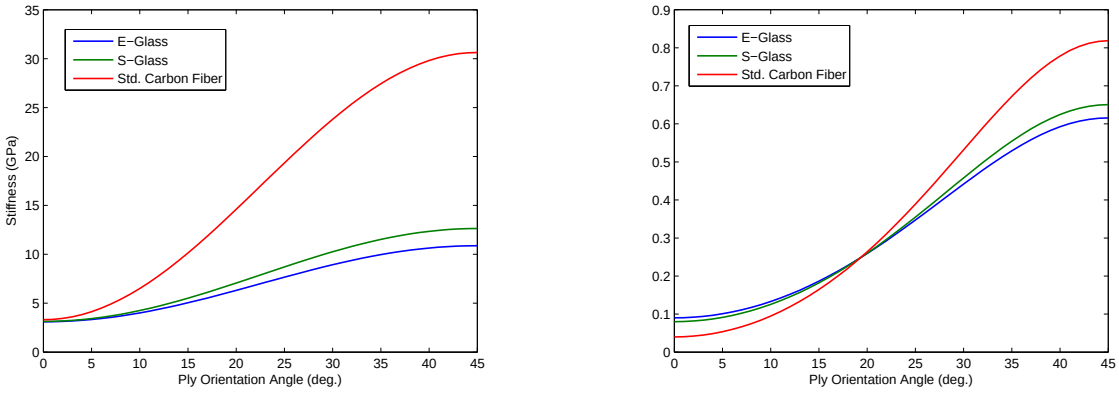

Figure 3.5: Variation of shear modulus G^b_{xy} (left) and in-plane Poissons ν^b_{xy} (right) for a woven ply of various materials.

3.4 Thermal Analogy

No method is available for directly modeling the piezoelectric effect in NX Nastran. The piezoelectric-based MFCs are modeled instead using a thermal analogy. This derivation uses a temperature input to represent the stress normally induced by placing a voltage across the MFC leads. Although the physical properties of the piezocomposite devices are in fact a function of temperature, this analysis will assume temperature effects are negligible compared to the piezoelectric coupling effects. Starting with the constitutive equations for piezoelectrics:

$$S = s^E T + dE \tag{3.1}$$

$$D = dT + \varepsilon E \tag{3.2}$$

In the first equation, S is strain, s is the material compliance (the superscript E denotes a short circuited condition), T is stress, d is the piezoelectric coupling coefficient, and E is electric field. In the second equation, D is electric displacement, ε is the dielectric constant.

In this form, strain and electric displacement are functions of stress and electric field, though this can easily be inverted to switch the independent and dependent variables. The simple form of these equations is arrived under the assumption that the constants s, d, ϵ do not to vary with stress or electric field. In reality, each coupling mode will saturate beyond the linear region [25], but for this analysis those terms are still considered linear. Since an important figure of merit for MFCs is the piezoelectric coefficient d, nonlinearity in this value will be assessed in later analysis.

Equating strain induced by voltage to a simple strain induced by temperature:

$$\varepsilon_{voltage} = \varepsilon_{thermal} \tag{3.3}$$

$$[d]\{E\} = [\alpha]\Delta\Theta \tag{3.4}$$

Where α is the coefficient of thermal expansion and $\Delta\Theta$ is the change in temperature. Now, with V_3 as the only direction of applied electric field:

$$d_{3i}\frac{\Delta V_3}{\Delta_{el}} = \alpha_i \Delta\Theta \quad i = \{1, 2, 3\} \tag{3.5}$$

Where Δ_{el} is the effective electrode spacing (constant). Equation 3.5 may be also be expressed:

$$\begin{bmatrix} \frac{d_{31}}{\Delta_{el}} \\ \frac{d_{32}}{\Delta_{el}} \\ \frac{d_{33}}{\Delta_{el}} \end{bmatrix} \Delta V = \begin{bmatrix} \alpha_1 \\ \alpha_2 \\ \alpha_3 \end{bmatrix} \Delta\Theta \tag{3.6}$$

Ignoring the out-of-plane direction, renaming axes, and assuming 1:1 voltage to temperature input:

$$\begin{bmatrix} \alpha_x \\ \alpha_y \end{bmatrix} = \begin{bmatrix} \frac{d_{31}}{\Delta_{el}} \\ \\ \frac{d_{33}}{\Delta_{el}} \end{bmatrix} = \begin{bmatrix} \frac{-170pm/V}{0.459mm} \\ \\ \frac{-400pm/V}{0.459mm} \end{bmatrix} = \begin{bmatrix} -3.704 \cdot 10^{-7}\ V^{-1} \\ 8.715 \cdot 10^{-7}\ V^{-1} \end{bmatrix} \tag{3.7}$$

where α is the coefficient of thermal expansion in the x and y directions, d is the piezoelectric strain coefficient term in the fiber and electrode directions, and Δ_{el} is the effective electrode spacing. The technique of this analogy is to simulate each voltage step 1:1 with each degree of temperature difference. Since real temperature changes are not a focus, the coefficients of thermal expansion for substrates and surrounding materials were not used.

The piezoelectric strain coefficient is not constant, however, and can vary with the magnitude of the electric field or stress. For simplicity, a distinction can be made between high and low electric fields. The manufacturer's website [3] defines high field as those exhibiting greater than 1 kV/mm. Noting the effective electrode spacing is 459 μm [6] for the MFCs:

$$V_{\text{highfield}} \geq E_{limit} \cdot \Delta_{el} \tag{3.8}$$

$$V_{\text{highfield}} \geq 1kV/mm \cdot 459\mu m$$

$$V_{\text{highfield}} \geq 459V$$

The appropriate coefficient is used depending on the expected electric field. The change in the coefficient for high and low electric fields is documented in Table 3.5.

3.5 Finite Element Modeling of Piezoelectric Strain

For the purpose of verifying the thermal analogy method, multiple tests cases were investigated through finite element analysis. In its final form, the MFC actuation was implemented as camber control on a morphing airfoil. The initial focus was on the ability of this airfoil to create sufficient deflection from a neutral state.

Strain was modeled with 2D plate elements that represent the mid-surface of the real geometry in the thickness direction. This assumption carries thin plate requirements, including small out-of-plane thicknesses relative to in-plane dimensions. The actual theory used by the NX Nastran solver is Mindlin-Reissner plate theory [20].

The various configurations included a plain MFC actuator, bimorph, and airfoil embedded applications. Since the thickness of each configuration is small relative to span-wise and chord-wise directions, all models were comprised of 2D CTRIA3 triangular and rectangular CQUAD4 surface elements in NX Nastran to simulate thin plate behavior. Using plate elements is remains valid when MFCs are modeled with substrates, since they will always be thin materials as well. After meshing, an element shape check verifes there are no distorted elements that exhibit excessive aspect ratios, warping, or other maladies.

Resulting nodal displacements were compared with predicted behavior and experimental tests. Depending on the specific model, the TE deflection will often be used as a quantified measure of actuator effectiveness due to substrate ply schedule, MFC placement, or other implementation effect. Radius of curvature is also used as a means of comparison because predicted curvatures are constant lengthwise along the model for simple bimorphs. This is defined as the inverse of the curvature κ.

3.5.1 Application of Thermal Analogy

The first step in employing the thermal analogy is setting reference temperatures where necessary to 0°C. The choice of temperature units is arbitrary, given continuity with the

input temperature. Next, a thermal load numerically equivalent to the intended voltage is applied to the nodes of the model that represent the active area of the MFC device. Gravity was neglected for these test cases. The inactive area, primarily consisting of thin flexible Kapton/epoxy layers, was also neglected.

Depending on the magnitude of the expected electric field between MFC electrodes, a coefficient of thermal expansion representing either a high- or low-field piezoelectric strain coefficient is used. Table 3.5 gives the alpha values for the half-actuation range. Larger coefficients are used with high field input ($V > 459\ V$). These values are entered into the orthotropic properties for the MFC plies within the airfoil laminate model. Actuation level, occasionally given with a percentage, is an arbitrary designation. Here, full positive actuation (100%) symbolizes the input generating maximum downward movement of the TE or maximum camber for any configuration.

Table 3.5: Thermal expansion coefficients representing the piezoelectric effect for various voltages.

Act.(%)	$\mathbf{V_{MFC}^{Top}(V)}$	$\alpha_{\mathbf{x}}^{\mathbf{Top}}(\mathbf{10^{-7}})$	$\alpha_{\mathbf{y}}^{\mathbf{Top}}(\mathbf{10^{-7}})$	$\mathbf{V_{MFC}^{Bot}(V)}$	$\alpha_{\mathbf{x}}^{\mathbf{Bot}}(\mathbf{10^{-7}})$	$\alpha_{\mathbf{y}}^{\mathbf{Bot}}(\mathbf{10^{-7}})$
0%	0.0	8.715	-3.704	0.0	-2.905	1.235
12.5%	187.5	8.715	-3.704	-62.5	-2.905	1.235
25.0%	375.0	8.715	-3.704	-125.0	-2.905	1.235
37.5%	562.5	10.02	-4.575	-187.5	-2.905	1.235
50.0%	750.0	10.02	-4.575	-250.0	-2.905	1.235
62.5%	937.5	10.02	-4.575	-312.5	-2.905	1.235
75.0%	1125.0	10.02	-4.575	-375.0	-2.905	1.235
87.5%	1312.5	10.02	-4.575	-427.5	-3.341	1.525
100.0%	1500.0	10.02	-4.575	-500.0	-3.341	1.525

As this macroscopic model is enabled only by an analogy to a true physical phenomenon, limitations on the applicability should always be considered. Out-of-plane voltage variation is assume constant and zero. Clearly, the domain of this analogous effect should never exceed the input voltage limits of an MFC. Additionally, failure modes, operational lifetime effects, nonlinearities in electromechanical properties, and effectiveness of dynamic behavior predictions are not delivered here. The analogy was not formulated for sensing (direct effect) applications.

3.5.2 Bare MFC

Generally, an MFC actuator exhibits expanding or contracting motion. The actuation mode is controlled by the orientation of the electric field with respect to the PZT fibers. A bending motion will result from electrodes running normal to the fibers, whereas twisting occurs if the electrodes are at any angle offset from normal to the fibers.

A simple MFC is modeled without a substrate (Figure 3.6). Dimensions are taken from the active area of an M8528-P1 MFC. Although this is not a useful real world implementation, it is important nonetheless to verify the finite element model with proper constraints and loading. After the geometry is meshed, the laminate property is applied to the mesh. A temperature load of 100°C is given to each of the 102 nodes, with one fixed constraint on the center bottom node (shown at the left in Figure 3.6).

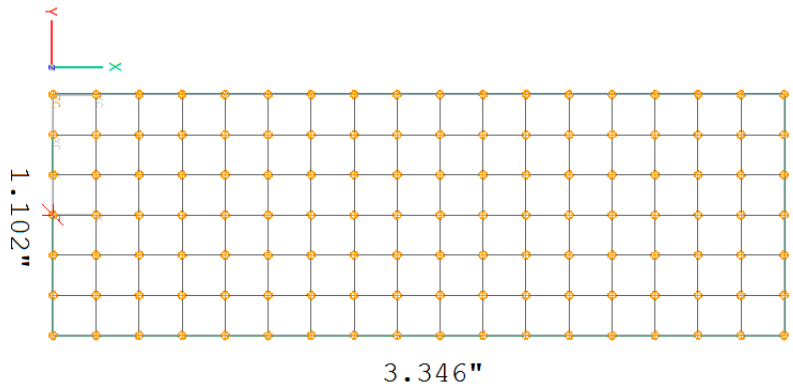

Figure 3.6: Bare MFC actuator with one fixed node and temperature-only loading (rotated 90°).

The predicted displacements in the X and Y directions are calculated with the temperature induced strain equation.

$$\Delta l_x = L_x(\alpha \Delta T) = 3.346 \cdot (-3.704 \cdot 10^{-7}) \cdot 100 = 2.916 \cdot 10^{-4}\ in.$$

$$\Delta l_y = L_y(\alpha \Delta T) = 1.102 \cdot (8.715 \cdot 10^{-7}) \cdot 100 = -4.082 \cdot 10^{-5}\ in.$$

$$\Delta l_{y/2} = -2.041 \cdot 10^{-5}\ in.$$

where Δl is the change in overall length and L is the original length given in the two directions.

The simulation is then solved with the single constraint SESTATIC101 solution type. Results are given in Figure 3.7.

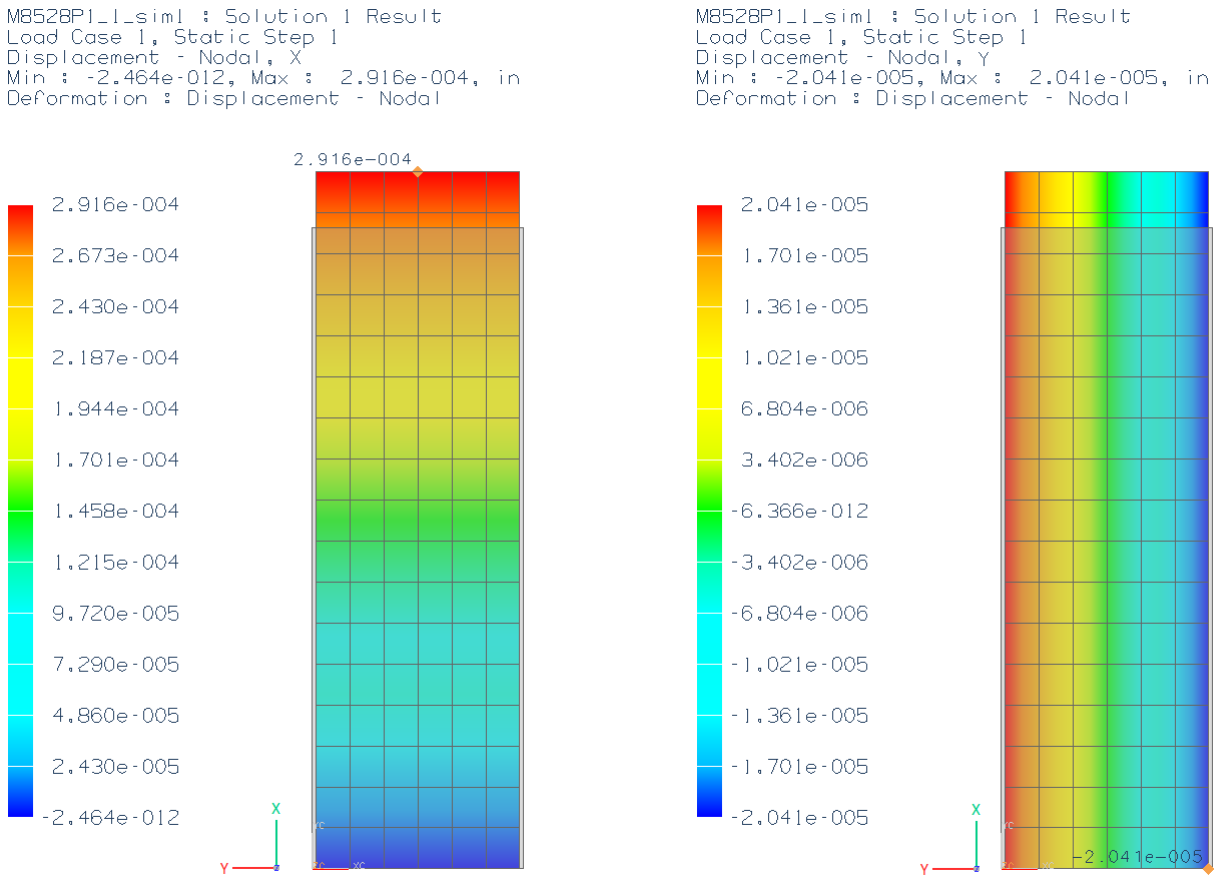

Figure 3.7: Bare MFC deformed (color gradient) and undeformed shapes (translucent gray). The physical displacement has been scaled by a factor of 1000 for better observation.

The total displacement of the MFC is $2.916 \cdot 10^{-4}$ in. in the X direction and the half-total displacement is $2.041 \cdot 10^{-5}$ in. in the Y direction. These values are in perfect agreement with previous hand calculations.

3.5.3 Bimorph Actuator

The term bimorph describes a configuration wherein two MFCs are bonded together. Constriction in one MFC and expansion in the other may be induced by means of specific voltage excitation. Initially, no substrate is added to the raw bimorph model. Thus, the laminate

construction is only comprised of two MFCs. This removes the possibility for any erroneous results from substrate property estimations. The bond between the layers is assumed perfect. Results are shown in Figure 3.8.

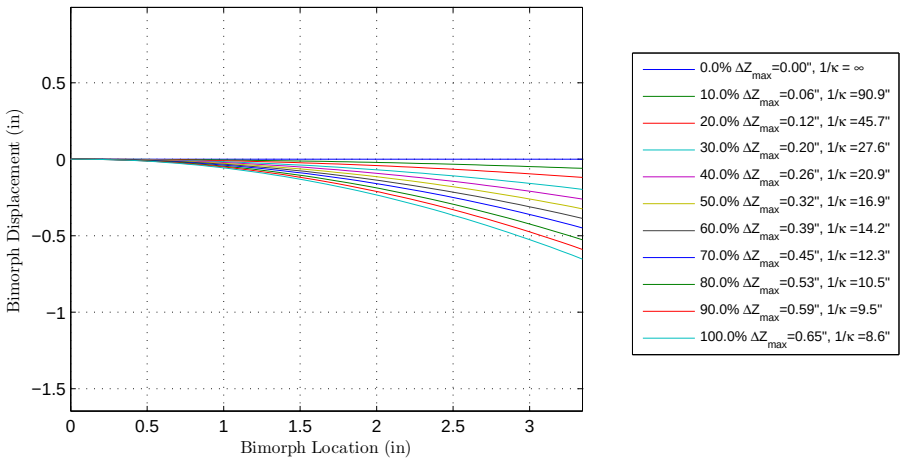

Figure 3.8: Predicted bimorph displacements from nonlinear solver. Tip displacements and curvature radii are given in the legend.

Large out of plane deflections evident from a bimorph make a good statement for the use of a nonlinear solver. Nonlinear structural analysis is required if a material is subjected to strains beyond its elastic limit. Another complication includes geometric nonlinearity. This situation presents itself when element displacements are large even though strain is still linear. In a bimorph, each MFC has a fixed wall boundary condition and only the coupled movement due to the bonding of the secondary MFC layer. For the static model-comparison tests, there is no external loading or substrate present, which normally constrain bimorph displacement. The largest predicted displacements are up to 20% of the original undeformed length. The CQUAD4 elements that comprise the bimorph mesh are compatible with the nonlinear static solution type NLSTATIC106 [20], which has the LGDISP parameter enabled to account for geometric nonlinearities. When processing, the solver creates subcases that incrementally load the part based on new geometry arrived at from previous (smaller) loads. This loading is of purely thermal form.

Results from the nonlinear analysis show slightly reduced displacements. This reduction is 8.1% of the original curvature at the maximum actuation, and 3.6% at 50% actuation.

3.5.4 GenMAV

Two distinct layers are created as 2D surface of the GenMAV airfoil that has a 5.25 in span and 5 in chord length. Refer to Appendix D for the coordinates of the airfoil shape. A laminate sandwich structure with an embedded bimorph is then defined. The CAD model of this is given in Figure 3.9. Table 3.6 documents the construction by breaking down the components of each laminate.

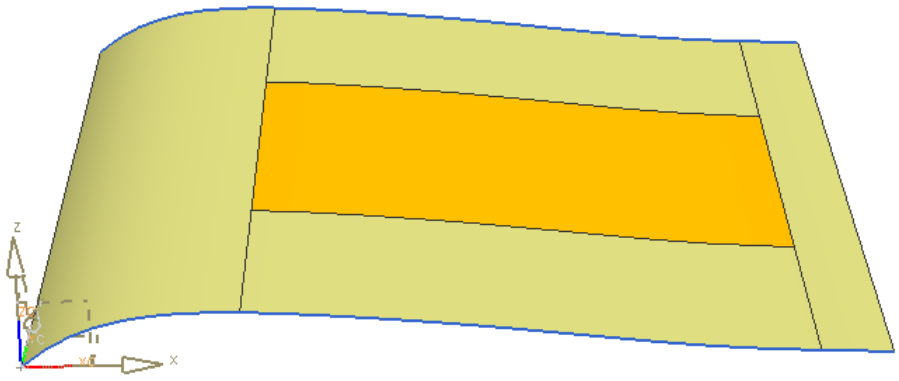

Figure 3.9: Raised side view of the GenMAV airfoil, the orange region representing the embedded MFC actuator.

Table 3.6: Construction of laminate by color region of Figure 3.9. Glass-epoxy (or fiberglass) is denoted as "G/E".

Region	**Ply**	**Material**	**Thickness**	$\alpha_{\textbf{thermal}}$
Orange	1	Top MFC	12mil	$\alpha_x^{top} \neq 0$ $\alpha_y^{top} \neq 0$
	2	(3.16+1.45) oz/yd^2 G/E	4.79mil	$\alpha_x = 0$ $\alpha_y = 0$
	3	Bottom MFC	12mil	$\alpha_x^{bot} = -\alpha_x^{top}/3$ $\alpha_y^{bot} = -\alpha_y^{top}/3$
Yellow	1	(3.16+1.45) oz/yd^2 G/E	4.79mil	$\alpha_x = 0$ $\alpha_y = 0$

Setting a particular temperature for the top and bottom active area nodes cannot be done separately, so the coefficients of thermal expansion are altered such that the induced strain is

not identical on the top and bottom physical surfaces. A bimorph creates a bending moment by inducing a positive and negative strain on the top and bottom surfaces, respectively. This issue is solved by negating and multiplying the coefficient of thermal expansion of the bottom MFC by one-third. In this manner, any temperature simulated as a positive voltage on the top MFC will be reflected by a negative voltage that is one-third of the top MFC voltage. This properly reflects how asymmetric voltage is applied to the actuator.

Two primary factors govern the capability of the actuator. Material stiffness comes from the elastic moduli, and the inertia component creates resistance to deformation. Beam curvature is inversely proportional to the bending stiffness term EI. The largest curvature would be experienced for the lowest material stiffness or inertia. Beam inertia is dominated by a cubed thickness term.

A simple airfoil model is shown in Figure 3.9. The surface where the MFC would be bonded to is the orange region, which follows the contour of the GenMAV profile. Two distinct surfaces are meshed with element edges of 0.1 in. All edges of the inner surface are coincident with the outer surface, and the edge nodes are shared. An example FEM is shown in Figure 3.10. Mesh density has been reduced to more clearly indicate loading and boundary conditions. A set of fixed nodes constrain the airfoil at a few edge nodes around the quarter chord to simulate the presence of a supporting structure. For later wind tunnel testing, this represents the load balance connection points. Nodes covering an area of around 0.01 in^2 are fixed to simulate these points, but this is exaggerated in Figure 3.10. The NLSTATIC106 solution type is used to solve for the static deflection condition.

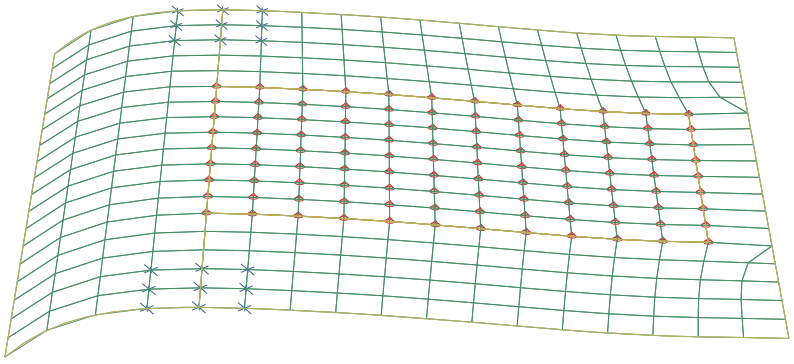

Figure 3.10: The finite element model showing placement of temperature loads and constraints.

A mesh sensitivity test was completed for the GenMAV airfoil under 45% actuation. Meshes

were applied to the 2D surfaces with element edge lengths ranging from 0.5 in to 0.075 in. Element sides with these lengths causes the number of elements to increase from 420 to 4830 after the automeshing. Sensitivity was quantified by observing the trend of TE deflection. Little variation was recorded, even after increasing element count by an order of magnitude, with the largest difference being 5.7%. This small difference can be attributed to the slight changes in fixed boundary conditions due to the various mesh densities; that is, the area (nominally 0.01 in^2) assigned fixed nodes is not always the same. A final value of 0.1 in (2600 elements) was chosen for all tests.

The full possible voltage (1500 V) is applied by setting the proper temperature of the second laminate area's nodes. After the NX Nastran solver has finished processing, the bulk deformation of the airfoil is observed in Figure 3.11. The gray translucent outline is the undeformed geometry.

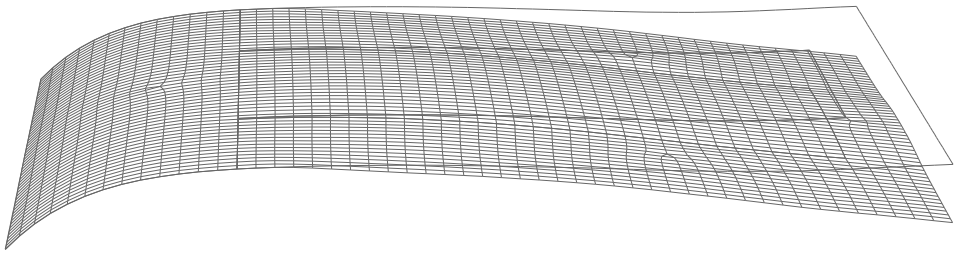

Figure 3.11: Side view of the embedded bimorph actuator.

Actuator effectiveness at four chordwise stations is observed by measure of TE deflection for three materials. Substrate ply schedule (thickness, orientation) is held constant. The predicted static deflections from the FEM are plotted in Figure 3.12.

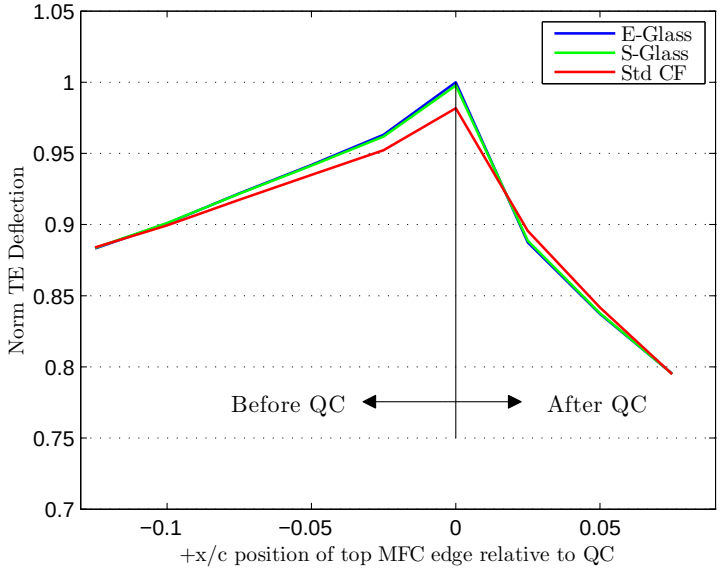

Figure 3.12: Maximum static deflection of the airfoil for actuator placement at various chordwise stations.

Placing the MFC closer to the quarter chord (QC) results in the greatest vertical stoke, and substrate material is not a significant factor. If the assumption is made that macroscopic mechanical effect is an equivalent bending moment, then it's easier to understand that this moment would be most effective at displacing the TE if it is applied at the fulcrum of the airfoil. Conveniently, a stiffer LE required to transmit lifting loads becomes the preeminant location for the front of the MFC actuator. After the chordwise position has been selected as the quarter-chord, the most dominant parameter is then studied.

Ply orientation has the largest effect for low substrate thicknesses. Displacement becomes mostly a function of thickness as that parameter increases. The predictions from Figure 3.13 are for E-Glass.

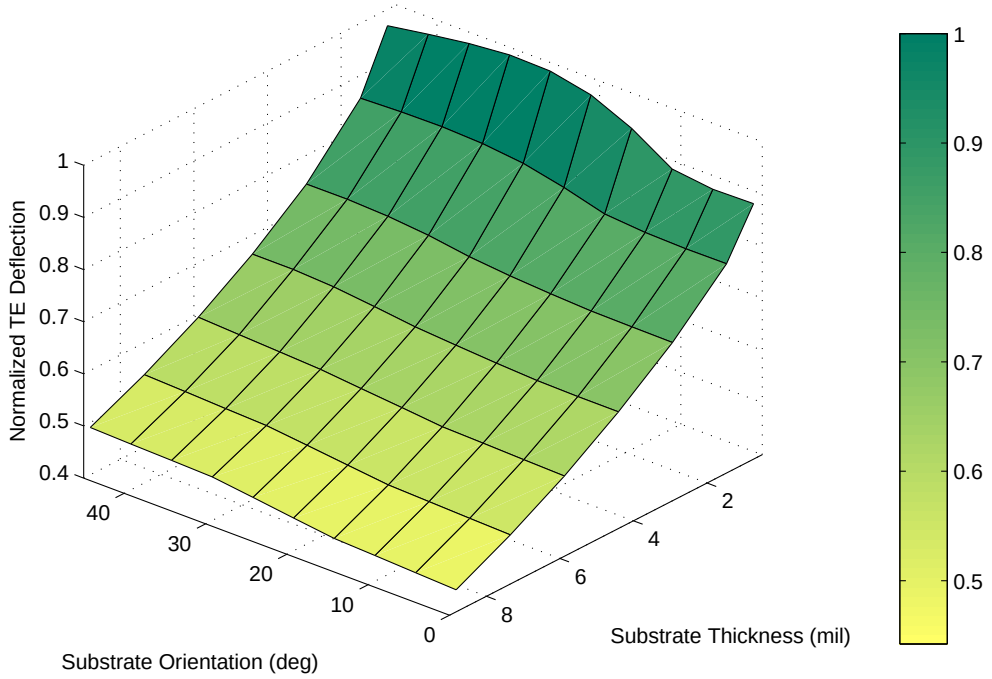

Figure 3.13: Maximum static deflection of the airfoil for various substrate orientation and thicknesses. Orientation angle is relative to the chord line.

Finally, Figure 3.14 shows maximum deflections for three materials and substrate thicknesses.

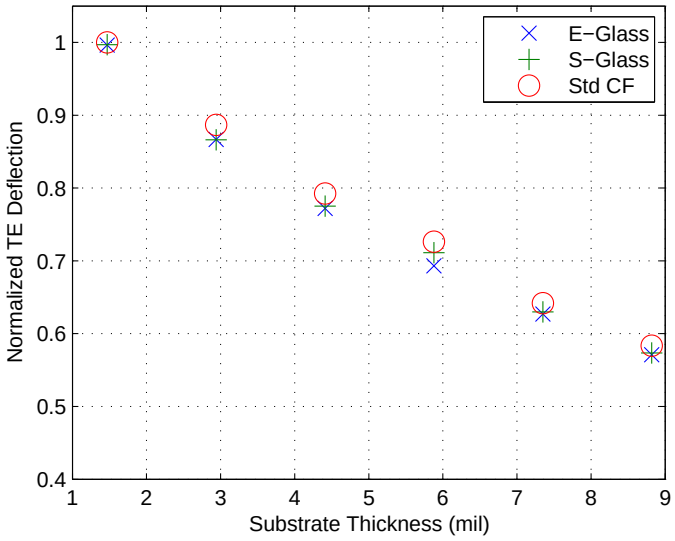

Figure 3.14: Maximum static deflection of the airfoil for various materials and thicknesses. Results are normalized to the greatest value within the plot.

Deflection does not seem to be a function of material. No optimal choice for thickness is evident beyond the minimum. This will later be shown to be driven by stiffness constraints defined by aerodynamic loading.

Chapter 4

MFC Driver Electronics

An important detail not to be neglected is the high voltage MFC drive circuitry. The key goal of the drive circuitry is to actuate a bimorph MFC. The bimorph structure induces a curvature by bending a beam with two actuators bonded on either side. Each individual MFC exerts a maximum deflection at 1500 V of excitation, and minimum deflection at -500 V. To drive the two MFCs in every bimorph simultaneously, multiple independent voltage supplies or a single supply with a unique voltage divider are required. The unique electrical requirements of the MFCs have contributed to an "electronics gap" in the past and warrant an extended look into circuitry that mitigates this issue.

4.1 Lightweight Circuit Prototype

As the airfoils presented here are designed for a small MAV, payload capabilities become a critical design point. In the laboratory setting, high voltage amplification is achieved with a 13.2 kg 80 W bench top power amplifier. More compact commercial amplifiers are available in power ranges around a few watts and weights around 50 g. This tradeoff is favorable, so long as the drive circuitry is efficient and does not demand large currents exceeding tens of milliamps. Due to limited market demands and recency of the MFC invention, there are no devices available to drive MFC bimorphs with small package electronics.

4.1.1 Lightweight Circuit Schematic

At the heart of the design are three DC-DC converters from AM Power Systems, Dayton, NV. These converters are single in, single out devices that operate in a manner such that output voltage is directly proportional to input voltage.

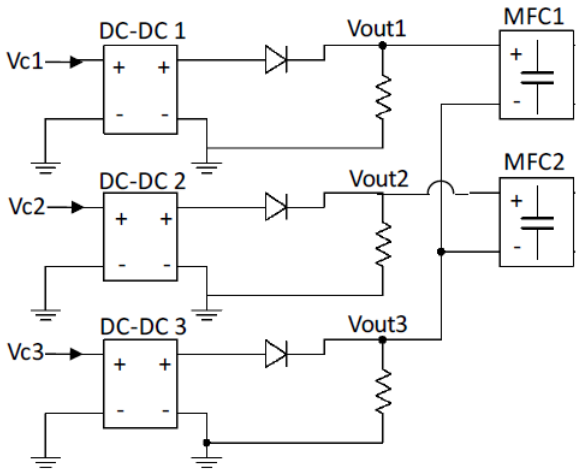

Figure 4.1: Electrical schematic of the lightweight MFC driver PCB (courtesy Bilgen [26]).

In this arrangement, the third DC-DC converter supplies a fixed voltage to the ground nodes of each MFC. This enables the other two converters to vary between 0 and 2000 V and therefore place between -500 V and 1500 V across the capacitive load of each MFC. Two analog output channels capable of 0-5 V_{out} and one fixed output are needed for control. Slope change at zero volts can be handled by software providing the control. Figure 4.2 demonstrates the voltage output trends produced by the circuit.

A limitation of the DC-DC converters is the minimum output voltage. Although the specified input range is 0 V to 5 V, the converters require at least 0.7 V to activate any output. The linear output region of the converters begins around 0.9 V, which translates to a minimum output of about 160 V. Note that the required changes do not affect the ultimate 1500 V and -500 V output levels for the MFCs.

Situations where the MFC is charging are expected to occur very quickly, due to the nature of the piezoelectric device. However, the system response when reducing the voltage across MFC nodes is a concern. Since the MFCs act as capacitors, bleed resistors are connected to drain the stored energy so that the physical deflection of the patch may decrease. Otherwise,

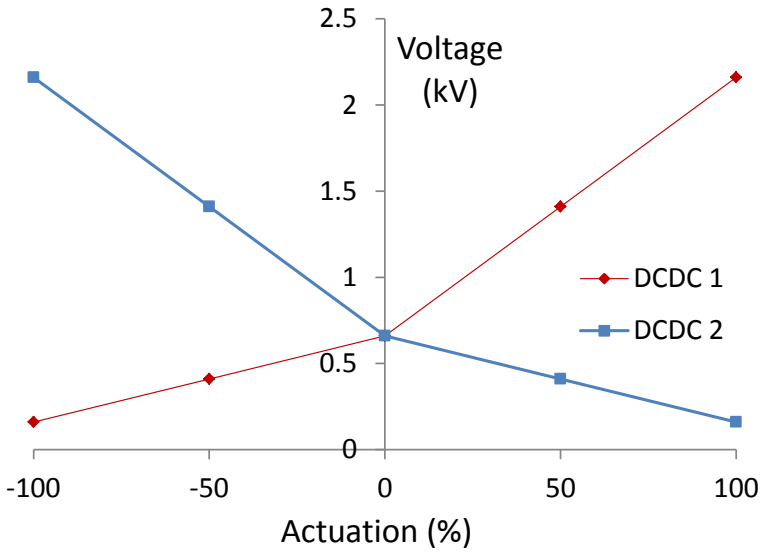

Figure 4.2: The output voltages of the two variable output converters over the actuation range.

there is limited control of the airfoil. Depending on the polarity of the voltage across their terminals, the MFCs may want to discharge electricity to the left or right DC-DC converter circuits. The diodes serve to prevent negative current from flowing through the converters and damaging them.

Diode selection is critical for circuit operation. They prevent the energy stored in the MFC patch from destroying the DC-DC converters when discharging. Proper selection requires studying the expected conditions across the diode terminals. Should a sufficient reverse voltage exist, the diodes could incur a reverse breakdown and they would allow harmful current to pass into the DC-DC converters. A $V_{br} \geq 5\ kV$ will protect against load faults.

Bleed resistors around 5 MΩ were chosen after initial circuit tests. This was the lowest resistance that allowed the DC-DC converters to reach the needed output voltage range. Each control channel also required a separate power buffer to decouple signal voltage and current draw from the control input.

The method for testing the control of an MFC actuated wing section starts with a LabVIEW VI that formulates the appropriate signals based on high level commands. Two analog out and one digital out channels of an NI USB-6009 DAQ then deliver these signals to the prototype circuit. This hardware could be packaged into a complete flight-ready solution so

long as provisions exists for PWM-analog conversion for remote control compatibily with commerical radio receivers. In a broader system level implementation with autonomy potential, a microcontroller with a multichannel digital to analog converter chip would replace the functionality of the NI DAQ.

4.1.2 Flight Weight PCB Design

If the unique voltage demands of the actuator cannot be satisfied by flight weight hardware, then MFCs will not prove to be a viable form of camber control. Using the commerical software program CadSoft EAGLE, the board in Figure 4.3 was developed as a proof of concept that minimized all hardware dimensions and weight. The initial version of the printed circuit board (PCB) weighed in at 32.5 g (for more details, refer to Appendix F). Seen in Figure 4.3 is a two-sided revision that takes advantage of surface-mount devices (SMDs). At half the size, this revision should bring the driver circuit weight to just 23.5 g. A matching schematic is located in Appendix F.

Length, width, and thickness of the PCB is 3.75 in, 1.55 in, and 0.062 in, respectively. These dimensions prove that this technology is in fact suitable for medium to large MAVs. Short, direct traces and full solder masks are present to minimize potential high voltage shorting. Additionally, a sizeable distance separates low voltage components from high voltage traces. As shown, only the footprint of each DC-DC converter daughterboard is indicated. These converters are not encapsulated to save weight. A weight breakdown of general equipment used in the class of 2 lb electric MAVs is given in Table 4.1.

Table 4.1: Weights of standard MAV equipment and lightweight driver PCB (sorted by percentage of overall weight).

Hardware	**Sample Product**	**Weight (g)**	**%**
Battery	EZ-Flite 351P 2600 mAh	200	60
Brushless Motor	Hacker A20-30M 150 W	45	13
Radio Receiver	Futaba FP-R127DF 7 Channel	40	12
MFC Driver PCB	–	32.5	10
Motor ESC	Castle Creations Phoenix-25	17	5
	total:	334.5	100

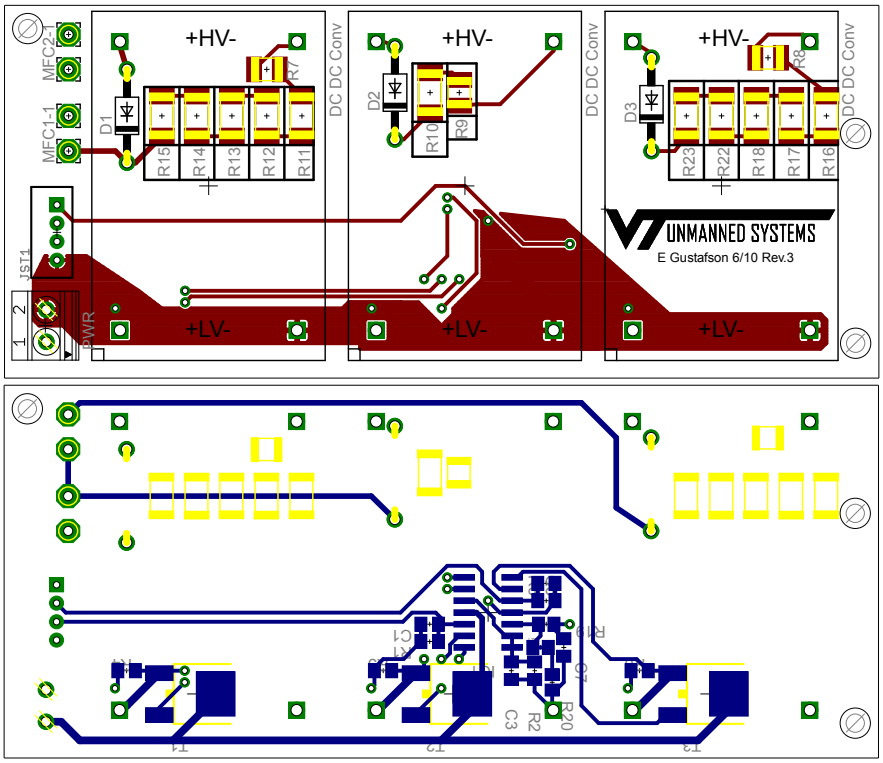

Figure 4.3: Top and bottom layers of the lightweight MFC driver PCB. Black, blue, and red colors correspond to silkscreen, top copper, and bottom copper layers.

The MFC driver PCB represents just 10% of the proposed final payload, or an increase of 11% from a non-MFC based system. Total weight of all electronics is 334.5 g (0.74 lb), or just under 37% of the MAV weight goal.

4.2 Experimentation Circuit

All test results given thus far are based on open loop voltage commands eminating from an NI DAQ analog output channel and conditioned through an amplifier and voltage divider circuit. The circuit in Figure 4.4 is used in all laboratory testing presented in this thesis. Less sources of error in output voltage are expected due to the singular voltage supply.

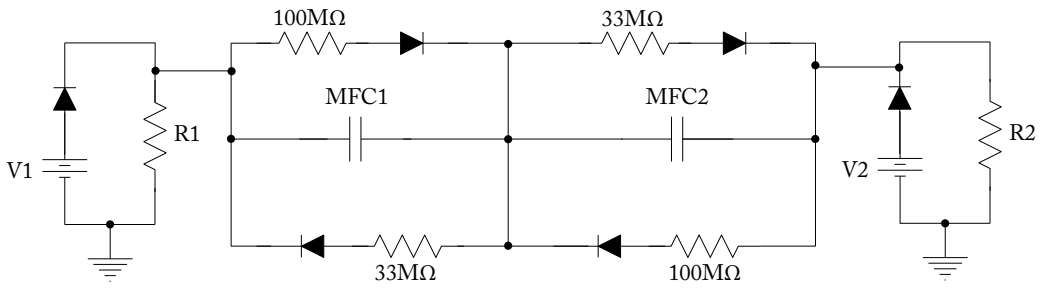

Figure 4.4: Asymmtetric voltage divider concept schematic (courtesy Bilgen [26]).

Instead of the two unipolar voltage supplies indicated by *V1* and *V2*, a single bipolar supply is used. Bipolar voltage outputs from the DAQ are amplifed by a Trek High Voltage Amplifier. The resulting voltage signal between -2 kV and 2 kV is then divided by the concept in Figure 4.4. Depending on the voltage polarity, the current direction and diode configuration dictate an asymmetric voltage division. For example, commanding full maximum camber to the airfoil-embedded bimorph brings the voltages across the top MFC to 1500 V but only -500 V to the bottom MFC. The reverse is also true; generating minimum camber is easily achieved by reversing the input voltage polarity, resulting in -500 V on the top MFC and 1500 V on the bottom.

Chapter 5

Static Actuation Testing

Static testing was undertaken to verify the degree to which the model can accurately determine the displacements of the piezoelectric actuator. Experiments were completed with a purpose-built rig capable of quantifying the entire deflection profile. These measurements are plotted against the model.

5.1 Experimental Setup

A custom measurement system (Figure 5.1) with a laser displacement sensor mounted on a computer numerical control (CNC) head is used to accurately measure the shape of the test specimen under various actuations. The sensor is a Microtrak II-SA with a LTC300-200-SA head delivering a resolution of ± 20 μm, which interfaces with an NI USB-6216 16-bit DAQ through an analog signal. The specimen is clamped at one end of the active area between two nonconductive acrylic plates that are bolted together. This serves to create a fixed condition which matches the model. The MFC is secured so that its thickness direction is orthogonal to gravity. Since only static deflection is of interest, the voltage input is stepped at arbitrary intervals over an arbitrary range (between $\pm 100\%$). At each actuation level, the distance between the specimen and the laser datum is measured along the middle of the specimen. This occurs as the laser beam from the offset displacement sensor is translated along the length of the specimen by the stepper motors of the CNC.

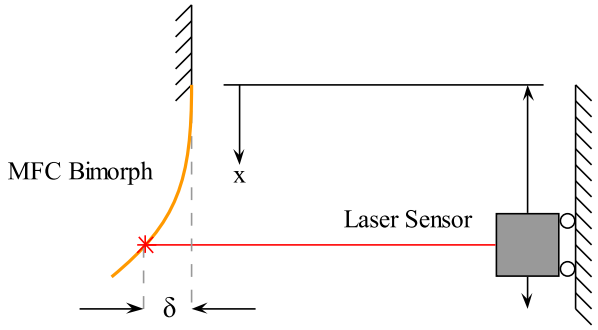

Figure 5.1: Experimental setup used to gauge bimorph shape under actuation for static deflection tests (not to scale).

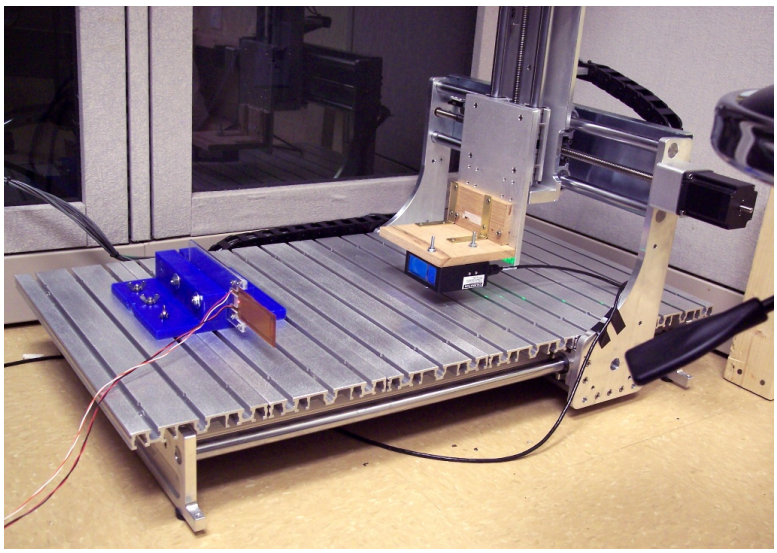

Figure 5.2: Bimorph mount (left) and laser displacement sensor (right) used for static deflection tests.

A Trek high voltage power supply combined with a custom circuit divider is used to drive the bimorph. The schematic may be seen in Bilgen (2010 [26]). This circuit produces the necessary bipolar asymmetric output to drive a bimorph up to its maximum input of 1500 V. As the Trek is capable of bipolar output (±2 kV), only this single supply is used. For more detail, see Chapter 4.

The divider circuit utilizing high power resistors delivers bipolar asymmetric output. The input and output voltages to this circuit for a test are recorded and shown in Figure 5.3.

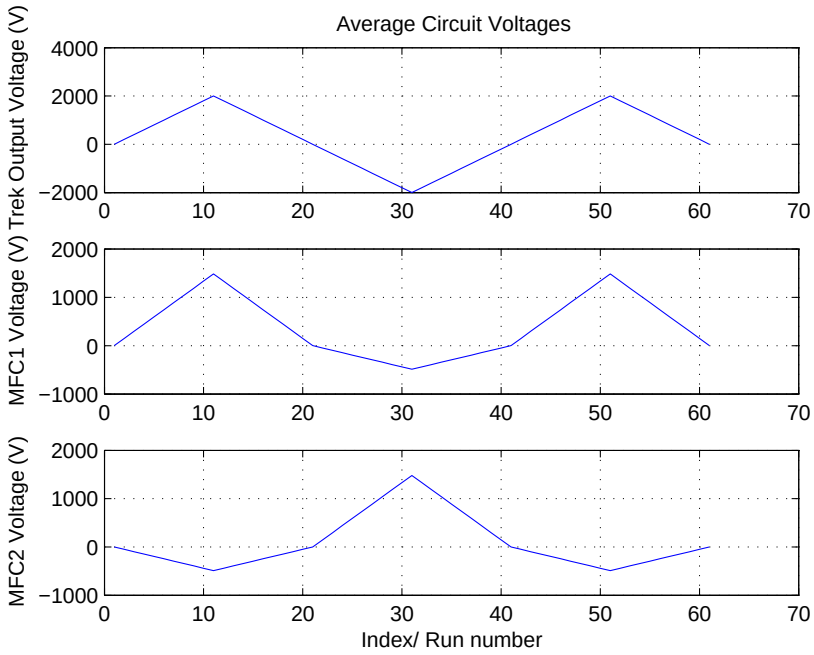

Figure 5.3: Voltage input (top) and expected outputs (bottom two) for the two MFCs in a bimorph.

This figure demonstrates the division of voltages between the top and bottom MFCs. In this test, the actuation is taken from 0% to +100%, -100%, +100%, and then back to 0%.

5.2 Model Fabrication

A bimorph was created by bonding two MFCs together with West Systems 105 epoxy. This bimorph was devoid of any substrate, and was cured under vacuum bagging against a flat plate. This set the neutral shape of zero camber. The actuator lacking a substrate will draw comparisons with the simplest two layer/ MFC model.

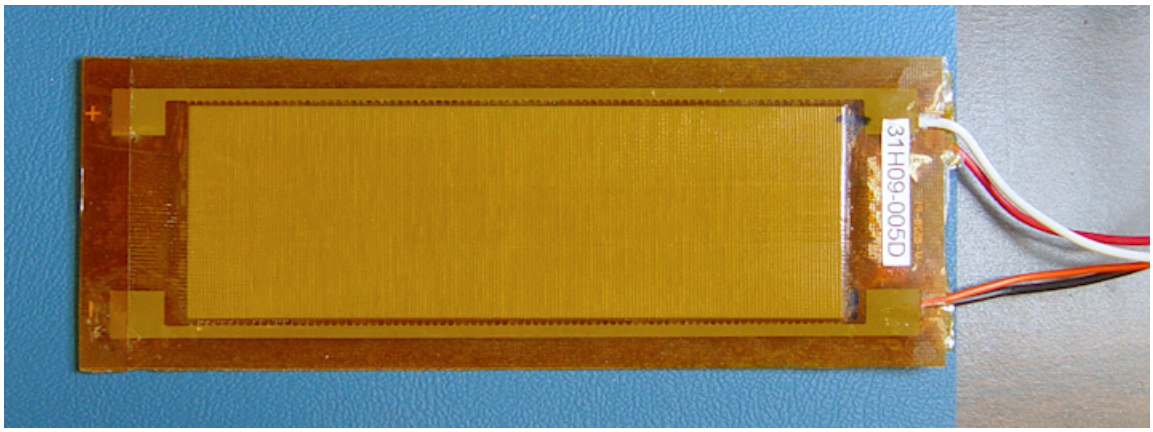

Figure 5.4: The zero camber bimorph used for model comparisons.

5.3 Model Comparison

The 100% actuation point was arbitrarily chosen for model comparisons. The zero camber bimorph was brought to this level by manual control, and the measurement process was initiated.

The first test's results (Figure 5.5) were promising; actuator curvature was within 3.7% of the model. Later tests showed increased output, even though no parameters are changed beyond the order and test date. Of concern is the unpredicted increase in output that occurs over testing intervals. The maximum strain evidenced by the large curvature induced by a bimorph actuator causes significant shear at the ply interfaces. In this case, each MFC represents one ply in a two ply laminate stack. Minimum curvature constraints (3.5 in when curled longitudinally [3]) were not exceeded. Laminate delamination is a byproduct of excessive loading, and manifests itself in small interlaminar voids. The increase in displacements could potentially be attributed to delamination, which directly reduces bending stiffness [27]. The bonding epoxy is a product normally used as the matrix in composite materials. Other researchers have used a high shear epoxies such as 3M DP460 [6]. Sizeable displacements from these experiments combined with poor binding could have overstressed the bond and allowed delamination. Shear stress is not transmitted through the voids, so the overall beam experiences reduced stiffness and more pronounced deflections.

A more complicated cause could be interconnected electric fields of the top and bottom MFCs. No electrical insulation is provided by the center thin epoxy or fiberglass layer.

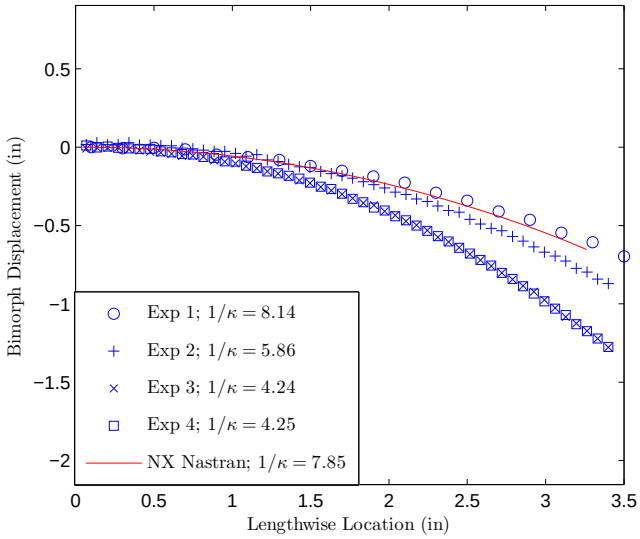

Figure 5.5: Bimorph deflection results of four tests under identical conditions but different times.

Applying an electric field to one MFC may also induce the piezoelectric effect in the other, given the inappreciable distance separating the MFCs. However, this does not explain initial model agreement.

These tests also expose the hysteretic nature of piezoelectrics. Each test begins at a completely neutral camber/ curvature corresponding to the point at the origin of Figure 5.6. The figure shows the maximum deflection results for the zero camber bimorph with the light fiberglass substrate. As the voltage sweeps up and to the right to 100%, a different deflection trend is seen than when the actuator is brought from -100% to 100%. This is because the trend is dependent upon the actuation history, and these are commonly referred to as distinctive “sweep up” and “sweep down” motions.

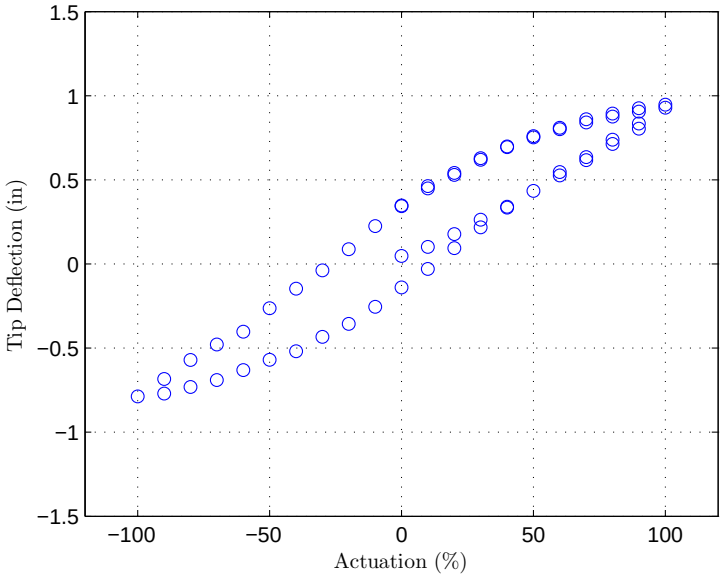

Figure 5.6: Hysteresis demonstrated during an actuation/voltage sweep $0\% \rightarrow -100\% \rightarrow +100\% \rightarrow -100\% \rightarrow 0\%$.

Any sort of MFC control architecture would ideally apply a transfer function between the input voltage and output strain or displacement. Unfortunately, the hysteretic response of piezoceramics is complicated and cannot be described by a simple transfer function. Hysteresis is a nonlinear property originating at a molecular level within the PZT fibers of an MFC. System output at any given moment is dependent upon the history of past inputs. The input-output plot in Figure 5.6 is characteristic of hysteretic materials. Past researchers [4] [6] have sought use of the classical Preisach model to account for hysteresis nonlinearities. Although hysteresis modeling is not a focus of this work, it is an important consideration used during testing. To "reset" an MFC actuated device, all hysteresis effects must be erased. This is accomplished via the "wiping-out" property that uses a peak to peak sweep of inputs so that the states consistently begin at the same value (neutral/zero displacement).

Chapter 6

Aerodynamic Analysis

Aerodynamic characteristics are critical in quantifying the effectiveness of this form of morphing control. In Chapter 3, actuation ability was predicted with no external forces. Now, flow distributions will be used to predict airfoil geometry under aerodynamic loading. The common software package XFOIL is used in this regard to accurately predict real world capabilities.

6.1 XFOIL

The aerodynamic characteristics of the thin, cambered GenMAV airfoil were identified with the XFOIL v6.9 program. XFOIL utilizes a combination of the traditional panel method with compressibility corrections and the integral boundary layer method to solve for viscous solutions. As a result, XFOIL can be used to accurately predict 2D airfoil characteristics in low Reynolds number (Re) subsonic flow.

6.2 GenMAV

GenMAV airfoil coordinates shown as smooth splines are given in Figure 3.1. Unfortunately, XFOIL has a known difficultly with obtaining the flow around thin airfoils with thicknesses less than 1% of the chord (XFOIL documentation [28]). When the raw coordinates are imported into the program, panels are auto-generated between the points in Figure 6.1.

The original set of coordinates results in 116 panel nodes and a maximum panel angle of 51.3^o, which XFOIL then flags as excessive. While the number of panels along the top and

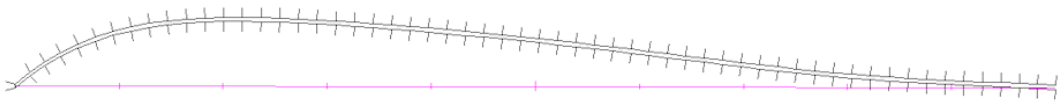

Figure 6.1: XFOIL panel distribution from raw coordinates import.

bottom surfaces may be sufficient, more attention is placed on the leading and trailing edges. The geometry about these regions is very important. Thin airfoils are typically specified by coordinates leading from the TE to the LE (or vice versa). Thickness is distributed by offsetting the original coordinates by a finite value. Thin composite airfoils are usually created by draping a fabric over a mold, so the thickness is plotted perpendicular to the camber line. This results in a straight LE/TE with one panel. Nominally, there should be multiple ($>> 1$) panels to describe this area. Convergence ability of the solution suffers because of the non-smooth shape of the LE. This necessitates a modification, and a new "false" round LE is generated only to enable this analysis. This will not affect the lift and drag coefficients at any significant level, but will improve convergence tremendously [29]. Pelletier and Mueller [30] confirmed the lack of influence of LE and TE shapes experimentally. Similarly, the TE is given a "false" wedge shape to aid in the application of the Kutta condition.

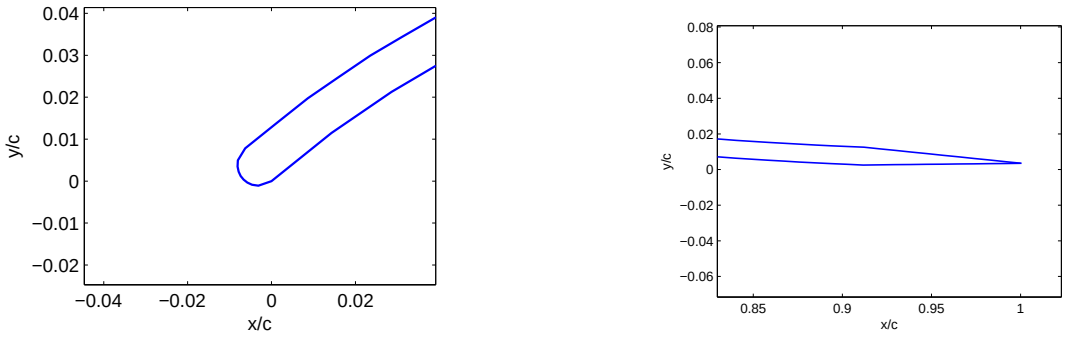

Figure 6.2: Refined leading edge (left) and trailing edge (right) geometries for importing coordinates into XFOIL.

The number of panels generated by the airfoil coordinates alone is sufficient for a solution; however, more panels are added to smooth results. The number of panels is generally around

150 panels (XFOILs imposes a limit of 177). A plot of the final airfoil coordinates is given in Figure 6.3.

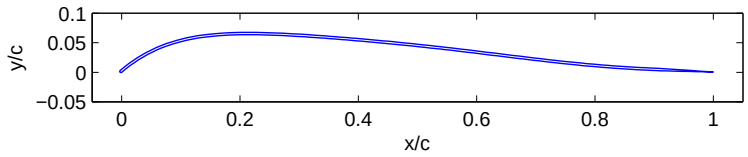

Figure 6.3: Conditioned GenMAV airfoil coordinates for importing into XFOIL.

6.3 C_p Distributions

Dimensionless C_p distribution is calculated and plotted with XFOIL for a 0° angle of attack and three Reynolds numbers between $7.6(10^4)$ to $1.4(10^5)$. Test section turbulence is accounted for with the transition criterion n_{crit}, which is kept at the default value for wind tunnels with an average level of turbulence [28]. A visualization of the associated vectors are simliarly shown in Figure 6.4.

The net upward pressure causes lift. Negative angles of attack progressively reduce this lift and extend the downward suction near the LE on the bottom surface further along the chord. The stagnation point just above the LE is responsible for the sudden jump in C_p. The flow then accelerates and peaks in velocity around the maximum camber point on the top surface, from where the majority of the lift is derived. A suction peak is also present just below the LE; the cause of which is the very small leading edge radius. The suction is a counteracting effect to the rapid change in flow direction around this edge. At sufficient magnitudes, separation can occur due to an adverse pressure gradient. The net aero-structural effect is muted, however, by the inherently thin LE.

Lift varies slightly with Reynolds number. In viscous mode, XFOIL makes predictions between the boundary layer and the flow field via integral boundary layer equations and the e^N method [28]. On this airfoil, it predicts separation and a drop in C_p to occur earlier for increasing Re. This loss of lift occurs on the top surface due to a laminar separation bubble. Laminar separation bubbles are a phenomena of low Reynolds number flow ($10^4 < Re < 10^6$). They are formed when an adverse pressure gradient becomes significant enough to induce rotational flow in the boundary layer [31]. This occurs when the laminar boundary layer

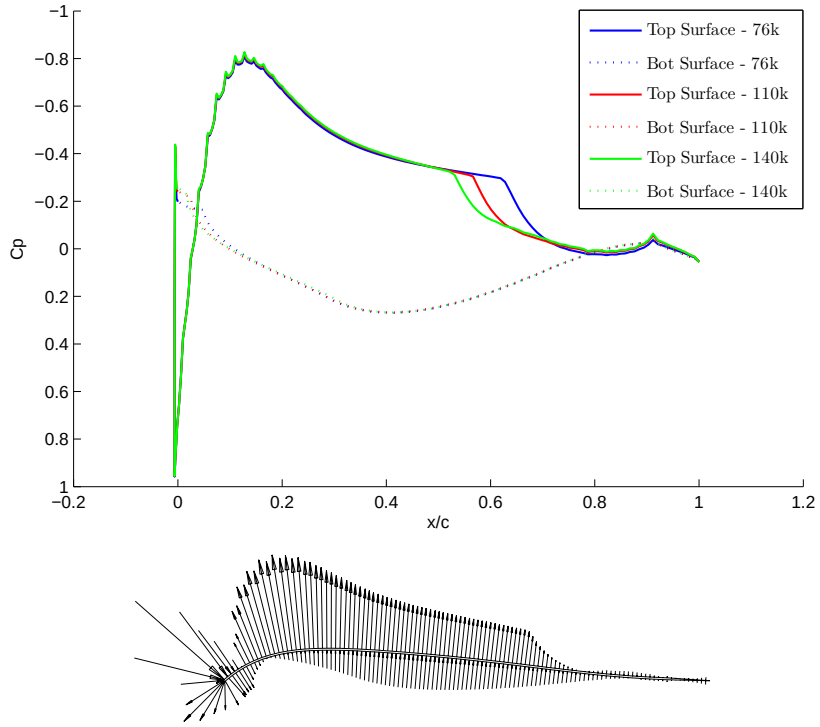

Figure 6.4: Distribution (top) and vector plot (bottom) of the C_p distribution on the Gen-MAV airfoil. Note the ordinate is reversed.

separates and becomes turbulent, but a circulatory pocket of entrained flow forms in the transitional region. Resulting separation explains the characteristic plateau and subsequent drop in C_p developing between x/c=0.55 and x/c=0.65 in Figure 6.4. Likelihood of reattachment decreases for $Re > 5(10^4)$ [31], but the data show marginal reattachment of flow near the TE.

In two dimensional analysis, spanwise effects are assumed negligible. This includes spanwise flow interactions. Laminar separation bubbles and other boundary layer phenomena are expected to hold constant over airfoil span. Realistically, some three dimensional effects such as this are anticipated. Correction factors accounting for a constrained wind tunnel test section are used to increase accuracy of predictions. Flow unsteadiness is assumed to be of low magnitude and frequency; minor perturbations are averaged out by time weighted data collection. The legitimacy of these assumptions will be assessed with a comparison of analytical and experimental results in Chapter 7.

6.4 Refinement of Airfoil Design

It was discovered that aerodynamic loading had a pronounced effect upon the portion of the airfoil between the LE and the quarter chord. In the model, the region covering the LE was designed to incorporate two ply materials. The first corresponds to the ply that covers the entire chord and acts as the actuator substrate. The second is a number of layers of 0/90° woven carbon fiber used to transmit lifting loads to the main vehicle structure (fuselage/frame). This second layer was initially designed to incorporate a single ply of 90° unidirectional carbon fiber. Analysis of aero-structural interactions showed this to be grossly insufficient; large deflections at the LE were predicted. This led to the gradual addition of individual plies to stiffen the LE of the model. In Figure 6.5, the maximum deflection is recorded for various LE thicknesses, which relates to the ply count.

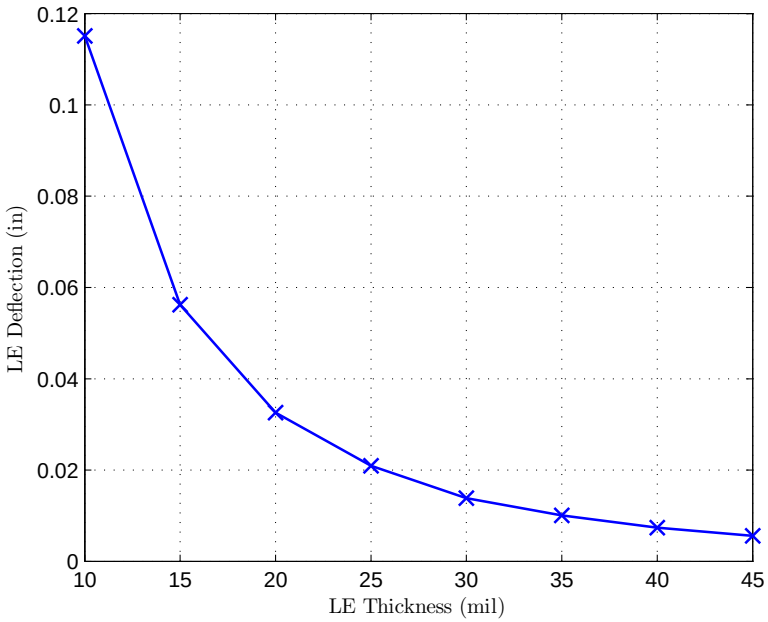

Figure 6.5: Maximum static downward deflection of the LE for various thicknesses. Results are normalized to the greatest value within the plot.

An obvious pattern of diminishing thickness effects are shown. From this figure, a minimum thickness of about 0.04 in (40 mil) is chosen to be acceptable. This corresponds to four woven plies of about 6.6 oz/yd^2 carbon fiber.

6.5 Sectional C_d, C_l Predictions

A 5 in chord and flow speeds of 9, 13, and 17 m/s give a range $4.2(10^4) \leq Re_c \leq 1.7(10^5)$. The following lift polar and other plots are for a 0.8% thick GenMAV airfoil.

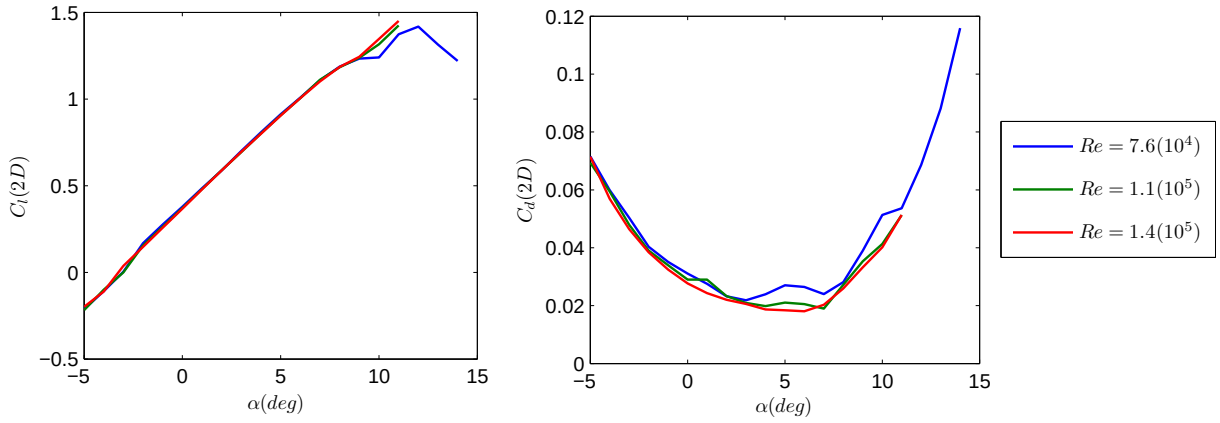

Figure 6.6: Baseline lift polar and drag data for the GenMAV as given by XFOIL.

The standard GenMAV airfoil is predicted to stall around a 10° angle of attack, although convergence at this point was not attained for the higher Re. This failure is most likely due to XFOIL's difficulty in determining larger regions of separated flow [28], therefore, it is assumed that lift would taper or drop off anyway. The zero angle lift coefficient due to airfoil camber is about 0.37, and $C_{l,max}$ ≈1.4-1.45. Minimum drag occurs between 3-6°. Lift does not seem to be a function of Re for the range specified, but drag does show an upward trend with Reynolds number near 5°.

According to the results, L/D_{max} increases from 46 to 59 over the Reynolds number range. These peaks occur between 6-7°. This closely matches the chosen incidence angle of the standard GenMAV MAV [21].

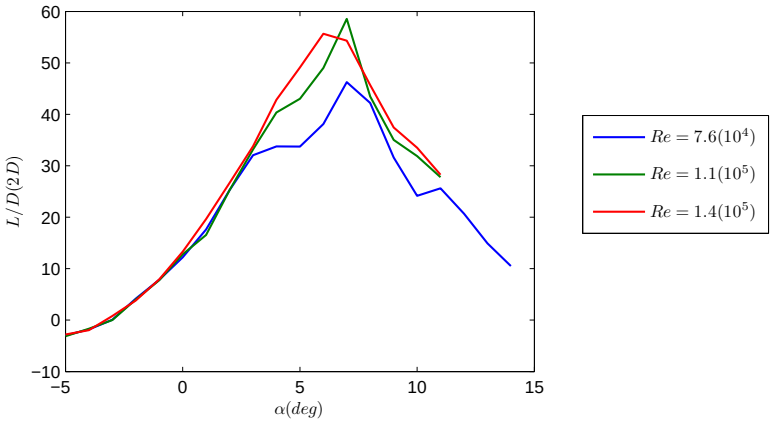

Figure 6.7: Baseline lift/Drag ratio versus angle of attack for the GenMAV airfoil.

6.6 Static Aeroelastic Response

The methodology for predicting static aeroelastic behavior of a morphing airfoil is presented. Pressure distributions over the GenMAV airfoil with a round LE and sharp TE are solved with XFOIL. The airfoil is set at 1% thick due to the real expected thickness of a bimorph actuator and optimized substrate. Non-dimensional pressure coefficients (C_p) are retrieved from XFOIL solutions with the *CPWR* command under the viscous analysis menu *OPER*. As purely a function of velocity ratio[1] for incompressible flows [32], C_p results from the XFOIL solution for a normalized airfoil may be extrapolated to different sized airfoils. Consequently, C_p is scaled to the appropriate chord and then applied over the complete model span. Pressures are calculated from Equation 6.1.

$$C_p \equiv \frac{\Delta p}{\rho U_\infty^2/2} \tag{6.1}$$

A MATLAB mfile post-processes the raw output for proper importation into NX by separating top and bottom pressure distributions into an intermediary data file. For 2D analysis, spanwise pressure variation is assumed uniform and pressures on the infinitesimal leading edge are ignored. Two boundary conditions with equivalent chordwise pressure distributions are placed on the root and tip of the model airfoil. An interpolation routine in NX Nastran delivers a spatial distribution of pressures along the airfoil span. Direction of the load on

[1]Ratio is between the local velocity U_L along the airfoil surface and freestream velocity U_∞

each element is determined by element orientation. Top and bottom pressures are applied to the 2D mesh. The FEA model is solved in the same way as previous simulations. Nodal displacements along the center span are saved into a new file. An assumption is made that the displacements at this location are representative of the entire span. This is true in most cases; only extremely thin substrates exterior to the bimorph location tend to invalidate the assumption.

Another MATLAB mfile receives the nodal displacements and generates proper XFOIL coordinates. The number of panels is correlated to the number of nodes along the chord on the model. Additional datapoints augment the net panel count to around 149. Leading and trailing edge treatments ease solution convergence. The entire process for converging upon a final static displacement prediction is given in Figure 6.8.

The static aeroelastic deflections of the morphing GenMAV airfoil design in low speed flow (9 m/s) is given in Figure 6.9.

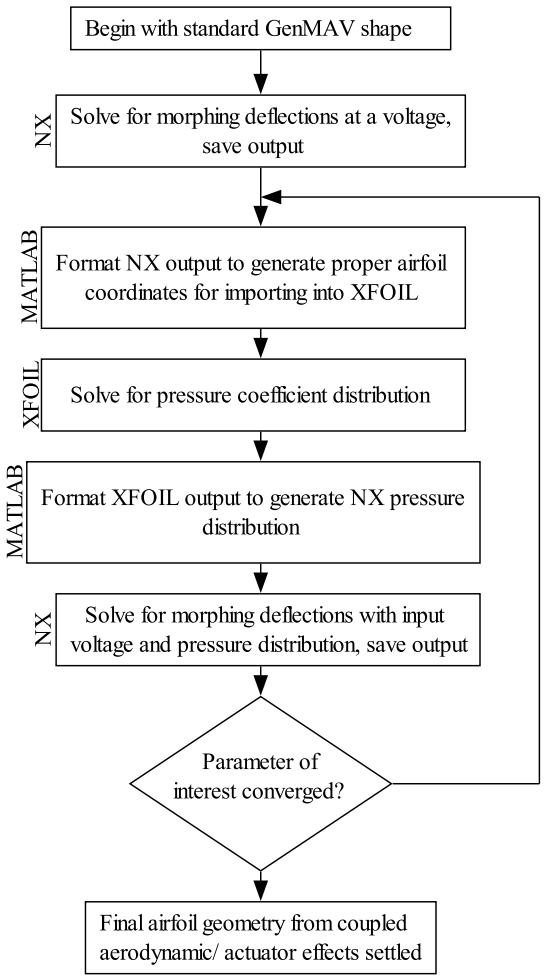

Figure 6.8: Numerical procedure for obtaining convergence of static aeroelastic predictions.

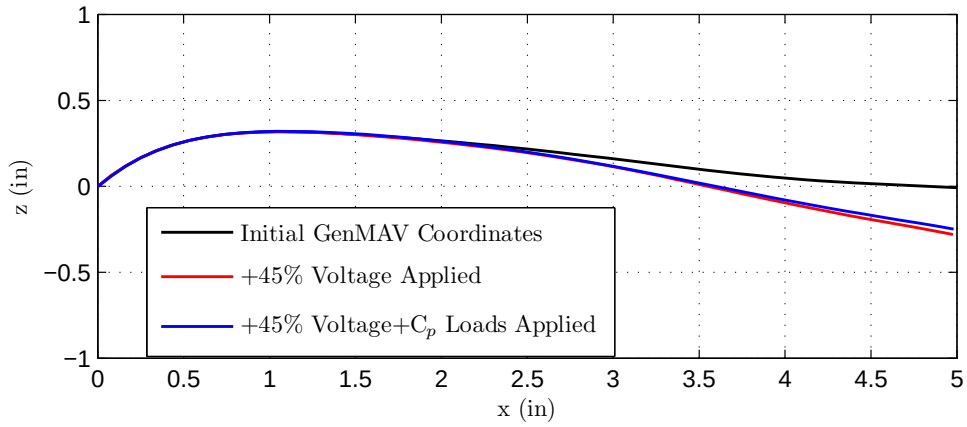

Figure 6.9: The pattern of displacements at 45% input after pressure loading is applied.

Here, the change in relative displacement is shown after just five iterations. Convergence, defined as less than 0.1% change in TE deflection, was achieved with only a few iterations. An iterative process history showing solution convergence is given in Figure 6.10. As a result of the stiffened region between the LE and QC and the chordwise placement of the embedded actuator, the majority of the displacement occurs behind the QC location. This effect is consistent for all simulated flow speeds and actuation input levels.

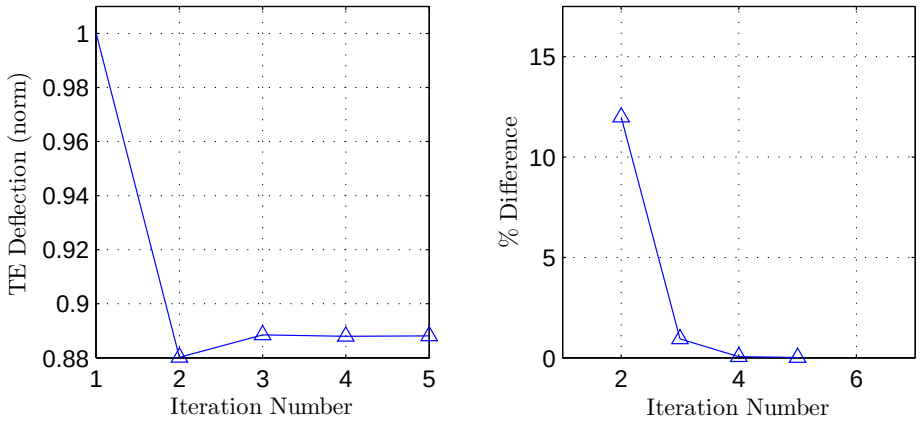

Figure 6.10: Convergence trends of the airfoil deflections at 45% input through the iterations.

The convergence trend of Figure 6.10 is common to all unlisted convergence plots. Looking at the effect of higher aerodynamic loading, a flow of 17 m/s was simulated while the actuation

was set at 90% (Figure 6.11). As expected, the larger pressures from the higher speed cause a greater loss of camber.

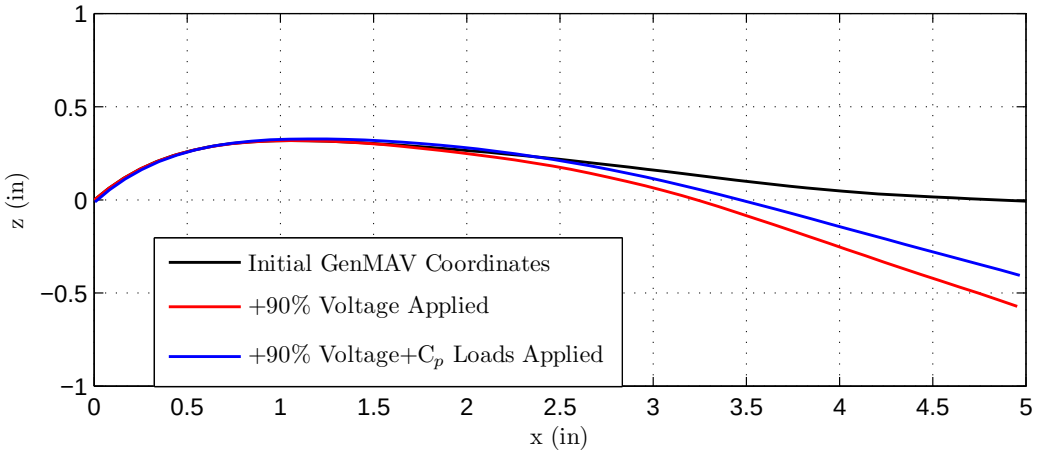

Figure 6.11: The pattern of displacements at 90% input after pressure loading is applied.

Static aeroelasticity assumes an equilibrium has been reached between aerodynamic and elastic forces. Velocities and accelerations are assumed to have settled after solution convergence. Temporal effects on system dynamics can be hidden by this assumption. This is why experiments to validate the model are so critical.

Chapter 7

Wind Tunnel Testing

An overview of the wind tunnel facility with the instrumentation for data collection is discussed. This form of experimentation is the only method available for validating numerical solutions obtained from aerodynamic analyses.

7.1 Wind Tunnel Facility and Instrumentation

Located in the CIMSS laboratory in Durham Hall on the Virginia Tech campus is a custom open return type low speed subsonic wind tunnel built for past and present research on MFC actuated airfoils. More in-depth construction details may be found in [6] and [9]. All aerodynamic experiments listed in this thesis were completed at this facility.

Two fan stages produce airflow that is drawn through honeycomb flow straighteners at the inlet, and then converged into the test section at a ratio of 5.9:1. The rectangular test section is 35.6 x 13.6 cm in cross section and 91 cm in length. It can hold airfoil spans of 133 mm. Test section speeds are variable between 2.5 and 18.5 m/s. Flow speed steadiness is a function of speed and activated fan stages. Tests demonstrating this variation are presented in Appendix E. Overall length is 4.1 m. Two static ports and a FlowKinetics pitot-static tube are connected to Setra and Dwyer differential pressure transducers, respectively. The Setra unit is has a full range of 0-2.5 inH_2O and 0.25% accuracy. The Dwyer transducer has a 0-5 inH_2O full scale range and 1% accuracy. An Omega thermocouple protrudes into the test section to indirectly provide estimations of air density. An optoNCDT laser

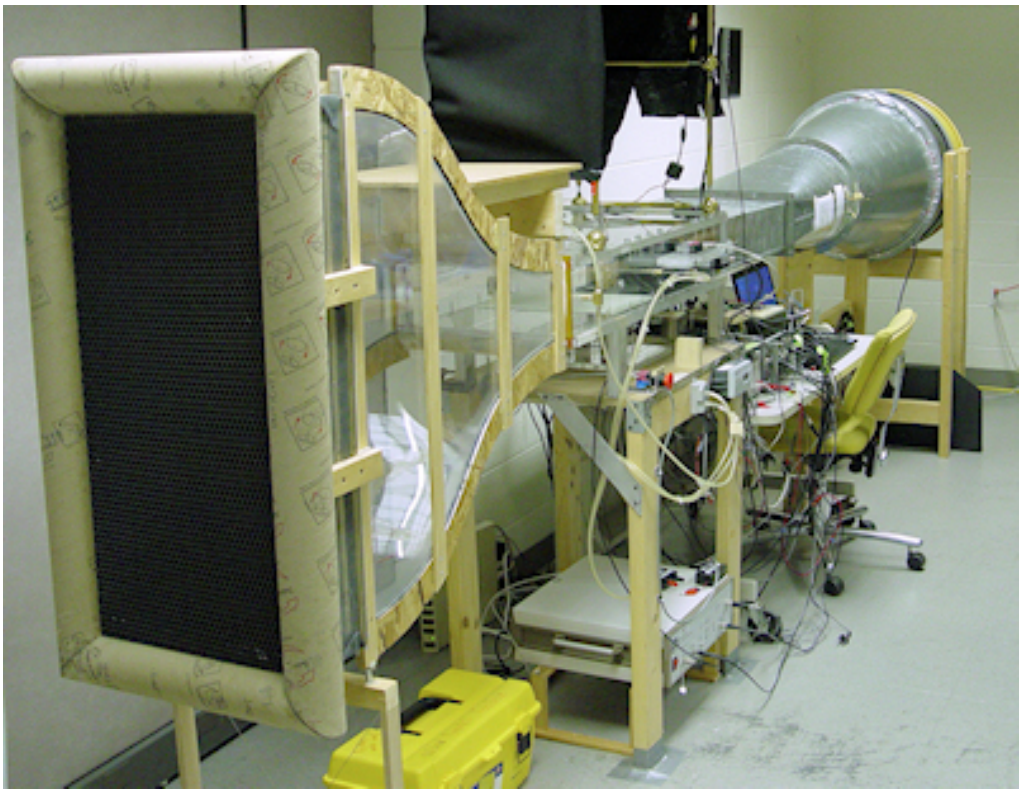

Figure 7.1: The open loop WT setup with the inlet in the foreground.

displacement sensor with 0.01% full scale output accuracy is mounted along the test section wall to gauge deflection distances from MFC actuation. Lift and drag forces are captured by two Transducer Techniques 10 lb capacity load cells. All measurement devices are given a minimum warm-up period of 30 minutes before data collection. Finally, a Canon S5-IS camera is situated above the test section and takes photos of the airfoil cross-section.

The hardware for driving the MFCs includes a Trek High Voltage Amplifier and bipolar asymmetric drive circuit detailed by Bilgen [26]. This amplifier also outputs the drive circuitry voltage and current draw as seen at the load output. An Oriental Motor Vextra stepper motor and Velmex stepping motor controller can reposition the airfoil angle to within 0.1°. A small alignment jig provides the initial airfoil alignment of 0° relative to the wind tunnel wall.

Both pressure transducers were calibrated against a Dwyer inclined differential manometer under various dynamic pressures created by the wind tunnel between 0 and 1.78 inH_2O. This

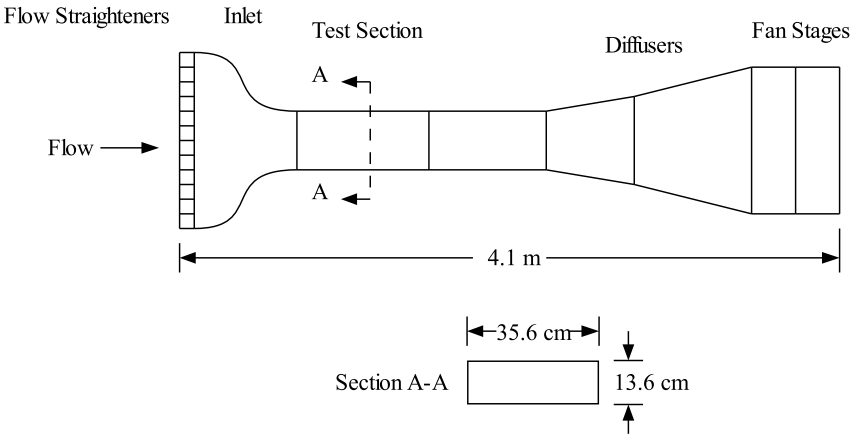

Figure 7.2: Layout of the CIMSS wind tunnel. Figure not to scale.

manometer had a sensitivity of 0.02 inH_2O. The low pressure side of each pressure sensing device was connected to the static pressure tap from the pitot-static tube, and the high pressure side was connected to the stagnation pressure tap. The load cells were calibrated by simulating a force at the middle of the test section, correlating to the center span of the airfoil. This force was created by hanging precision weights from a cable/pulley assembly.

Velocity was deduced from a relationship between static pressure and dynamic pressure. The static pressure was measured at the front of the test chamber. A factor related this to dynamic pressure seen at the airfoil quarter chord location.

Data acquisition was handled by a National Instruments DAQ-Card 6062E and SCC-68 breakout box. All transducer channel voltages were polled by the onboard 12-bit A/D converter at 100 hz over 5-10 seconds. The resulting data was time-averaged to filter noise. This device interfaced with a standard PC running LabVIEW 2009 on top of Windows XP. Hardware accessing each channel is outlined in Table 7.1 [1].

Turbulence rejection is bolstered through use of honeycomb flow straighteners and screens. Flow quality measurements were previous surveyed by Bilgen [6] [9] for an empty test section. Turbulence intensity is a function of flow speed, but does not exceed 0.4% for the indicated range. Freestream velocity varies by 4.5% and 1.5% in the horizontal and vertical directions, respectively, but these deviations are not accounted for in later coefficient corrections.

[1] Servo PWM unused in the scope of this thesis

Table 7.1: All wind tunnel instrumentation hardware.

Ch	Device	Purpose
AO/0	Trek 623B	High Voltage Amplifier
AI/0	Setra 267	Pressure Transducer
AI/1	Omega CCT-22	Air Temperature
AI/2	Trek 623B	MFC Driver Voltage
AI/3	optoNCDT ILD1800-200	Laser Displacement
AI/4	Dwyer 668-5	Pitot-Static Tube Pressure
AI/5	Trans. Tech. MLP10,TMO-2	Lift Load Cell/ Signal Conditioner
AI/6	Trek 623B	MFC Driver Current
AI/7	Trans. Tech. MLP10,MO-1	Drag Load Cell/ Signal Conditioner
D/3	Canon S5IS Camera	Test Section Photos
C/0	Servo Motor PWM	Flap Actuation

7.2 2D Lift & Drag Coefficients

A two-component load balance simutaneously measured lift and drag forces. The balance is external to the test section. The part of the balance that holds the airfoil models is called the "C-Arm". Physical airfoil models with a constant 133 mm span and 127 mm chord are vertically fixed to this C-Arm to cancel the effect of gravity. Aerodynamic loads are carried by the fixture to the load balance and pivot table. These forces pivot the entire assembly about a universal joint at the base, and in doing so apply an amplified force to the lift and drag load cells which are aligned in their respective directions. In this manner, certain configurations such as high angles and flow speeds in the upper range of the wind tunnel can load the cells up to 80% of their capacity. The pivot table can change the angle of attack by rotating the entire balance (C-Arm and counterweight). A 1-2 mm gap exists between the model and test section wall on each side of the airfoil. This is mostly in the range of acceptability as shown by Mueller and Burns [33]. Sectional lift and drag coefficients were calculated in the following manner:

$$C_l = \frac{F_l}{0.5\rho V^2 A} \qquad C_d = \frac{F_d}{0.5\rho V^2 A} \tag{7.1}$$

where F_l and F_d are the time averaged load cell outputs, ρ is the density of air, V is the velocity calculated at the quarter chord, and A is the effective airfoil area. Wind tunnel

blockage and streamline curvature corrections were applied to lift and drag coefficients. These are discussed in Appendix E.

7.3 Model Fabrication and Installation

Using the designs generated in Chapter 3 and construction procedure in Appendix C, the morphing GenMAV airfoil was fabricated in-house. The ply schedule comprising the model surface was laid up in a precision CNC-cut mold and vacuum bagged during the curing process. Special care was taken with respect to MFC alignment during this step in order to stay true to the previously determined layout. Excessive dimensions were trimmed to produce an airfoil with a 127 mm chord and 133 mm span. A span of this length minimizes the gap between the model and tunnel ceiling/ floor. Proper two dimensional flow requires these gaps to be as small as possible.

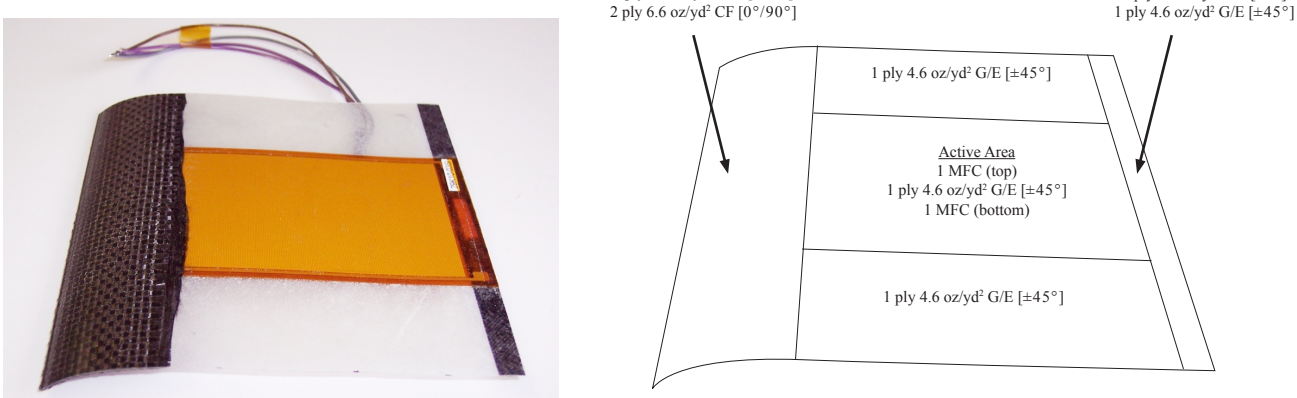

Figure 7.3: The airfoil with embedded M8557-P1 actuator.

Post-cure, the model was removed from the mold. The edges were trimmmed to create a 133 mm span. Finally, 8-32 studs (not shown) were bonded to the thin airfoil at the quarter chord with 3M DP460 epoxy. Extra care was taken to ensure the airfoil matched the design as much as possible. The four requisite electrical connections to the MFC terminals were insulated with Kapton tape to avoid exposure to conductive carbon fibers. Each of the four wires inevitably adds bulk to the airfoil, so these were secured to the bottom surface and covered with more tape to provide the smoothest surface possible.

The model was installed into the C-Arm fixture. Couplers were secured to the studs rigidly

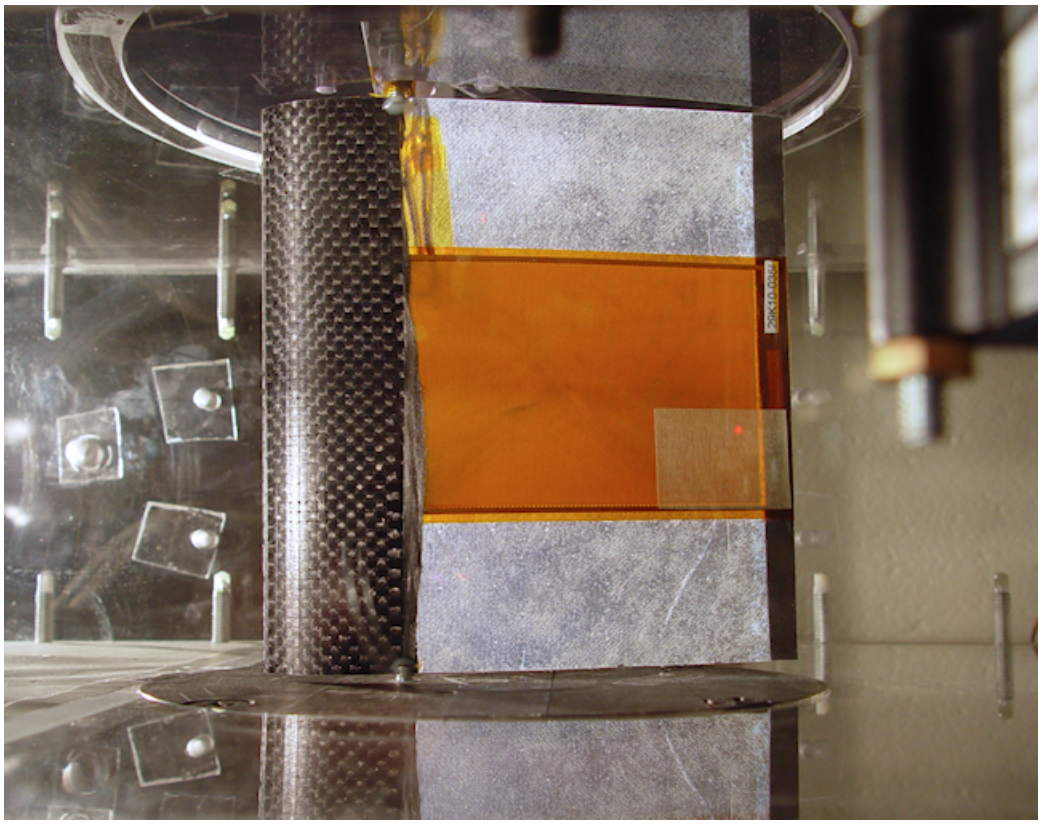

Figure 7.4: Airfoil mounted in the wind tunnel.

fixed at the quarter chord. Final model weight is 31.5 g.

7.4 Reference Airfoil Investigation

For the purpose of validating the experimental wind tunnel setup, a reference NACA airfoil was installed. The NACA 0009 airfoil with a 127 mm chord and 133 mm span was tested under various angles of attack at a speed of 15 m/s and $Re = 1.4(10^5)$. The airfoil was made of rapid prototyping material. Baseline data for low Reynolds number flow was obtained from Selig [34].

The lift predictions match up well. This load cell was calibrated only in the negative lift direction, but this doesn't seem to have any detrimental effect. The results reveal an unexpected asymmetric drag for this airfoil. Minimum drag occurs at 2°. A few explanations

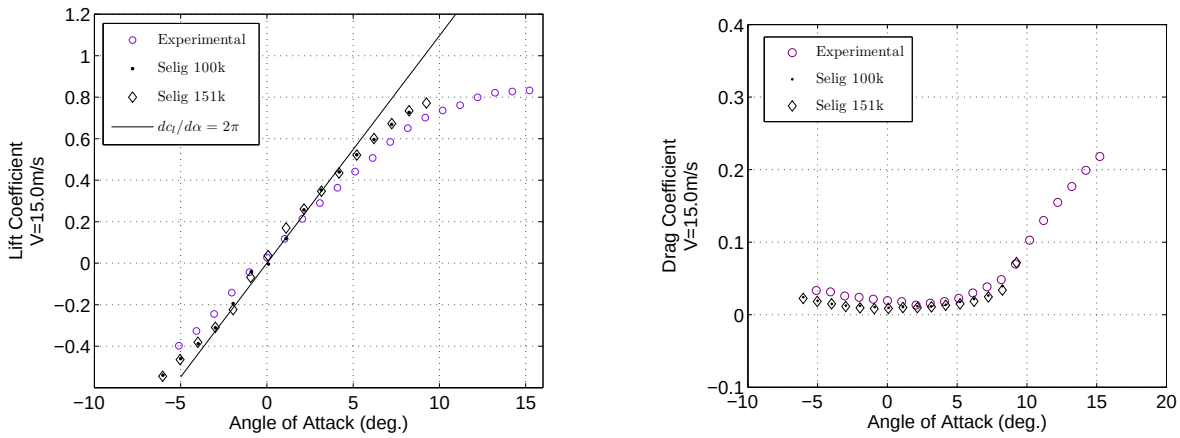

Figure 7.5: Comparison of lift and drag results for the NACA 0009 airfoil.

are provided for the admittedly high drag. During the load cell calibration process, a slight cross-coupling between lift and drag load cell output was uncovered during drag calibrations. Additionally, each measurement is very sensitive to external factors due the low forces involved. The difficulty in ascertaining true drag should not be interpreted as though experimental drag is useless; it still provides data for comparisons.

7.5 Experimental Procedure

A comprehensive LabVIEW Virtual Instrument (VI) was written to gather data from all sensors and equipment shown in Table 7.1. A simple control file specifying flow speeds, angles of attack, and voltage sweeps forms the only program input. Tunnel speed is manually set for each desired Reynolds number. A velocity readout indicates the test section velocity, and the variable autotransformer for fan control is adjusted until the readout settles on the desired velocity. Airfoil angle of attack and MFC voltage sweeps are completely automated. At each voltage (or actuation input), a 6 second delay waits for the airfoil to settle to a new static position, and then 5 seconds of data are recorded at a frequency of 100 Hz. Simutaneously, the camera is triggered to capture a photo of the deflection. Immediately before and after each test, tare data are gathered from the lift and drag load cells for every angle of attack. These data remove the effect of an uncanceled force due to airfoil weight. Lift and drag coefficients ultimately quantify the aerodynamic characteristics of the mounted airfoil.

Although the wind tunnel is capable of flow speeds up to 18.5 m/s, undesirable vibrations

occur due to fan RPM (and possibly blade pass frequencies) at this level. This limit was thus set at 17 m/s. Stall is expected to occur after 10° from XFOIL predictions, so the angle of attack limit is given as 15°. Voltage sweeps are stepped at 22.5% of the full range (+337.5V/-112.5V). Total test time depends on the breadth and desired detail of the test, but generally takes around 3 hours for each airfoil.

7.6 Results

All test results are gathered at once in the wind tunnel. Figure 7.6 gives a general idea about the magnitude of actuator effectiveness of camber control while the test was being completed. The figure shows minimum, neutral, and maximum deflections at $\alpha = 10°$ and $U = 9\ m/s$.

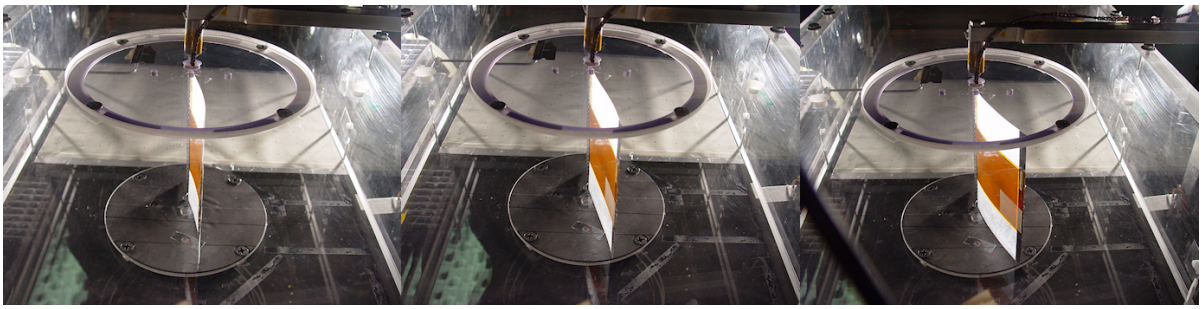

Figure 7.6: Airfoil deflections in the wind tunnel as seen aft of the test section. From left to right, -90%, 0%, and +90% actuation.

7.6.1 Sectional C_d and C_l Results

Lift and drag coefficients at flow speeds of 9, 13, and 17 m/s were obtained experimentally and are shown in Figures 7.7-7.11. Lift coefficients taken for increasing angles of attack and actuations are presented, along with XFOIL predictions at $\alpha = 0°$:

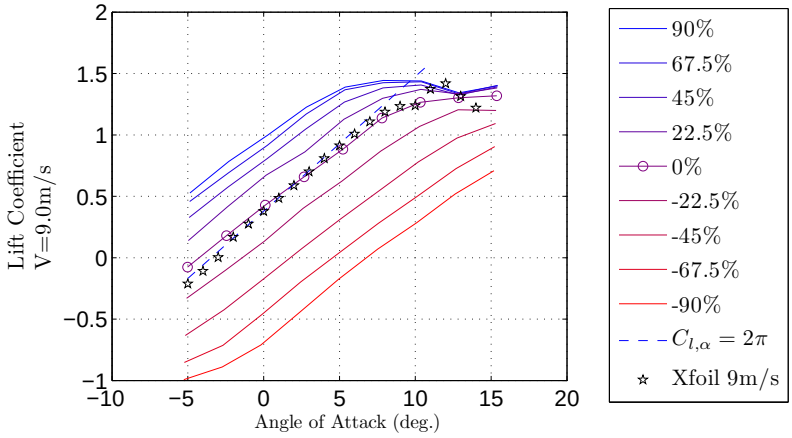

Figure 7.7: Lift versus angle of attack for the morphing GenMAV airfoil at $U = 9m/s$

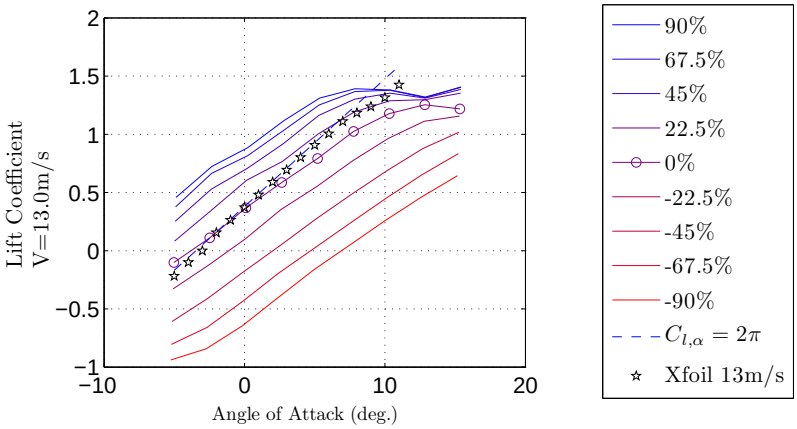

Figure 7.8: Lift versus angle of attack for the morphing GenMAV airfoil at $U = 13m/s$

All lift curves gradually plateau around 7.5°. The slight uptick in lift at the highest angle of attack is not considered useful due to limit cycle oscillations. At 9 m/s, predictions from XFOIL correlate well with the experimental results when the airfoil is in a neutral state.

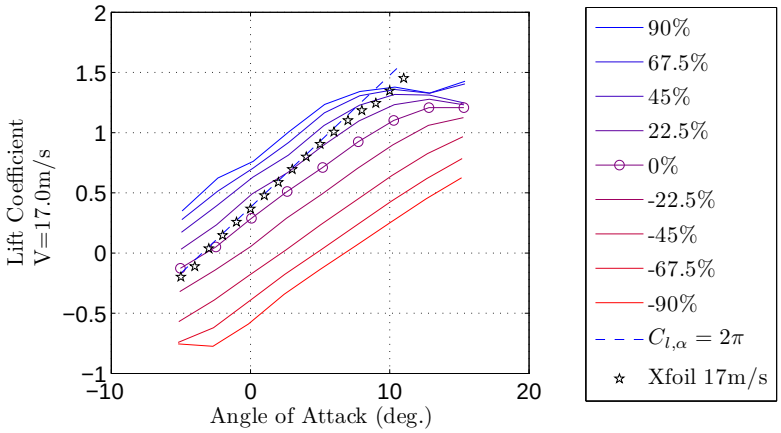

Figure 7.9: Lift versus angle of attack for the morphing GenMAV airfoil at $U = 17m/s$

Lift tapers off starting around 10°, but it does not roll off as expected. Actuator effects are evident in the offset lift slopes corresponding to various actuation levels. Reducing the camber has a tendency to delay stall.

The bulk of the data exhibit linear lift responses with angle of attack. These extend to around $\alpha \approx 7.5 - 10°$, with the exception of large MFC inputs. As flow speeds increase, the neutral input predictions fail to account for a lower lift curve slope. From photographic data taken during testing, it is obvious that this is caused by aeroelastic deformations. The benefit of being able to recover and then exceed the lost lift is afforded by the morphing concept. Although the total authority of the aileron section would drop, it only takes around a 22.5% input to restore the lift loss to the aeroelastic deformation. At 5°, that level of input gives the same amount of lift as the neutral shape at lower dynamic pressures.

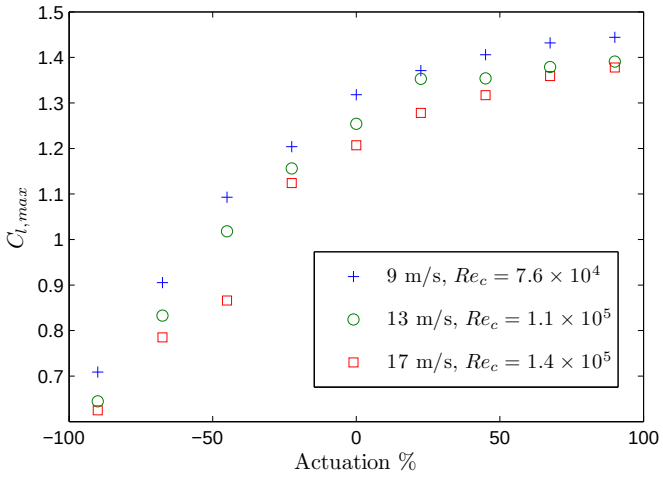

Figure 7.10: $C_{l,max}$ versus actuation for the morphing GenMAV airfoil at $U = 9, 13, 17m/s$

Maximum lift coefficient $C_{l,max}$ peaks at 1.44 for 90% input and 9 m/s. The MFC actuators afford increases of 10%, 11%, and 14% at the three respective flow speeds compared to a neutral camber state. Dynamic pressure has a negative effect on the coefficient. As discussed earlier, this is due to elastic deformations from aerodynamic pressure loading. On average, this reduces $C_{l,max}$ values 4.3% at 13 m/s compared to 9 m/s, and 8.1% at 17 m/s compared to 9 m/s.

Drag coefficients taken for increasing angles of attack and actuations are presented in Figure 7.11.

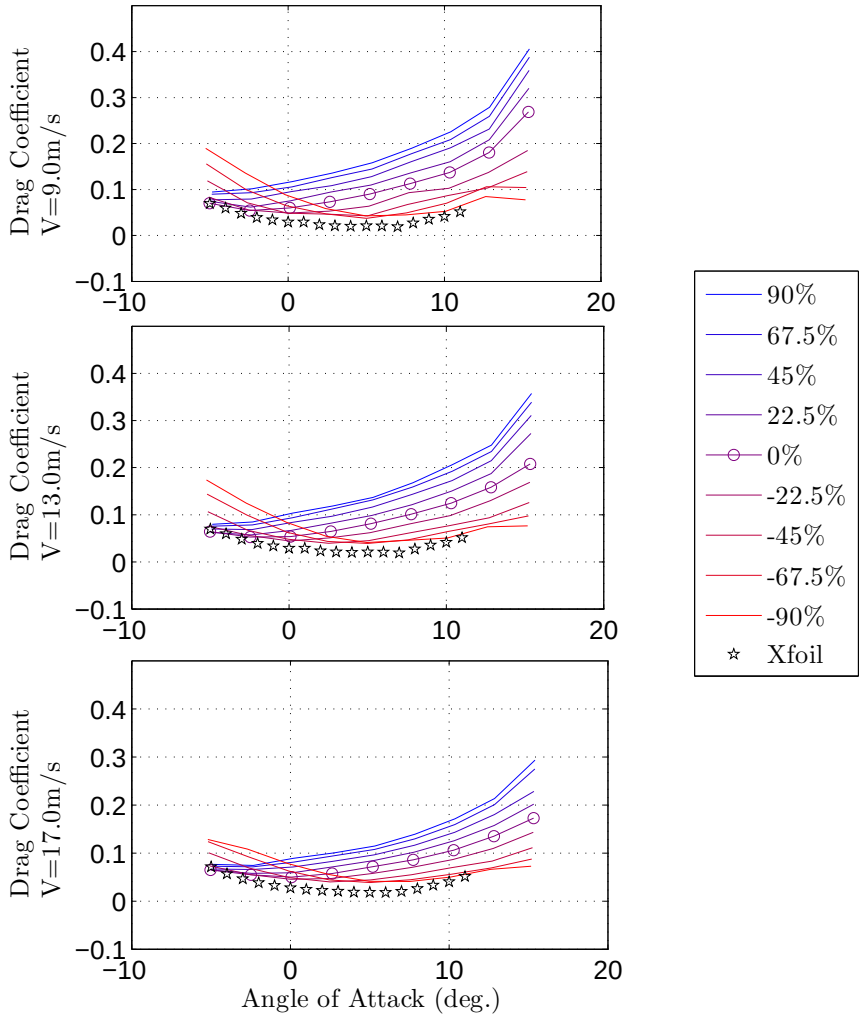

Figure 7.11: Drag versus angle of attack for the morphing GenMAV airfoil at $U = 9, 13, 17m/s$

As expected from the reference airfoil investigation, drag coefficients are higher than predicted. The angle for minimum drag shifts from 0-5° for instances of high camber to less than 0° for the lower camber. Higher flow speeds seem to reduce drag coefficient across all angles and actuation levels. Drag normally rises with flow speed (Equation 7.1). The reduction is another effect of the pressure loading.

7.6.2 Measurement Uncertainty

Uncertainties in sectional coefficients were determined in accordance with AIAA standards [35] on wind tunnel testing. The coefficients arrive from three measurements: drag or lift force, dynamic pressure, and area. Bias (systematic) and precision (random) errors from each of those individual measurements contribute to overall coefficient uncertainty. Force measurement uncertainties are combined from load cell and signal conditioner instrumental errors. Pressure uncertainty is the result of a calibration process and elemental tranducer errors. A small amount of uncertainty is added from measurement of the airfoil planform. A 95% probability level is assumed for combination of elemental uncertainty sources and for calculating component precision errors. Bias uncertainties are calculated by Equation 7.2:

$$B_c = \left(\sum_{i=1}^{J} [\theta_i B_i]^2 \right)^{1/2} \qquad \theta_i = \frac{\partial r}{\partial X_i} \tag{7.2}$$

where i is the index for bias uncertainties B_i and X_i is the measurement variable with associated error sources. This equation omits correlated measurement effects because none are made in the determination of lift/drag coefficients. Precision uncertainties are calculated by Equation 7.3 since some, but not all, of the elemental errors are determined with averaged readings:

$$P_c = \left(\sum_{i=1}^{J} [\theta_i P_i]^2 \right)^{1/2} \qquad P_i = \frac{K S_i}{\sqrt{N_i}} \tag{7.3}$$

where i is the error source index and θ_i is defined as before. The precision limit P_i is a function of K [1], measurement standard deviation S_i, and the number of samples (readings) N_i. Equations 7.2 and 7.3 account for the propagation of bias and precision limits. Cumulative uncertainty in coefficient calculations is determined from Equation 7.4:

$$U_c = \sqrt{B_c^2 + P_c^2} \tag{7.4}$$

The constant bias errors are listed in Table 7.2.

[1] K is the coverage factor equalling 2 for a 95% confidence interval [35].

Table 7.2: Bias errors originating from transducers used in determining coefficients.

Bias Value B_i	**Measurement** X_i	**Description of Error Source**
$B_F = 0.068\ N$	Lift or Drag Force	Sensor-Transducer Stage, Signal Conditioning
$B_Q = 3.32\ Pa$	Dynamic Pressure	Sensor-Transducer Stage, Calibration
$B_A = 46\ mm^2$	Planform Area	Instrument Resolution

Bias for lift and drag forces are equal because the same load cell type is used for both measurements. Lift and drag coefficient uncertainties were calculated for the range of wind tunnel conditions such as flow speed, angle of attack, and actuation input to the airfoil. Both coefficient uncertainties were mostly a function of flow speed and voltage input. Precision errors were significantly lower in magnitude than bias errors (just 3.6% in comparison, on average), which were prominent for cases of negative actuation. Trailing edge deflection above the original camber line counteracts the gain in lift due to airfoil camber, resulting in very low forces to be measured by the load cells. This explains the peaks in uncertainty in Figure 7.12.

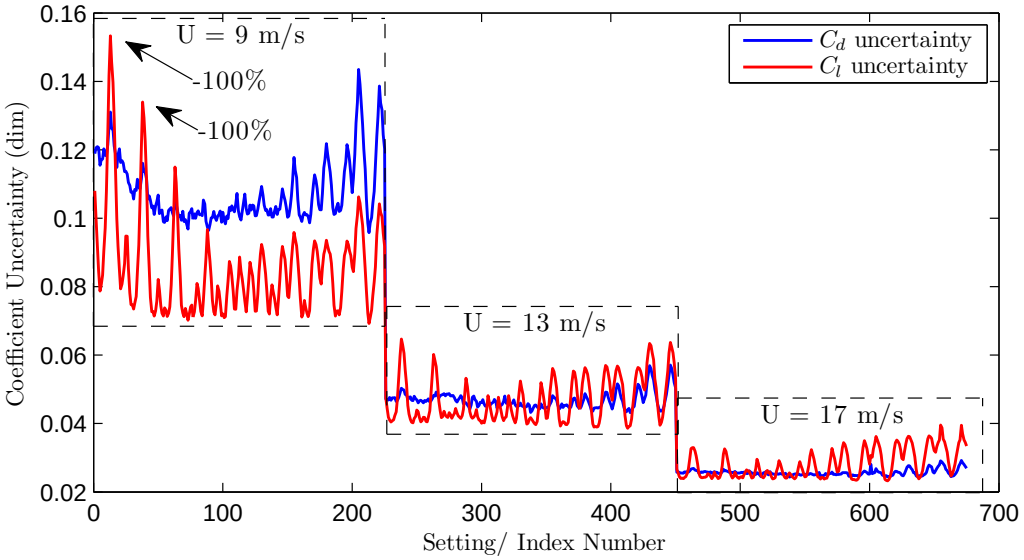

Figure 7.12: Lift/ drag coefficient uncertainty as a function of test setting (setting # correlates to the progression of flow speeds, attack angles, and actuation levels). The three flow speeds and first two peaks corresponding to minimum camber are indicated for clarity.

Table 7.3 charts the variation in maximum and average coefficient uncertainties for lift and drag. Uncertainties peak at the lowest speed, but quickly drop off for higher speeds. The overall average U_{cd} and U_{cl} are 0.061 and 0.054, respectively.

Table 7.3: Average and mean uncertainties for coefficients data.

Speed (m/s)	U_{cd} **mean**	U_{cd} **max**	U_{cl} **mean**	U_{cl} **max**
9.0	0.11	0.14	0.086	0.15
13.0	0.047	0.057	0.047	0.065
17.0	0.026	0.029	0.028	0.040

7.6.3 Model Comparison

A comparison made between wind tunnel data and C_l predictions that included coupled aeroelastic effects is shown in Figure 7.13.

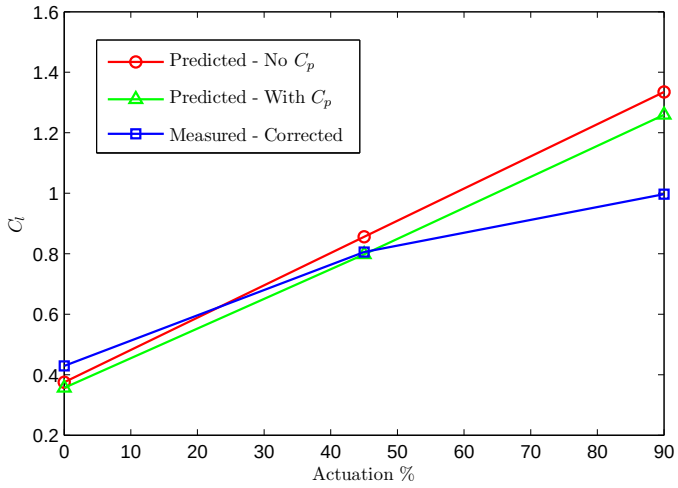

Figure 7.13: C_l predictions versus actuation at $U = 9m/s$ and $\alpha = 0°$.

The pressure loading had a greater effect on the lift characteristics than anticipated, especially at higher actuator input. As the actuation and camber increases, the actual lift deviates from estimations more quickly. Aeroelastic predictions have an initial offset from measured coefficients within uncertainty bounds, but with larger actuation, the predictions account for a only portion of the reduced lift. The disparity could be attributed to separation regions that were larger than predictions. Experimental data were gathered from a test that is 3D in nature; results are only post-processed into averaged 2D measurements after the test is completed. This can obscure 3D effects, such as the complex trend of a laminar separation bubble over the airfoil model span. Simliarly, gaps between the wind tunnel walls at the airfoil root and tip were slightly larger than the recommended amount of 0.5% of span. Due to manufacturing tolerances and the small airfoils of this class of air vehicles, the gaps varied between 1-2% of the span. This could have introduced a larger than expected vertical variation in flow speed within the tunnel. At the minimum, the nonlinearity should be investigated in the future.

7.6.4 Limit Cycle Oscillations

Limit Cycle Oscillations (LCO) are a phenomenon characterized by sustained flow induced vibrations. The mechanism by which this initiates is a coupled aero-structural problem. If strong enough, aerodynamic pressures may induce an elastic deformation of a wing; the deflection then changes the flow around the wing. In a situation where the wing deflects past its neutral shape, the flow and elastic restoring forces change directions. The system may devolve to constant vibration via positive feedback of the coupled motion. Traditional models accounting for this effect describe the motions in a two degree of freedom model. Coupling between the wing pitch and plunge displacements may lead to a net-positive amount of work which may channel energy from the freestream into the the wing structure [36]. Oscillation amplitudes may increase until structural failure. However, nonlinearities in the material stiffnesses can limit excessive growth and instead allow for sustained oscillations (LCO). Minimization of LCO is key in efforts to reduce fatigue and potential resulting damage on wing structures. Nominally, aero-structures must be sufficiently stiff to prevent undue vibrations.

Modeling LCOs with a composite airfoil design is exceedingly complex. A variety of ply schedules create a spatial distribution of local orthotropic properties. Airfoil geometry and strain is not constant and flucuates with MFC input. As such, wind tunnel testing is key in identifying aeroelastic behavior of the airfoil design.

Airfoil oscillations were experienced under high aerodynamic loading. At high angles of attack for the two higher flow speeds, the airfoil vibrates due insufficient chordwise stiffness. Oscillations were measured with the optoNCDT laser displacement sensor already used to gauge trailing edge deflections due to MFC input. In order to quantify the LCO effects, amplitude and frequency measurements were included in post-processing. The NI DAQ is set to queue analog input channels at 1000 hz[1]. Along with a 5 second collection period, a spectral resolution of 0.2 hz is obtained. Input data is filtered with a 5^{th} order Butterworth filter with a cutoff frequency of 40 hz. Using MATLAB, one FFT is performed at each actuation level, angle of attack, and flow speed. Peak frequencies were plotted versus actuation level. Note that the actuation index refers to the level of voltage input as indicated in Table 7.4. The data indicate no clear resonant frequency for $\alpha < 15^{\circ}$ and $U = 9m/s$. However, the FFT plots specific to $\alpha = 15^{\circ}$ at 13 and 17 m/s are given in Figure 7.14.

[1] A sampling frequency greater than 200 Hz is not really necessary, since oscillation frequencies are limited by lower frequency airfoil dynamics.

Table 7.4: The voltages across the top and bottom MFCs embedded in the airfoil as a function of the actuation index number.

Index #	**Act. %**	$\mathbf{V_{MFC}^{top}}$ **(V)**	$\mathbf{V_{MFC}^{bot}}$ **(V)**
0	0.0	0.0	0.0
1	22.5	337.5	-112.5
2	45.0	675.0	-225.0
3	67.5	1012.5	-337.5
4	90.0	1350.0	-450.0
5	67.5	1012.5	-337.5
6	45.0	675.0	-225.0
7	22.5	337.5	-112.5
8	0.0	0.0	0.0
9	-22.5	-112.5	337.5
10	-45.0	-225.0	675.0
11	-67.5	-337.5	1012.5
12	-90.0	-450.0	1350.0
13	-67.5	-337.5	1012.5
14	-45.0	-225.0	675.0
15	-22.5	-112.5	337.5
16	0.0	0.0	0.0
17	22.5	337.5	-112.5
18	45.0	675.0	-225.0
19	67.5	1012.5	-337.5
20	90.0	1350.0	-450.0
21	67.5	1012.5	-337.5
22	45.0	675.0	-225.0
23	22.5	337.5	-112.5
24	0.0	0.0	0.0

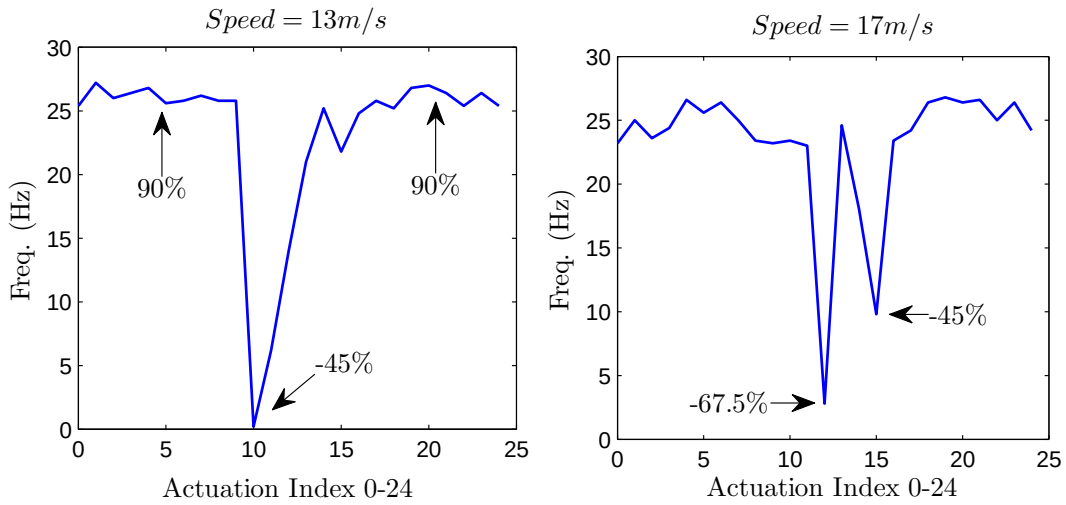

Figure 7.14: Frequency response of trailing edge displacements for indicated flow speeds and $\alpha = 15°$

Figure 7.14 may be interpreted by understanding that a consistently horizontal line represents a constant peak in frequency data across all actuation levels ($-90\% \leq Act. \leq 90\%$) from the FFT. This is precisely what is observed for the speed and angle combinations in the two subfigures. As the dynamic pressure rose, the random responses became more ordered. Most of the data suggest a constant aeroelastic natural frequency centered around 25 hz. The dips in peak frequencies occur around full negative actuation (minmum camber), where no distinctive peak frequency is identifiable. This is most likely due to a cancelling effect of reduced camber (lift detracting) and a high angle of attack (lift enhancing). The associated mean zero data is simliarly plotted to obtain the RMS displacement amplitudes:

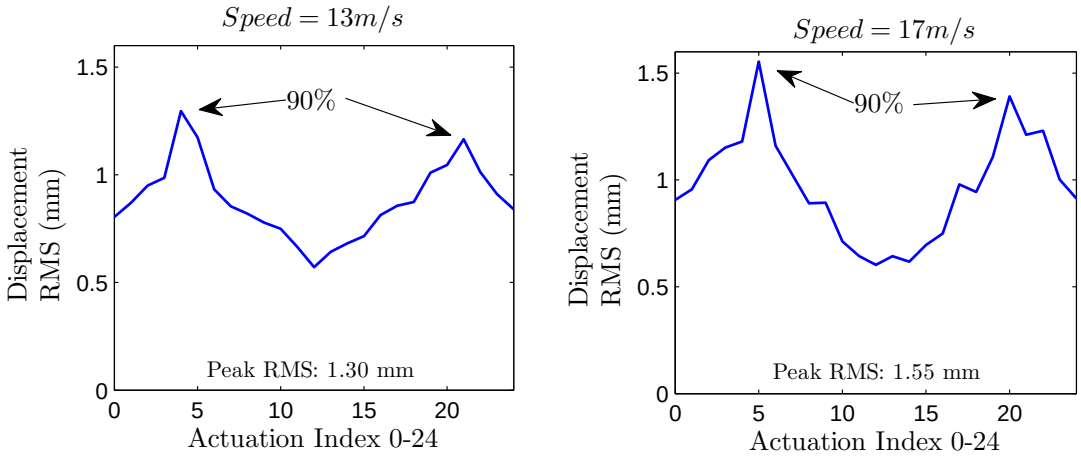

Figure 7.15: RMS amplitude response of trailing edge displacements for indicated flow speeds and $\alpha = 15°$

Average RMS displacement is 0.70 mm across all speeds and angles of attack. As before, amplitudes only spike for $\alpha = 15°$ at 13 and 17 m/s. The peaks are consistent, occuring between 67.5-90% actuation for each of the higher flow speeds. Peaks at these actuations correspond to 204% and 183% gain in RMS amplitudes over the average. Aforementioned average and peak amplitudes correspond to 0.6% and 1.1% of the chord dimension.

LCO behavior did not occur for the expected operating region of $-5° \leq \alpha \leq 10°$. The lift curve trails off beyond 10° for the GenMAV airfoil. Evidence of this has been presented analytically (Chapter 6) and experimentally. This analysis has shown that LCO only becomes in issue at extreme levels of aerodynamic loading exterior to a typical flight regime. Additionally, the boundary conditions defined here do not necessarily reflect the final form. The two fixed points at either end of the quarter cord on the airfoil only serve to allow for the 2D measurements. The LCO observed here are not inexorably linked to the morphing GenMAV airfoil.

Chapter 8

Conclusion

8.1 Summary

Seeking to utilize a promising new actuator that affords an efficient means of shape control, an investigation was undertaken that applied morphing capability to an airfoil. A two dimensional analysis of the GenMAV airfoil design judged the morphing effects over the baseline shape. The orthotropic elastic properties of a composite substrate were optimized for maximum shape control authority, leading to a highly tailored ply schedule. A thermal analogy was used to represent piezoelectric strain. The applicability of using FEA to predict large structural displacements was assessed. Deflection tests initially demonstrated good agreement with the model, matching beam curvature predictions to within 3.7%. However, significant out of plane bending was thought to have caused minor delaminations in the zero-substrate test bimorph.

Minute treatments to the airfoil coordinates' leading and trailing edges were required to enable viscous analysis with the XFOIL program. The Reynolds number was shown to have little influence on sectional lift and drag characteristics of the GenMAV airfoil. A $C_{l,max}$ of 1.45 at 10° and $C_{d,0}$ of 0.02 at 5° were estimated. Subjecting the airfoil to various dynamic pressures was simulated with both XFOIL and NX NASTRAN software. The coupling between pressure loading and elastic deformations was iteratively calculated. The dominant parameter affecting camber changes was found to be airfoil thickness. Substrate material effects were inappreciable, and the selection was driven by the insulating electrical properties of E-Glass. Morphing implications on static aeroelasticity were predicted.

The extensive set of equipment used to obtain lift and drag coefficients in wind tunnel testing was discussed. A brief explanation on fabrication procedures of the morphing GenMAV airfoil was provided. To validate the wind tunnel apparatus, the lift and drag characteristics of a reference NACA 0009 airfoil were assessed. Lift data showed excellent correlation to data provided by previous researchers, although drag was more pronounced. Sectional lift and drag for the GenMAV airfoil matched up well with XFOIL estimations at lower dynamic pressures. At 9 m/s and 0°, a C_l of 0.4 and $C_{l,max}$ of 1.0 were found. Similarly important, a ΔC_l range of +0.6/-1.1 at this angle indicates the large working lift domain due to the piezoelectric effect. With the ability to change the camber, the absolute $C_{l,max}$ is attainable at lower attack angles. Aeroelastic results showed a nonlinear trend of C_l that was underpredicted under higher actuations. Experiments also exposed some LCO effects for limited situations, but the two fixed point wind tunnel model doesn't completely reflect real world boundary conditions.

Lastly, a lightweight circuit prototype was developed to prove that the electrical demands of the actuator did not require any hardware unusually large for an MAV platform. A 32.5 g proof of concept circuit board was fabricated and verified. A second revision condensed the hardware to an estimated weight of 23 g. The final weight is within acceptable MAV payload limits.

The cumulative contribution of this work was the application of morphing wing technology to a standard MAV. Airfoil dimensions accomodated the application of MFCs very well; most practically due to the thin nature of wings in this vehicle class. The GenMAV in particular provides a good base of comparisons, since data from aerodynamic modeling and wind tunnel testing are already freely available [21].

8.2 Recommendations of Future Work

In this thesis, practical airfoil designs were created for a single bimorph comprised of one MFC type. That actuator is the M8557-P1 product from Smart-Material Corporation. This company offers more MFCs that have scaled down in-plane dimensions, but are based on the same piezoelectric principle. Such actuators may be advantageous to vehicle design with reduced weight. Further analysis of morphing airfoils with various distributions of smaller MFCs will determine if these versions are just as effective. These will be characterized by continued wind tunnel testing at the same facility.

A good portion of research remains on identifing the bandwidth characteristics of embedded bimorphs on the thin airfoil. The effectiveness of the thermal analog to predict dynamic response was not quanitifed. The question of how to simulate the response under steady and unsteady aerodynamic loading is also left open (dynamic aeroelasticity).

This thesis was limited to two dimensional analyses and experiments. Only chordwise effects of bimorph placement were studied. There are a myriad of ways to implement wing morphing with MFC bimorphs; this is the benefit afforded to an embeddable actuator. The purpose of the airfoil research is a lead-up to a complete wing and vehicle design. Air vehicle design evaluations will require a larger wind tunnel so that three dimensional effects may be measured.

Continued efforts in aeroelastic tailoring can eliminate the limit cycle oscillations existing at higher aerodynamic loading. It may be prove favorable to trade deformability for a larger safety factor against LCO.

Bibliography

[1] Wilkie, W. K., Bryant, R. G., High, J. W., Fox, R. L., Ileilbaum, R. F., Jr., A. J., Little., B. D., and Mirick, P. H., "Low-Cost Piezocomposite Actuator for Structural Control Applications," NASA Langley Research Center, Newport Beach, CA, March 2000.

[2] Kurdila, A., "Active Materials and Smart Structures," ME5804 Lecture, Virginia Polytechnic Institute and State University.

[3] Smart Material Corporation, May 2011, http://www.smart-material.com/MFC-product-main.html.

[4] Williams, R. B., *Nonlinear Mechanical and Actuation Characterization of Piezoceramic Fiber Composites*, Ph.D. thesis, Virginia Polytechnic Institute and State University, 2004.

[5] Houghton, E. and Carpenter, P., *Aerodynamics for Engineering Students*, Butterworth-Heinemann, 5th ed., 2003, p. 182.

[6] Bilgen, O., *Aerodynamic and Electromechanical Design, Modeling, and Implementation of Piezocomposite Airfoils*, Ph.D. thesis, Virginia Polytechnic Institute and State University, 2010.

[7] Schultz, M. R., *Use of Piezoelectric Actuators To Effect Snap-Through Behavior Of Unsymmetric Composite Laminates*, Ph.D. thesis, Virginia Polytechnic Institute and State University, 2003.

[8] Vos, R., Breuker, R. D., Barrett, R., and Tiso, P., "Morphing Wing Flight Control Via Postbuckled Precompressed Piezoelectric Actuators," *Journal of Aircraft*, 2007.

[9] Bilgen, O., *Macro Fiber Composite Actuated Unmanned Air Vehicles: Design, Development, and Testing*, Master's thesis, Virginia Polytechnic Institute and State University, 2007.

[10] III, O. J. O., Karni, E. D., Olien, C. C., Gustafson, E. A., Kochersberger, K. B., Gelhausen, P. A., and Brown, B. L., "Piezoelectric composite morphing control surfaces for unmanned aerial vehicles," Vol. 7981, SPIE, 2011.

[11] Gandhi, F. and Anusonti-Inthra, P., "Skin design studies for variable camber morphing airfoils," *Smart Materials and Structures*, Vol. 17, 2008.

[12] Kudva, J., "Overview of the DARPA Smart Wing Project," *Journal of Intelligent Material Systems and Structures*, Vol. 15, 2004, pp. 261–267.

[13] Pendleton, E., Flick, P., Paul, D., Voracek, D., Reichenbach, E., and Griffin, K., "The X-53, A Summary of the Active Aeroelastic Wing Flight Research Proram," AIAA/ASME/ASCE/AHS/ASC Structures, Structural Dynamics, and Materials Conference, April 2007.

[14] Bowman, J., Sanders, B., Cannon, B., Kudva, J., Joshi, S., and Weisshaar, T., "Development of Next-Generation Morphing Aircraft Structures," AIAA/ASME/ASCE/AHS/ASC Structures, Structural Dynamics, and Materials Conference, April 2007.

[15] Flanagan, J. S., Strutzenberg, R. C., Myers, R. B., and Rodrian, J. E., "Development and Flight Testing of a Morphing Aircraft, the NextGen MFX-1," AIAA/ASME/ASCE/AHS/ASC Structures, Structural Dynamics, and Materials Conference, April 2007.

[16] Hwang, W.-S. and Park, H., "Finite Element Modeling of Piezoelectric Sensors and Actuators," *Journal of Intelligent Material Systems and Structures*, Vol. 31, No. 5, May 1993, pp. 930–937.

[17] Côté, F., Masson, P., Mrad, N., and Cotoni, V., "Dynamic and static modelling of piezoelectric composite structures using a thermal analogy with MSC/NASTRAN," *Composite Structures*, Vol. 65, No. 3-4, 2004, pp. 471–484.

[18] Reaves, M. C. and Horta, L. G., "Test Cases For Modeling And Validation Of Structures With Piezoelectric Actuators," 42nd AIAA/ASME/ASCE/AHS/ASC Structure and Structural Dynamics Conference, April 2001.

[19] NX7, S. P., "Siemens PLM, Plano, TX," 2010.

[20] Siemens PLM Software Inc., *NX Nastran 7 Element Library Reference*, 2009.

[21] Stewart, K., Wagener, J., Abate, G., and Salichon, M., "Design of the Air Force Research Laboratory Micro Aerial Vehicle Research Configuration," *Proceedings of AIAA*, 2007.

[22] Baker, A., Dutton, S., and Kelly, D., *Composite Materials for Aircraft Structures*, American Institute of Aeronautics and Astronautics, 2004, pp. 57,119.

[23] Hexcel Corporation, *Technical Fabrics Handbook*, 2010.

[24] West System, *Typical Physical Properties*.

[25] Leo, D. J., *Engineering Analysis of Smart Material Systems*, Wiley, 2007.

[26] Bilgen, O., Kochersbeger, K. B., Inman, D. J., and III, O. J. O., "Lightweight High Voltage Electronic Circuits for Piezoelectric Composite Actuators," *Journal of Intelligent Material Systems and Structures*, Vol. 0, 2010.

[27] Kollar, L. P. and Springer, G. S., *Mechanics of Composite Structures*, Cambridge University Press, 2003.

[28] Drela, M., "XFOIL 6.9 User Primer (User Documentaion)," .

[29] Reid, M. R., *Thin/Cambered/Reflexed Airfoil Development for Micro-Air Vehicles at Reynolds Numbers of 60,000 to 150,000*, Master's thesis, Rochester Institute of Technology, 2006.

[30] Pelletier, A. and Mueller, T. J., "Low Reynolds Number Aerodynamics of Low-Aspect-Ratio, Thin/Flat/Cambered-Plate Wings," *Journal of Aircraft*, Vol. 37, 2000, pp. 825–832.

[31] Gad-El-Hak, M., *Flow Control: Active, Passive, and Reactive Flow Management*, Cambridge University Press, 1st ed., 2000, pp. 192–193.

[32] Shevell, R. S., *Fundamentals of Flight*, Prentice Hall, 2nd ed., 1989.

[33] Mueller, T. and Burns, T., "Experimental Studies of the Eppler 61 Airfoil at Low Reynolds Numbers," AIAA, 1982.

[34] Selig, M. S., Donovan, J. F., and Fraser, D. B., *Airfoils at Low Speeds*, H. A. Stokely, 1989.

[35] American Institute of Astronautics and Aeronautics, *Assessment of Experimental Uncertainty with Application to Wind Tunnel Testing*, 1999.

[36] Mazet, R., *Manual On Aeroelasticity*, Vol. 1, North Atlantic Treaty Organization Advisory Group for Aerospace Research and Development, 1968, pp. 1–51.

[37] Barbero, E. J., *Finite Element Analysis of Composite Materials*, CRC Press, 2007.

[38] Barbero, E. J., *Introduction to Composite Materials Design*, CRC Press, 1998.

[39] Barlow, J. B., Rae, W. H., and Pope, A., *Low-Speed Wind Tunnel Testing*, John Wiley & Sons, 3rd ed., 1999.

Appendix A

Generating Laminate Stiffness Properties

Substrate effects are the critical driven requirement to actuator design. The substrate itself may be thought of as a passive component of the MFC actuator in unimorph or bimorph configurations. Before a study of all possible effects may be completed, the material properties of laminate substrates are derived with classical laminate theory.

A procedural summary for calculating equivalent orthotropic properties of a composite substrate used in finite element modeling is hereby given. The three levels at which mechanical properties may be computed include micromechanics, ply (lamina), and laminate. Low level micromechanics combine constituent fiber/matrix properties to find equivalent homogeneous anisotropic properties. Ply mechanics then treat the ply as an orthotropic material in-plane stress, and relate these layer properties to those of the entire laminate factoring in fiber orientations. At the macro-scale, plies with their thicknesses and stacking sequences are combined to find whole laminate properties. This simplification treats a laminate as a singular homogenous material, but also hides potentially important information about stress variations at the ply and micromechanical levels. An assumption is made that any forces within the scope of this work will not stress the substrate beyond failure limits. Additionally, the airfoil model that is devoid of joints or other geometric features is inherently simple; the lack of detail is therefore not a concern. When defining these axes, the label set (1, 2, 3) is reserved for the ply level. The reference coordinate system at the macroscopic laminate level is given the direction labels (x, y, z).

The basis of all laminates studied here are woven fabrics. For purposes of simplified analysis, these are considered to be two sublayers of unidirectional fabric oriented at 90° relative to each other. The apparent properties of the entire fabric are proportional to the percentage of fibers in the warp and fill (weft) directions. Since the yarns on average lie on the middle surface, the these woven fabrics are considered to be balanced. Models that account for weave patterns and geometry can be found in [37].

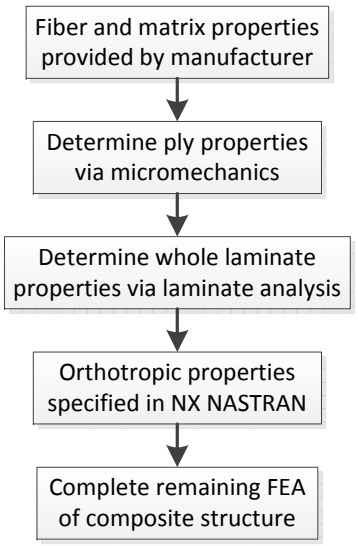

Figure A.1: Steps taken to generate mechanical properties of composite substrates.

A.1 Micromechanics

Although irrelevant to this research, much literature is available that discusses the numerous models for combining constituent fiber and matrix properties into those of a laminate ply. Fiber (E-glass) and matrix (epoxy) data are given by the manufacturers technical datasheets [Hexcel, West Systems]. A set of Rule of Mixture (ROM), Inverse Rule of Mixtures (IROM), and Cylindrical Assemblage (CAM) models are used to calculate orthotropic properties based on the assumption of isotropic fiber/matrix materials.

A.2 Ply Mechanics

Hooke's Law governing the elasticity of an anisotropic material is given by:

$$\sigma_{ij} = C_{ijkl}\epsilon_{kl} \tag{A.1}$$

The stiffness matrix C is a fourth order tensor with 81 components (21 independent). By taking advantage of the three planes of symmetry inherent to woven and unidirectional plies, this can be reduced to:

$$\begin{Bmatrix} \sigma_1 \\ \sigma_2 \\ \sigma_3 \\ \sigma_4 \\ \sigma_5 \\ \sigma_6 \end{Bmatrix} = \begin{bmatrix} C_{11} & C_{11} & C_{11} & 0 & 0 & 0 \\ C_{12} & C_{22} & C_{23} & 0 & 0 & 0 \\ C_{13} & C_{23} & C_{33} & 0 & 0 & 0 \\ 0 & 0 & 0 & C_{44} & 0 & 0 \\ 0 & 0 & 0 & 0 & C_{55} & 0 \\ 0 & 0 & 0 & 0 & 0 & C_{66} \end{bmatrix} \begin{Bmatrix} \epsilon_1 \\ \epsilon_2 \\ \epsilon_3 \\ \gamma_4 \\ \gamma_5 \\ \gamma_6 \end{Bmatrix} \tag{A.2}$$

These are known as the consitutive equations for an orthotropic material (contracted index notation used for the stiffness matrix). As substrates are invariably thin structures, they are considered to be in the state of plane stress. For in-plane properties, the reduced stiffness matrix becomes:

$$\{\sigma\} = [Q]\{\epsilon\} \tag{A.3}$$

$$\begin{Bmatrix} \sigma_1 \\ \sigma_2 \\ \tau_6 \end{Bmatrix} = \begin{bmatrix} Q_{11} & Q_{12} & 0 \\ Q_{12} & Q_{22} & 0 \\ 0 & 0 & Q_{66} \end{bmatrix} \begin{Bmatrix} \epsilon_1 \\ \epsilon_2 \\ \gamma_6 \end{Bmatrix} \tag{A.4}$$

And for the out-of-plane properties:

$$\{\tau\} = [Q^*]\{\gamma\} \tag{A.5}$$

$$\begin{Bmatrix} \tau_4 \\ \tau_5 \end{Bmatrix} = \begin{bmatrix} Q^*_{44} & Q^*_{45} \\ Q^*_{45} & Q^*_{55} \end{bmatrix} \begin{Bmatrix} \gamma_4 \\ \gamma_5 \end{Bmatrix} \tag{A.6}$$

Each ply in a laminate may be stacked so that the in-plane fiber orientations are not parallel. If this is the case, a simple stress transformation is necessary to reorient the angled ply stress into the global coordinates.

$$\begin{Bmatrix} \sigma_x \\ \sigma_y \\ \tau_{xy} \end{Bmatrix} = \begin{bmatrix} \cos(\theta)^2 & \sin(\theta)^2 & -2\cos(\theta)\sin(\theta) \\ \sin(\theta)^2 & \cos(\theta)^2 & 2\cos(\theta)\sin(\theta) \\ \cos(\theta)\sin(\theta) & -\cos(\theta)\sin(\theta) & \cos(\theta)^2 - \sin(\theta)^2 \end{bmatrix} \begin{Bmatrix} \sigma_1 \\ \sigma_2 \\ \tau_6 \end{Bmatrix} \tag{A.7}$$

Applying this transformation to the stiffness matrix,

$$\left[\overline{Q}\right] = [T]^{-1}[Q][T]^{-T} \tag{A.8}$$

To more clearly denote the stiffness matrix in global coordinates, the following notation is used:

$$\begin{Bmatrix} \sigma_x \\ \sigma_y \\ \tau_{xy} \end{Bmatrix} = \begin{bmatrix} \overline{Q}_{11} & \overline{Q}_{12} & 0 \\ \overline{Q}_{12} & \overline{Q}_{22} & 0 \\ 0 & 0 & \overline{Q}_{66} \end{bmatrix} \begin{Bmatrix} \epsilon_x \\ \epsilon_y \\ \gamma_{xy} \end{Bmatrix} \tag{A.9}$$

$$\begin{Bmatrix} \tau_{yz} \\ \tau_{xz} \end{Bmatrix} = \begin{bmatrix} \overline{Q}^*_{44} & \overline{Q}^*_{45} \\ \overline{Q}^*_{45} & \overline{Q}^*_{55} \end{bmatrix} \begin{Bmatrix} \gamma_{yz} \\ \gamma_{xz} \end{Bmatrix} \tag{A.10}$$

A.3 Macromechanics

With the ply stiffnesses defined, they are then combined into whole-laminate force-strain relationship. Note these equations are made based on a small rectangular element subjected to in-plane and bending loads. An ABD matrix relates these forces and moments to mid-plane strains and curvatures.

$$\begin{Bmatrix} N_x \\ N_y \\ N_{xy} \\ M_x \\ M_y \\ M_{xy} \end{Bmatrix} = \begin{bmatrix} A_{11} & A_{12} & A_{16} & B_{11} & B_{12} & B_{16} \\ A_{12} & A_{22} & A_{26} & B_{12} & B_{22} & B_{26} \\ A_{16} & A_{26} & A_{66} & B_{16} & B_{26} & B_{66} \\ B_{11} & B_{12} & B_{16} & D_{11} & D_{12} & D_{16} \\ B_{12} & B_{22} & B_{26} & D_{12} & D_{22} & D_{26} \\ B_{16} & B_{26} & B_{66} & D_{16} & D_{26} & D_{66} \end{bmatrix} \begin{Bmatrix} \epsilon_x^0 \\ \epsilon_y^0 \\ \epsilon_{xy}^0 \\ \kappa_x^0 \\ \kappa_y^0 \\ \kappa_{xy}^0 \end{Bmatrix} \tag{A.11}$$

The interlaminar shear components are given detached from the overall stiffness matrix:

$$\begin{Bmatrix} V_y \\ V_x \end{Bmatrix} = \begin{bmatrix} H_{44} & H_{45} \\ H_{45} & H_{55} \end{bmatrix} \begin{Bmatrix} \gamma_{yz} \\ \gamma_{xz} \end{Bmatrix} \tag{A.12}$$

Each ply in a laminate may be in a different state of stress. Equation A.11 represents the integrated stresses over all plies. The ABD matrix components are a function of the reduced stiffness matricies and z-values. Numerical Z-values are derived from ply thicknesses and scheduling [38].

$$\begin{aligned} A_{ij} &= \sum_{k=1}^{N} (\overline{Q}_{ij})_k (z_k - z_{k-1}) \qquad i,j = 1,2,6 \\ B_{ij} &= \frac{1}{2} \sum_{k=1}^{N} (\overline{Q}_{ij})_k (z_k^2 - z_{k-1}^2) \qquad i,j = 1,2,6 \\ D_{ij} &= \frac{1}{2} \sum_{k=1}^{N} (\overline{Q}_{ij})_k (z_k^3 - z_{k-1}^3) \qquad i,j = 1,2,6 \\ H_{ij} &= \frac{5}{4} \sum_{k=1}^{N} (\overline{Q}_{ij}^*)_k \left[t_k - \frac{4}{t^2} \left(t_k \overline{z}_k^2 + \frac{t_k^3}{12} \right) \right] \qquad i,j = 4,5 \end{aligned} \tag{A.13}$$

Minimal shear deformation occurs for such thin low ply count laminates studied here. However, the shear stiffness matrix is still important for sandwich plate structures with thick center cores. Finally, the equivalent moduli for used in the finite element analysis are given by:

$$E_x^b = \frac{12(D_{11}D_{22} - D12^2)}{t^3 D_{22}}$$

$$E_y^b = \frac{12(D_{11}D_{22} - D12^2)}{t^3 D_{11}}$$
$$G_{xy}^b = \frac{12D_{66}}{t^3}$$
$$\nu_{xy}^b = \frac{D_{12}}{D_{22}} \tag{A.14}$$

These properties are only accurate in predicting bending loads. Given this is the true actuation mode of the MFCs, the approach is applicable to predicting the response of MFCs in either unimorph or bimorph configurations.

A MATLAB file was created to automatically generate the final properties given above (see Appendix B).

Finally, Equation A.15 is used to relate the area density of a fabric to its thickness.

$$t_c = \frac{0.0339 \cdot w}{V_f \rho_f} \tag{A.15}$$

Where t_p is the ply thickness (mm), V_f is fiber volume fraction, w is fabric density (oz/yd^2), and ρ_f is fiber density (g/cm^3). The mix of units is due to how suppliers typically advertise fabric properties.

Appendix B

MATLAB Code for Determining Sensitivity of Laminate Mechanical Properties to Substrate Orientation

This MATLAB mfile will compute the equivalent stiffness properties of a laminate for various ply materials angles between 0 and 45° in bending only. These materials include E-Glass, S-Glass, and standard Carbon Fiber offerings from a typical supplier [23]. Note that E_x and E_y will be identical for the balanced laminates studied here, so they are plotting together.

```
% Calculates equivalent elastic moduli of a woven laminate for various
% ply angles and materials
% Equations from ISBN:1560327014, 1420054341
% Eric Gustafson 3-26-11

%Eglass(woven)
E1(1)=23.71e9;E2(1)=E1(1);G12(1)=3.10e9;
v12(1)=0.09;G13(1)=2.85e9;G23(1)=2.85e9;
%Sglass(woven)
E1(2)=27.29e9;E2(2)=E1(2);G12(2)=3.14e9;
v12(2)=0.08;G13(2)=2.91e9;G23(2)=2.91e9;
%CF(woven)
E1(3)=63.72e9;E2(3)=E1(3);G12(3)=3.31e9;
v12(3)=0.04;G13(3)=3.04e9;G23(3)=3.04e9;
```

```
15
16 th=0:45;
17
18 Ex=zeros(numel(th),3);
19 Ey=zeros(numel(th),3);
20 Gxy=zeros(numel(th),3);
21 vxy=zeros(numel(th),3);
22 Exb=zeros(numel(th),3);
23 Eyb=zeros(numel(th),3);
24 Gxyb=zeros(numel(th),3);
25 vxyb=zeros(numel(th),3);
26
27 for j=1:3
28
29     % Reduced compliance matrix
30     S1=[1/E1(j)          -v12(j)/E1(j)    0;...
31         -v12(j)/E1(j)    1/E2(j)          0;...
32         0                0                1/G12(j)];
33
34     % Interlaminar components
35     Q_star=[G23(j) 0;0 G13(j)];
36
37     for i=1:numel(th)
38
39         layers=th(i);
40         t=0.03733e-3;
41         n=numel(layers);
42
43         Qbarij=zeros(3,3,n);
44         Qbarij_star=zeros(2,2,n);
45         for k=1:n
46             theta=layers(k);
47
48             T1=[cosd(theta)^2 sind(theta)^2 2*sind(theta)*cosd(theta);...
49                 sind(theta)^2 cosd(theta)^2 -2*sind(theta)*cosd(theta);
50                 -sind(theta)*cosd(theta) sind(theta)*cosd(theta) cosd(theta
                       )^2-sind(theta)^2];
51             S=T1'*S1*T1;
52             Qbarij(:,:,k)=S^-1;
53
54             Qbarij_star(1,1,k)=Q_star(1,1)*cosd(theta)^2+Q_star(2,2)*sind(
```

```
                theta)^2;
55              Qbarij_star(2,2,k)=Q_star(1,1)*sind(theta)^2+Q_star(2,2)*cosd(
                    theta)^2;
56              Qbarij_star(1,2,k)=(Q_star(2,2)-Q_star(1,1))*sind(theta)*cosd(
                    theta);
57              Qbarij_star(2,1,k)=Qbarij_star(1,2,k);
58          end
59
60          % Find zkbar
61          zkbar=zeros(1,n);
62          zkbar(1)=t(1)/2;
63          for k=2:n
64              zkbar(k)=t(k)/2+sum(t(1:k-1));
65          end
66          zkbar=(zkbar-sum(t)/2);
67
68          % Compute ABDH matricies
69          A=zeros(3,3);
70          B=zeros(3,3);
71          D=zeros(3,3);
72          H=zeros(2,2);
73          for k=1:n
74              A=A+Qbarij(:,:,k)*t(k);
75              B=B+Qbarij(:,:,k)*t(k)*zkbar(k);
76              D=D+Qbarij(:,:,k)*(t(k)*zkbar(k)^2+1/12*t(k)^3);
77              H=H+Qbarij_star(:,:,k)*(t(k)-4/sum(t)^2*(t(k)*zkbar(k)^2+1/12*t
                    (k)^3));
78          end
79          H=H*5/4;
80
81          Ex(i,j)=(A(1,1)*A(2,2)-A(1,2)^2)/(sum(t)*A(2,2));
82          Ey(i,j)=(A(1,1)*A(2,2)-A(1,2)^2)/(sum(t)*A(1,1));
83          Gxy(i,j)=A(3,3)/sum(t);
84          vxy(i,j)=A(1,2)/A(2,2);
85
86          Exb(i,j)=12*(D(1,1)*D(2,2)-D(1,2)^2)/(sum(t)^3*D(2,2));
87          Eyb(i,j)=12*(D(1,1)*D(2,2)-D(1,2)^2)/(sum(t)^3*D(1,1));
88          Gxyb(i,j)=12*D(3,3)/sum(t)^3;
89          vxyb(i,j)=D(1,2)/D(2,2);
90
91      end
```

```
92
93  end
94
95  figure
96      h1=plot(th,Exb(:,1)/1e9,th,Exb(:,2)/1e9,th,Exb(:,3)/1e9);
97      %title('Variation of E_x^b & E_y^b with Ply Angle')
98      axis([0 45 0 70]),
99      xlabel('Ply Orientation Angle (deg.)'),ylabel('Stiffness (GPa)')
100     set(h1,'Linewidth',1.2)
101     legend('E-Glass','S-Glass','Std. Carbon Fiber')
102 % figure % Redundant
103 %     h2=plot(th,Eyb(:,1)/1e9,th,Eyb(:,2)/1e9,th,Eyb(:,3)/1e9);
104 %     title('Variation of E_y^b with Ply Angle')
105 %     xlabel('Ply Orientation Angle (deg.)'),ylabel('Stiffness (GPa)')
106 %     set(h2,'Linewidth',1.2)
107 %     legend('E-Glass','S-Glass','Std. Carbon Fiber')
108 figure
109     h3=plot(th,Gxyb(:,1)/1e9,th,Gxyb(:,2)/1e9,th,Gxyb(:,3)/1e9);
110     %title('Variation of G_x_y^b with Ply Angle')
111     xlabel('Ply Orientation Angle (deg.)'),ylabel('Stiffness (GPa)')
112     set(h3,'Linewidth',1.2)
113     legend('E-Glass','S-Glass','Std. Carbon Fiber')
114 figure
115     h4=plot(th,vxyb(:,1),th,vxyb(:,2),th,vxyb(:,3));
116     %title('Variation of \nu_x_y^b with Ply Angle')
117     xlabel('Ply Orientation Angle (deg.)')
118     set(h4,'Linewidth',1.2)
119     legend('E-Glass','S-Glass','Std. Carbon Fiber')
```

Appendix C

Composite Layup Process

Initial layup tests were completed to determine advantageous combinations of ply (laminate layers) orientations and thicknesses of the laminates. MFCs will eventually be bonded to similiar laminates. The primary focus is going to be fiberglass/ epoxy composites, and these tests include unidirectional and woven fiber architectures. A mold was machined in-house on a three axis mill using g-code generated from the GenMAV airfoil coordinates in the NX Manufacturing environment. A wax material (www.machinablewax.com) was chosen for ease of manufacture and layup extraction. Dry glass fabrics are hand cut, laid over the mold, wet out with epoxy, and then vacuum bagged. Curing of the composites occurs under 85°F and a vacuum of 25-30 inHg for the time period dictated by the hardener specifications. Each layup was completed with this 11 in (span) x 5 in (chord) mold.

Sixteen trial layups were completed. The table below shows the various combinations of plies and orientations.

Table C.1: Combinations of layers and ply orientations for each fabric weight.

Weight (oz/yd^2)	**Weave**	**Layers**	**Orientations (°)**
1.45	plain	1,2	0/90, ±45, 0/90/±45
3.16	plain	1,2	0/90, ±45, 0/90/±45
5.80	plain	1,2	0/90, ±45, 0/90/±45
4.20	uni	1,2	0,90,±45

For a thin airfoil such as the GenMAV, the coupon tests give a qualitative idea about what

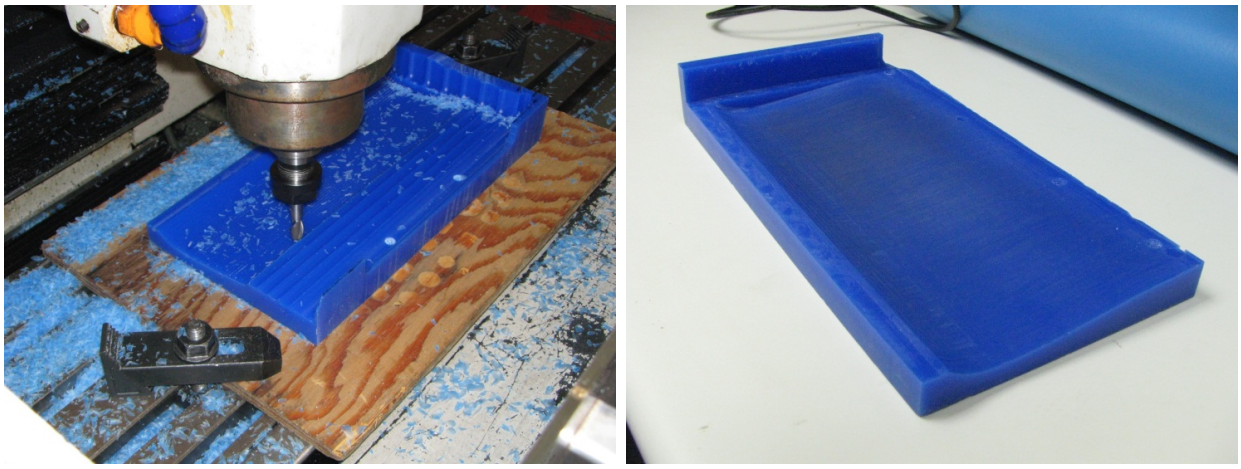

Figure C.1: Creating the mold for the GenMAV airfoil.

combinations are satisfactory for further study with finite element tools. This test has revealed that the range between 3.16 oz/yd^2 and 5.80 oz/yd^2 would include the acceptable lower bound. Any less and the material cannot hold the profile of the wing without deformation, even without the presence of external forces. Bonding MFCs to the top and bottom surfaces will increase the airfoil stiffness in the vicinity of the actuator(s), but portions exterior to this region still require sufficient stiffness to transmit lifting loads without excessive deflection. More detail is given in Chapter 3.

Elastic moduli can be sensitive to the fiber volume fraction of the composite (V_f). The V_f needed to be validated, since this type of manufacturing can typically create a V_f between 0% and 60% [38]. Using a set of digital calipers, the cured thickness of the glass epoxy layer of a GenMAV airfoil with the M8557-P1 actuator was measured as 6±0.5 mil. Rewriting Equation A.15:

$$V_f = \frac{0.0339w}{t_c\rho_f} = \frac{0.0399 * (1.45oz/yd^2 + 3.16oz/yd^2)}{0.1524mm * (2.6296g/cm^3)} = 0.39 \tag{C.1}$$

This indicates a V_f of 0.39±0.03. A V_f of 0.5 was used in estimating the orthotropic properties for deflection prediction; the actual value is thus within reason.

C.1 Notes on Composite Fabrics and Suppliers

Composite textile fabrics are available in a wide variety of weaves, weights, and materials. Analysis of composite properties was limited to plain weaves and relatively lightweight plies. Pre-impregnated ("prepreg") fabrics that ship to the consumer with embedded, uncured epoxy were not used due to fabrication constraints, but these offer better control over the fiber volume fraction. All products presented in this work came from one or more of the following distributors:

Table C.2: Suppliers of composite fabrics.

Distributor	**Website**	**Location**
ACP Composites	www.acp-composites.com	Livermore, CA, USA
Fibre Glast Development Corp.	www.fibreglast.com	Brookville, OH, USA
Aircraft Spruce	www.aircraftspruce.com	Corona, CA, USA

Appendix D

GenMAV Airfoil Coordinates

Table D.1: The nondimensional GenMAV airfoil coordinates.

x/c	**y/c**	**x/c**	**y/c**	**x/c**	**y/c**
0.0000	0.0011	0.3260	0.0600	0.6621	0.0256
0.0143	0.0126	0.3438	0.0587	0.6797	0.0235
0.0286	0.0224	0.3617	0.0573	0.6973	0.0214
0.0436	0.0312	0.3795	0.0559	0.7150	0.0193
0.0602	0.0393	0.3973	0.0544	0.7327	0.0173
0.0768	0.0459	0.4150	0.0529	0.7504	0.0154
0.0939	0.0513	0.4328	0.0512	0.7683	0.0136
0.1114	0.0557	0.4505	0.0496	0.7862	0.0119
0.1289	0.0590	0.4682	0.0479	0.8041	0.0103
0.1468	0.0614	0.4859	0.0461	0.8221	0.0088
0.1646	0.0631	0.5036	0.0442	0.8400	0.0075
0.1825	0.0641	0.5212	0.0423	0.8580	0.0064
0.2005	0.0647	0.5389	0.0404	0.8759	0.0053
0.2184	0.0647	0.5565	0.0384	0.8938	0.0044
0.2364	0.0645	0.5742	0.0363	0.9295	0.0029
0.2543	0.0639	0.5918	0.0342	0.9472	0.0022
0.2723	0.0632	0.6094	0.0321	0.9649	0.0015
0.2902	0.0623	0.6270	0.0299	0.9825	0.0007
0.3081	0.0612	0.6445	0.0278	1.0000	-0.0004

Appendix E

Additional Wind Tunnel Testing Details

E.1 Lift & Drag Coefficient Corrections

During wind tunnel testing, air flow around the airfoil models cannot perfectly represent freestream characteristics. Realistic limitations on test section size prevent wall boundaries from accuractely representing free air conditions. Barlow's [39] correction method comes from the method of images, where singularities are deliberately arranged to simulate real wall boundaries in a flow field. This is a lead-in to the panel method, which predicts 2D ideal flow fields around immersed geometries (same principle used by XFOIL). The coefficients presented in this work use corrections derived from those concepts.

$$C_l = K_{C_{lu}} C_{lu} \qquad C_d = K_{C_{du}} C_{du} \tag{E.1}$$

where $K_{C_{lu}}$ and $K_{C_{du}}$ are the correction factors relating corrected and uncorrected lift and drag coefficients, and "u" subscripts denote uncorrected values. Solid ε_{sb} and wake ε_{wb} blockage factors account for the change in freestream flow speeds due the presence of the physical model and its downstream wake, respectively.

$$K_{C_{lu}} = 1 - \sigma - 2\varepsilon_{sb} - 2\varepsilon_{wb}$$

$$K_{C_{lu}} = 0.960 - 0.357(C_{du}) \tag{E.2}$$

$$K_{C_{du}} = 1 - 3\varepsilon_{sb} - 2\varepsilon_{wb}$$

$$K_{C_{du}} = 0.979 - 0.357(C_{du}) \tag{E.3}$$

Compression of streamlines by the limited cross sectional test section area induces an increase in lift. This is corrected by an adjustment to the effective angle of attack:

$$\alpha = \alpha_u + \frac{57.3\sigma}{2\pi}\left(c_{lu} + 4c_{m_{\frac{1}{4}u}}\right)$$

$$\alpha = \alpha_u + 0.239(c_{lu}) \tag{E.4}$$

A reduction in effective airfoil span can arise from the boundary layer that generates along the floor and ceiling of the test section. Recently, Bilgen [6] determined the boundary layer displacement thickness at the airfoil quarter chord location as a function of static port pressure. This did not exceed the finite gap between the spanwise airfoil edges and test section surfaces, so its effect was assumed to be nominally zero.

E.2 Load Cell Calibrations

Two Transducer Techniques MLP-10 10 lb capacity load cells measure lift and drag forces. Each is connected to a Transducer Techniques TMO signal conditioner. Sensor signals are carried by shielded cabling to reduce interference noise. Individual load cell transfer functions are arrived from simple in-situ experiments. Precision weights were connected to the load cells via a high-gauge cable running through a low friction pulley. The C-arm attachment point lies at the center span-quarter chord location, by using of a metal "calibration" bar in place of the airfoil. The output trends demonstrate excellent linearity within the range of expected forces.

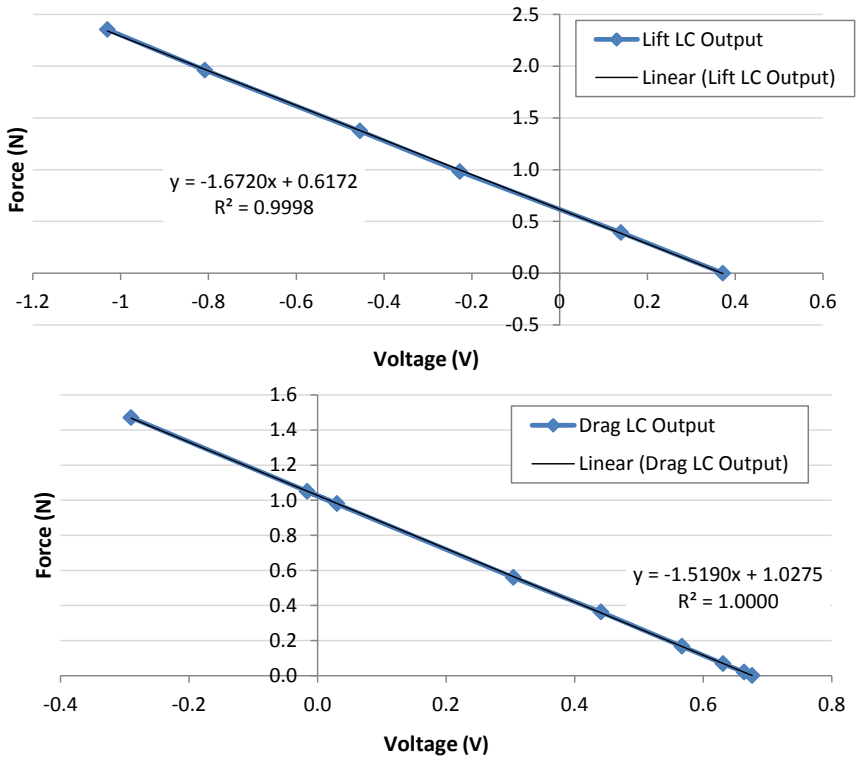

Figure E.1: Load cell output as a function of output voltage for lift (top) and drag (bottom).

E.3 Variation of WT Flow Speeds

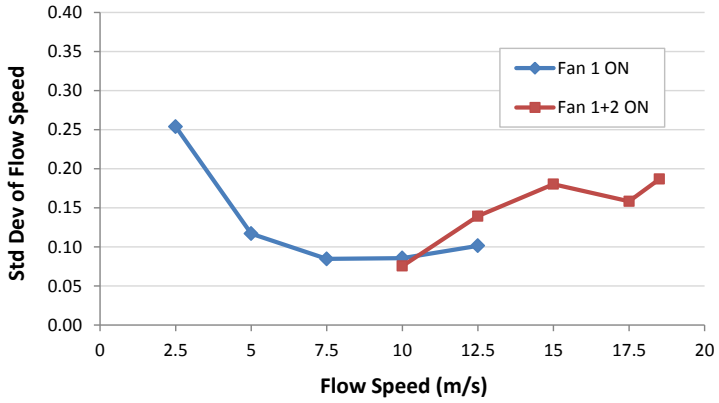

Figure E.2: Standard deviation of flow speed measurements as a function of flow speed.

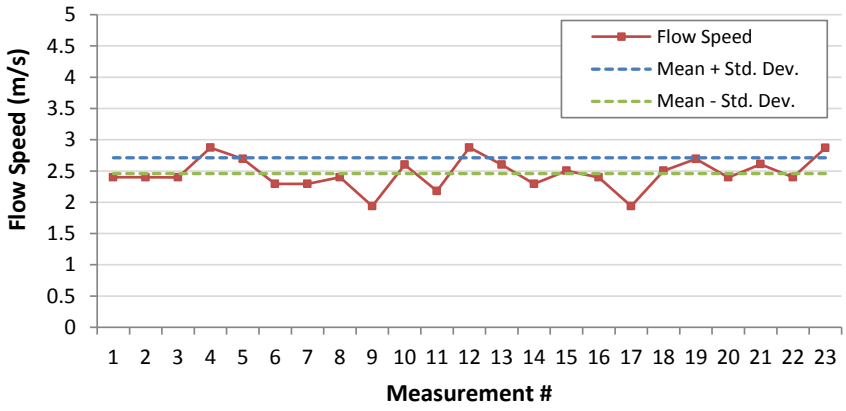

Figure E.3: Average wind tunnel speeds towards the lower limit of the flow speed range.

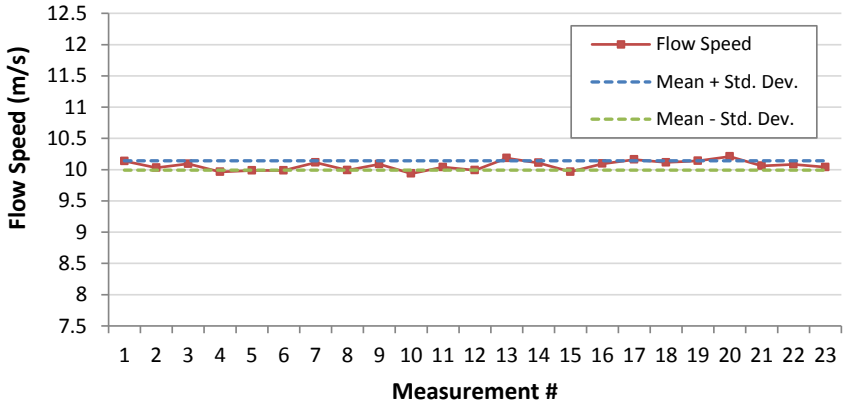

Figure E.4: Average wind tunnel speeds around the middle of the flow speed range.

E.4 LCO Amplitude and Frequency Plots

The plot on the following pages were generated in support of analysis on the limit cycle oscillations discussed in Chapter 7. Note that actuation indicies 0 to 24 represent an actuation sweep from $0\% \rightarrow -100\% \rightarrow +100\% \rightarrow -100\% \rightarrow 0\%$.

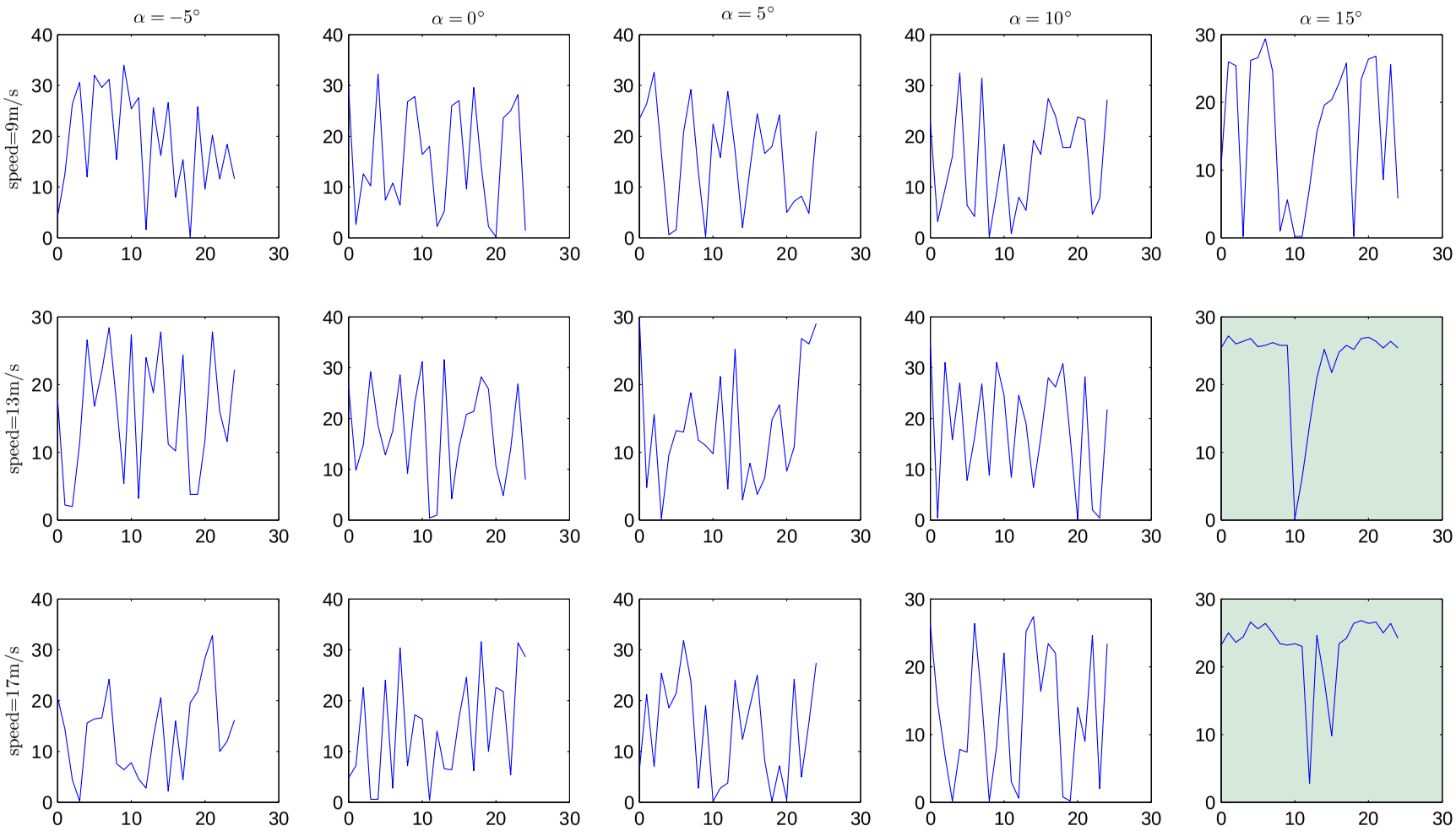

Note: For all plots, abscissa is frequency (hz), and ordinate is actuation index number.

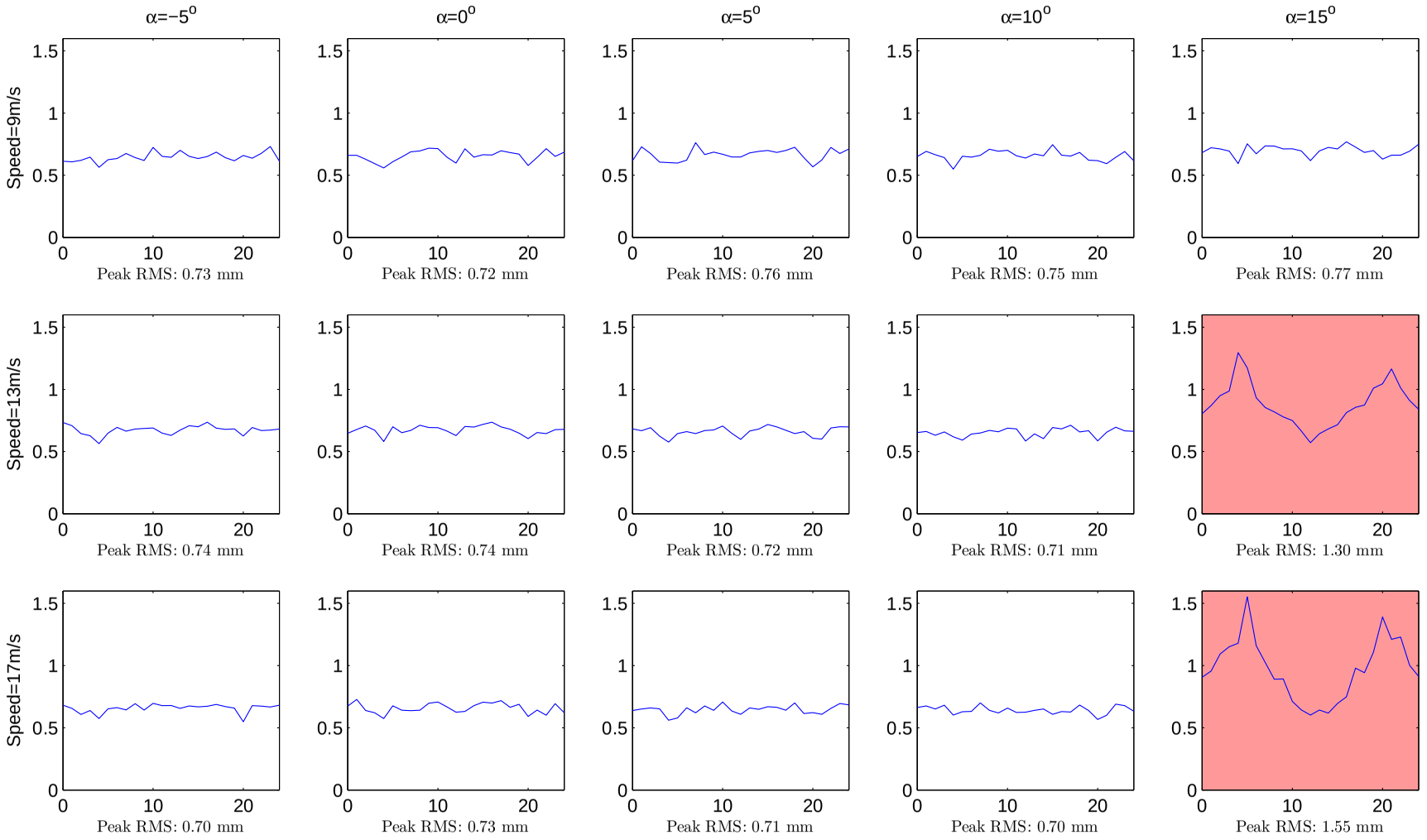

Note: For all plots, abscissa is displacement RMS (mm), and ordinate is actuation index number.

E.5 Laser Displacement Plots

The output from the laser displacement sensor mounted on the wind tunnel test section wall is plotted in Figure E.5. The laser is nominally aimed at the trailing edge of the airfoil during all tests. These values are inherently inaccurate, due to the fixed mounting of the sensor and movement of the airfoil. Consider the scenario that occurs for one particular actuation input level. The laser may measure deflection at a different chordwise station along the airfoil for a different attack angles.

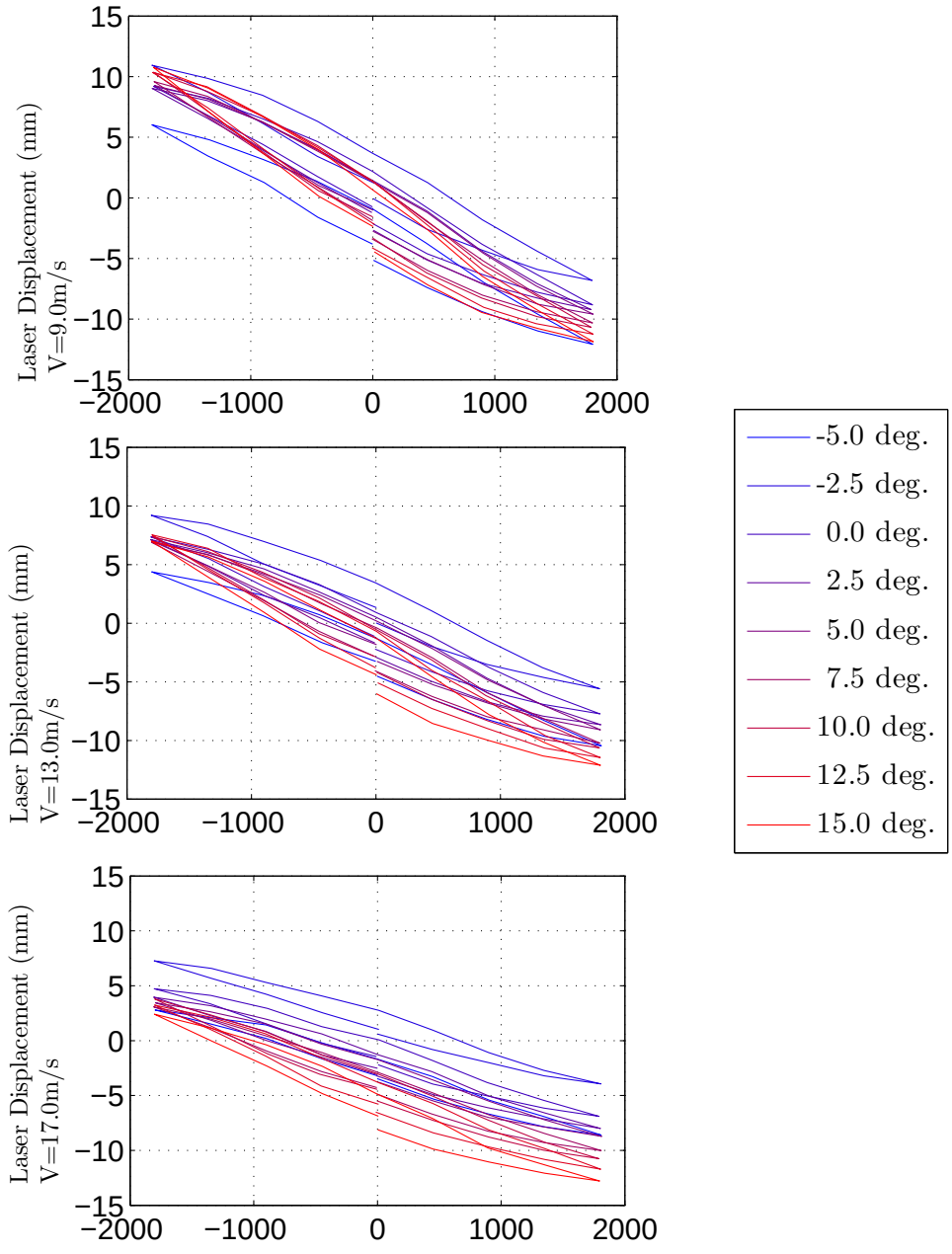

Figure E.5: Static displacements versus input voltage for flow speeds $U = 9, 13, 17m/s$.

Appendix F

Additional Lightweight Circuit Details

Two T-2505 and one T-1505 AM Power Systems DC-DC converters provide the voltage amplification for the MFC actuators. The total bleed resistance is divided amongst multiple medium power (1W) resistors, to prevent over-volting. Three out of the four op amp (Digikey part OPA4743UA/2K5) channels are connected to a general purpose NPN power transistor (Digikey part 497-2462-1) to uncouple current draw from the signal source. The high voltage diodes were samples from HVCA (part SP5L).

CAM files are generated and sent to Advanced Circuits, Aurora, CO, which handles printed circuit board manufacture. The two layer board is then populated in-house almost exclusively with SMDs using a Hakko hot air rework station.

After the PCB was populated, a few issues such as an insufficient solder pad size became apparent. These were resolved after a few light modifications. Since flight weight is a concern, the weight of the PCB was examined. The total weight was mostly represented by the three converters (4.5 g each), and the PCB (19 g), for a total of 32.5 g. A 9 V battery weighs about 47 g by comparison. A more complete breakdown of typical components used with a 2 lb MAV are compared in Chapter 4.

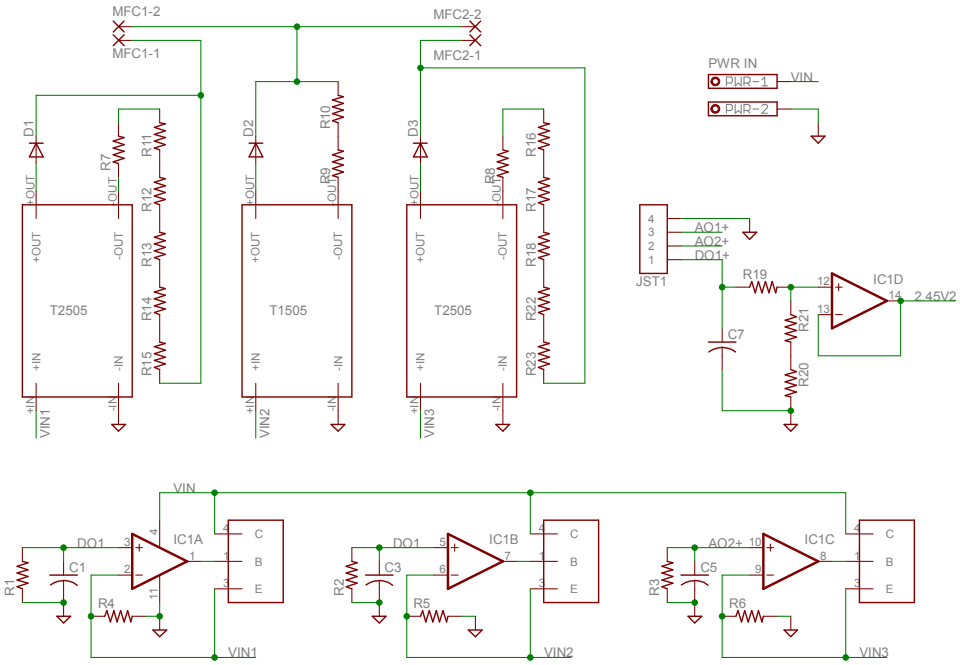

Figure F.1: Electrical schematic of the lightweight MFC driver PCB.

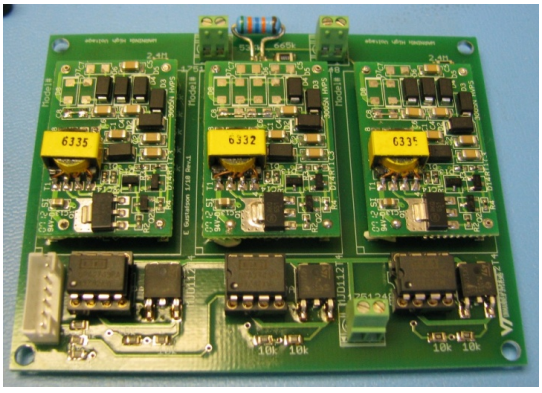

Figure F.2: Final populated revision 1 of the lightweight circuit prototype.